Title
MICRDSTRUCTURE AND MAGNETIC PROPERTIES OF MnZn-FERRITE

Author
Lin, I-N.

Publication Date
1982-12-01

Lawrence Berkeley Laboratory
UNIVERSITY OF CALIFORNIA

Materials & Molecular Research Division

MICROSTRUCTURE AND MAGNETIC PROPERTIES OF MnZn-FERRITE

I-Nan Lin
(Ph.D. Thesis)

December 1982

Prepared for the U.S. Department of Energy under Contract DE-AC03-76SF00098

DISCLAIMER

LBL-15434

MICROSTRUCTURE AND MAGNETIC PROPERTIES ON MnZn-FERRITE

By

I-Nan Lin
(Ph.D. Thesis)

Lawrence Berkeley Laboratory
University of California
Berkeley, California 94720

December 1982

This work was supported by the Director, Office of Energy Research, Office of Basic Energy Sciences, Division of Materials Science of the U.S. Department of Energy under Contract Number DE-AC03-76SF00098 and by the Institute of Nuclear Energy Research (R.O.C.).

MICROSTRUCTURE AND MAGNETIC PROPERTIES OF MnZn-FERRITE

I-Nan Lin

Ph.D. Materials Science and Mineral Engineering

Sponsors: U. S. Department of Energy
R.O.C. Institute of Nuclear Energy Research

Gareth Thomas
Chairman of Committee

ABSTRACT

Grain boundaries in MnZn-ferrites have been characterized and their effects on the magnetic and electrical properties have been investigated. In addition, controlled atmosphere annealing has been performed on high permeability ferrite to improve the electrical resistivity of the bulk materials.

The addition of a small amount of CaO into MnZn-ferrite materials is observed to lead to the formation of secondary phases along the grain boundaries. These grain boundary phases which consist of a thin layer of CaO/MnZn-ferrite intermediate compound, exist as liquid phases at sintering temperature and as amorphous phases when cooled to room temperature.

Partial dissolution of Ca ions into the matrix results in a higher magnetic anisotropy energy in the regions near grain boundaries and the amorphous grain boundary phases act as non-magnetic barriers; both of them retard magnetic domain wall motion. The grain boundary phases, on the other hand, also act as insulating layers for electrical conduction. The space charge polarization of the materials, however, renders the blocking effect totally invalid in the high

frequency regime. It is concluded from these observations that the Ca addition in these materials does not produce beneficial effects on the electrical properties but only leads to a detrimental influence on the magnetic properties.

Other microstructural features such as secondary phases and stacking faults will also affect, besides grain boundaries, the domain wall dynamics. They not only retard the domain wall motion but can also act as nucleation sites for domains of reverse magnetization.

The controlled atmosphere annealing improves drastically the apparent resistivity of the sintered MnZn-ferrites through the reduction of ferrous ions content. The magnetic permeability is, unfortunately, degraded as a result of annealing. This is ascribed to the inhomogeneity of the oxidation in the polycrystalline specimens. Therefore, a stringent control of the oxygen partial pressure at an earlier stage of processing rather than post fabrication annealing is called for, in order to raise the intrinsic electrical resistivity of the bulk materials by reducing ferrous ion concentration but not to affect the magnetic permeability detrimentally.

Table of Contents

ABSTRACT

Grain boundaries in MnZn-ferrites have been characterized and their effects on the magnetic and electrical properties have been investigated. In addition, controlled atmosphere annealing has been performed on high permeability ferrite to improve the electrical resistivity of the bulk materials.

The addition of a small amount of CaO into MnZn-ferrite materials is observed to lead to the formation of secondary phases along the grain boundaries. These grain boundary phases which consist of a thin layer of CaO/MnZn-ferrite intermediate compound, exist as liquid phases at sintering temperature and as amorphous phases when cooled to room temperature.

Partial dissolution of Ca ions into the matrix results in a higher magnetic anisotropy energy in the regions near grain boundaries and the amorphous grain boundary phases act as non-magnetic barriers; both of them retard magnetic domain wall motion. The grain boundary phases, on the other hand, also act as insulating layers for electrical conduction. The space charge polarization of the materials, however, renders the blocking effect totally invalid in the high frequency regime. It is concluded from these observations that the Ca addition in these materials does not produce beneficial effects on the electrical properties but only leads to a detrimental influence on the magnetic properties.

Other microstructural features such as secondary phases and stacking faults will also affect, besides grain boundaries, the domain wall dynamics. They not only retard the domain wall motion but can also act as nucleation sites for domains of reverse magnetization.

The controlled atmosphere annealing improves drastically the apparent resistivity of the sintered MnZn-ferrites through the reduction of ferrous ion content. The magnetic permeability is, unfortunately, degraded as a result of

annealing. This is ascribed to the inhomogeneity of the oxidation in the polycrystalline specimens. Therefore, a stringent control of the oxygen partial pressure at an earlier stage of processing rather than post fabrication annealing is called for, in order to raise the intrinsic electrical resistivity of the bulk materials by reducing ferrous ion concentration but not to affect the magnetic permeability detrimentally.

INTRODUCTION

MnZn-ferrites are mainly used in telecommunication and entertainment electronics[1-10]. Their technical importance stems from high initial permeability and low magnetic and electrical losses; linear temperature dependence and stable time dependence of these properties have also been recognized recently as important factors.

In addition to being composition dependent, MnZn-ferrites are extremely microstructure dependent and hence processing sensitive. In the past, all efforts to improve the magnetic properties have emphasized the control of composition, impurities (additives), grain size and porosity. While large improvements in magnetic properties have been achieved by adjusting chemical compositions and optimizing the processing parameters[11-38], little progress has been made toward understanding the influence of the grain boundaries until recently[18,39-47].

In general, the presence of secondary phases at grain boundaries in polycrystalline ceramics has great influence on their mechanical and electronic properties[48-50]. In the case of high temperature structural ceramics, such as Si_3N_4, the amorphous boundary phase is responsible for low temperature creep[51]. In the case of electronic materials, such as PZT, ZnO varistors and soft ferrites, the presence of a thin grain boundary layer drastically affects the electrical and magnetic properties[18,39-47]. The formation of a second phase at grain boundaries in ceramic materials is very common, and a complete characterization of these second phases can be done only by modern techniques, such as transmission electron microscopy (TEM), analytical electron microscopy (AEM) and auger electron spectroscopy (AES).

In MnZn-ferrite, CaO has been added to increase the resistivity of the material through the formation of an insulating layer along grain boundaries[43,44]. The exact nature of these grain boundary phases and the influences of these phases on magnetic behavior have, however, not been thoroughly investigated. In this study, the physical and chemical characteristics of the grain boundary phases in commercial MnZn-ferrites are examined using the above-mentioned techniques. For the purpose of exploring the role of grain boundary phases in determining the magnetic and electrical properties, Lorentz microscopy in TEM was used to study the interaction of magnetic domain walls with grain boundaries and the complex-impedance technique was used to examine the electrical behavior of grain boundaries.

Finally, controlled atmosphere annealing was performed on low resistivity ferrite in order to increase the intrinsic electrical resistivity of the bulk materials without degrading the magnetic properties, since the formation of an insulating layer by CaO addition is known to be detrimental to magnetic properties[18].

II. GRAIN BOUNDARY PHASES

II.A. Ca-Segregation at Grain Boundaries

II.A.1. Introduction

MnZn-ferrite is a soft ferrite with high initial permeability (μ_i). A small amount of CaO is added in commercial $(Mn,Zn)Fe_2O_4$ to increase the electrical resistivity through the formation of an insulating layer along the grain boundaries[43,44]. There are two different views on the formation of this high resistivity layer: (i) an insulating amorphous phase containing CaO forms at the sintering temperature[43] and (ii) a high resistivity layer forms during cooling of the sample from high temperature, during which grain boundary oxidation occurs as a result of Ca segregation[39,45]. A recent study on CaO doped MnZn-ferrite has given support to the first model of formation of an amorphous phase: the existence of an amorphous intergranular phase has been observed[18]. The equilibrium phase diagram of the Calcium-Magnetite system shows the existence of an intermediate phase with the composition $CaO.Fe_2O_3$ and a eutectic temperature at about 1220°C[52,53].

In this investigation, the existence of an intermediate phase between CaO and MnZn-ferrite is investigated and the mechanism of formation of the CaO rich grain boundary layer is explored. In-situ heating in a scanning electron microscope (SEM) and a high voltage transmission electron microscope (HVEM) is used to examine the formation of the liquid phase at high temperature. Auger electron spectroscopy (AES) of fractures surfaces is used to determine the chemical composition of the intergranular phase.

II.A.2. Experimental

Sintered MnZn-ferrite samples with a nominal composition of

$MnO:ZnO:Fe_2O_3$ = 26.9:19.8:53.3 (mole%) and with major impurity of CaO (2543ppm) were used for studying the CaO/MnZn-ferrite reaction and the grain boundary characteristics. A 1mm x 4mm x 4mm slice of the sintered specimen was coated with 99.99% pure CaO powder in a platinum crucible and was heated in the hot stage of a JSM-U3 scanning electron microscope (SEM) in high vacuum to a temperature of 1320°C. The room temperature microstructure of the reacted surface was examined and the chemical composition was determined using an AMR-1000 SEM with a KEVEX x-ray analyzer.

The grain boundary composition was determined by Auger electron spectroscopy[46,54-63] (AES). A slice of the specimen was fractured in situ in a Physical Electronics-590 Scanning Auger Electron Microscope. The chemical composition of the fractured surface was determined from the Auger electron spectra. The Ca distribution of the fractured surface was examined by mapping the Ca Auger electron signal, and the corresponding fractured microstructure was imaged with the secondary electron signal. To study the behavior of Ca diffusion at high temperature, a specimen was fractured at 1300°C, after it was kept at 1300°C for 0.5 hours (in 2400ppm PO_2), and then quenched to room temperature. The Ca distribution and the corresponding fractured microstructure of this specimen were also examined by AES. The behavior of the grain boundary phase at sintering temperature was studied by in-situ heating in a high voltage electron microscope (HVEM). A 2.3mm electron transparent thin foil was prepared from the bulk material by the ion milling technique and was heated in the hot stage of the Osaka University 2MeV HVEM to a temperature of 1400°C. Similar foils were used to examine the characteristics of the grain boundary phase using a Siemens 102 high resolution TEM[63-67].

II.A.3. Results and Discussion

(a) Reaction of CaO and MnZn-ferrite. A SEM hot stage experiment was done on a MnZn-ferrite specimen coated with CaO powder. At the start of the experiment, two different areas were observed. Region A showed an exposed MnZn-ferrite surface with small islands of CaO. In region B no substrate could be seen due to the thickness of the continuous CaO layer.

Reactions between the CaO powder and the ferrite matrix occurred only above 1250°C. A liquid phase was first seen at about 1320°C. It wetted the ferrite substrate and, as shown in Fig. II.1a, coexisted with solid phases in the same region. When the sample was cooled slightly from 1320°C, a secondary phase nucleated (Fig. II.1b), which could be remelted by heating with condensed electron beams (Fig. II.1c). When the sample was further cooled to room temperature, a two phase microstructure, characteristic of the solidification of a eutectic liquid was obtained as shown in Fig. II.2. The chemical composition of the two phases, as analyzed using x-ray microprobe, is listed in Table I. In the region A (Fig. 2.a), the matrix contained a negligible amount of Ca and the elongated precipitates are rich in Ca. On the other hand, in the region B (Fig. II.2b), the reverse was the case, namely, the matrix was rich in Ca and the round precipitates contained a much smaller amount of Ca.

Owing to the short time at high temperature and the fast quenching rate, the phases observed are not necessarily the equilibrium ones. The results of this experiment, however, indicate definitely the presence of a liquid phase and an intermediate phase in the CaO-(Mn,Zn)Fe_2O_4 system.

No intermediate phases have been reported in commercial MnZn-ferrite where CaO concentrations are of the order of 3000ppm. Further work must be done to determine whether these phases and liquid phases are present in

commercial material. For this purpose, two experiments were performed: (i) grain boundary composition determination by Auger electron spectroscopy and (ii) in-situ heating of a thin foil in a high voltage electron microscope (HVEM).

(b) Composition and nature of grain boundary phases. The AES spectra from a room temperature in-situ fractured specimen of commercial MnZn ferrite are shown in Fig. II.3. The corresponding regions from which the spectra were taken are indicated in the accompanying fracture micrograph which was obtained from the secondary electron signal of the same specimen. The Ca signal was observed only when the electron probe, 500Å in diameter, was placed at an intergranular fracture surface (region B). No Ca peak was observed when the electron probe was placed at a transgranular fracture surface (region A). This Ca signal completely disappeared after the fractured surface was in-situ sputtered by Argon ions for only six minutes. Since the escape depth of the Auger electrons is less than 20Å and the sputtering rate is about 10Å/min.[54-60], the thickness of the Ca containing phase is estimated to be about 60Å. These observations indicate that a Ca-containing phase forms only in a very thin layer along grain boundaries.

Besides the Ca signal indicated in Fig. II.3b, the spectrum from the intergranular fracture surface also shows Fe and Mn signals. This indicates that the grain boundary phase does not contain CaO alone as proposed by other authors[39,43-45]. Although the chemical composition is very difficult to determine quantitatively, it can be concluded that the grain boundary phase is an intermediate compound of CaO and MnZn ferrite. This is in agreement with the results of the SEM hot stage experiment discussed earlier. The high resolution dark field micrograph[67] in Fig. II.4 shows that this grain boundary phase exists as a 50Å thick amorphous layer. The existence of a grain boundary phase

in an amorphous state has been shown in other systems. It occurs due to the difficulties of crystallization of thin liquid layers of liquid trapped between grains[68,69].

To establish if Ca segregates at the grain boundary region during cooling from the sintering temperature, an experiment was performed in which specimens were fractured at high temperatures or at room temperature and subsequently studied by AES. In both cases, Ca distribution is similar, viz. Ca exists only at the intergranular fracture surfaces and no Ca is detected at transgranular fracture surfaces. In other words, Ca stays at the grain boundaries, as is shown in the Ca map and the fracture micrograph of a fractured specimen in Fig. II.5.

If Ca dissolves into the matrix at high temperature and resegregates upon cooling, it should be distributed uniformly over the fracture surface of a specimen which was fractured at 1300°C and then cooled. On the other hand, if the amorphous phase only melts at high temperatures, but stays at the grain boundaries, the Ca distribution will be the same no matter whether it is fractured at high temperature or at room temperature. From the above argument and the experimental data, it is concluded that Ca stays at the grain boundary at the sintering temperature.

(c) Behavior of grain boundary phases at high temperature. In the hot stage experiments in the 2MeV electron microscope, for temperatures below 1300°C, there is no noticeable reaction--neither sublimation of the bulk material nor migration of the grain boundaries is observed. However, when the temperature reaches 1300°C, the sublimation of the material at the thin edge of the specimen is observed. The sublimation continues at higher temperatures. Besides the acceleration of the sublimation rate, the following three observa-

tions are made when the specimen is heated from 1300°C to 1400°C. (i) The image of the grain boundary changes from a sharp line (or fringes) to a diffuse line when the temperature reaches 1400°C (Fig. II.6). The existence of a disordered phase at the grain boundary at 1400°C is inferred from this observation. (ii) The positions of the three grain junctions are shifted due to grain boundary migration. The migration is more prominent in the junctions in which the angle between the grain boundaries originally deviated considerably from 120° (e.g. junctions a, b and c in Fig. II.6b). (iii) The sublimation of the material at three grain junctions begins when the specimen temperature reaches 1400°C, and the sublimation continues at that temperature (junction d in Fig. II.6). The sublimation also occurs at the grain boundaries. In view of the above observations, it is suspected that the grain boundary region first melts and then evaporates.

The tendency of the grain boundaries to make equal angles with each other implies that the grain boundary surface energy is isotropic at high temperature. This idea also supports the existence of either a non-crystalline phase or a liquid phase at the grain boundaries, as the solid-liquid interfacial energy is known to be less anisotropic than the solid-solid interfacial energy[70]. In summary, both the sublimation at grain boundaries and the grain boundary migration can be correlated to the existence of a non-crystalline phase at grain boundaries at high temperature, which is implied from the diffuse image of the grain boundaries and is in agreement with the liquid phase observed in the SEM hot stage experiment.

In thinning the specimen for use in the HVEM, some small holes inside grains were observed. One such hole is shown in Fig. II.6. As the temperature increased, the size of the hole increased, apparently due to sublimation of the

thin area around the hole. When the specimen was held at 1400°C, no further changes were observed. Furthermore, most of the grain boundary migration occurred when the temperature was rising. The shape and size of the grains hardly changed while the specimen was held at 1400°C. These observations suggest that a rapid rise in the temperature aids in mass transport, which accounts for the formation of the internal pores in type B material (Fig. II.7). This material was processed by a rapid rise of the sintering temperature. The grain boundary mobility was enhanced during the temperature rising period such that the grain boundaries were detached from the pores and abnormal grain growth occurred[71-74]. The pores were thus trapped inside the grains.

II.A.4. Conclusion

The formation of a Ca-rich liquid phase at 1250°C ~ 1320°C in the CaO-(Mn,Z n)Fe_2O_4 system is confirmed from in-situ SEM observations. In the case of commercial MnZn-ferrite containing small quantities of CaO, the existence of a liquid phase at the grain boundaries at high temperature is confirmed from in-situ HVEM observations. The AES chemical analysis of fractured surfaces of MnZn-ferrite show that Ca is present only in the grain boundary regions, as a thin layer of CaO/MnZn-ferrite intermediate compound in an amorphous form. The Ca must be present in the liquid phase at the sintering temperature and does not dissolve and resegregate during the heating cycle.

II.B. The Effect of the Grain Boundary Phase on Magnetic and Electrical Properties

II.B.1. Introduction

The presence of a thin grain boundary layer will significantly affect the electrical and magnetic properties of electronic ceramic materials, such as PZT, ZnO varistors and soft ferrites[50]. An addition of a small amount of Ca in MnZn-ferrite increases the electrical resistivity, as well as the coercivity of the material, but lowers the initial permeability[18]. All these effects can be ascribed to the segregation of Ca at grain boundaries. The physical and chemical nature of the grain boundary phase resulting from the addition of Ca can be characterized by modern analysis techniques such as TEM, SEM and AES and have already been described in detail. However, a complete understanding of the mechanisms by which this phase affects the magnetic and electrical properties of $(Mn,Zn)Fe_2O_4$ has not been achieved.

In the present investigation, Lorentz microscopy in TEM[75-80] and convergent beam electron diffraction[81-85] (CBED) were used to examine the interaction of magnetic domain wall motion with the grain boundary phase. The complex impedance technique was used to separate the electrical behavior of the grain boundary phase from that of the bulk material. Mechanisms of interaction are proposed to explain the effect of the grain boundary phase on the magnetic and electrical properties of MnZn-ferrite.

II.B.2 Experimental

Two typical commercial MnZn-ferrite samples were used to study the effect of the grain boundary phase on magnetic and electrical properties; the low loss material (type A) contained a CaO additive for reducing the magnetic loss, whereas the high permeability material (type B) contained no additives

aside from inherent impurities. The microstructures of the two types of specimens were examined by SEM, after sectioning, polishing and etching in a 25%HF and 75% HCl solution.

The magnetic and electrical properties were calculated from the measured impedance of the specimens. The details of the apparatus and data analyzing procedures for these measurements are described in Appendix A. Briefly, a toroidal geometry was used for magnetic measurement; toroids of 4.76mm (3/16") I.D., 9.52mm(3/8") O.D., and 1.5mm thick were cut with an ultrasonic cutter from bulk material and wound with copper coils. The initial permeability (μ') and magnetic loss (μ'') of the specimens (toroids) were calculated from the self-inductance of the coils, which, in turn, were derived from their measured impedance. A rectangular geometry was used for electrical measurements; rectangular bars of dimensions 2.67mm x 5.5mm x 10.53mm were cut with a diamond saw from bulk material. The apparent resistivity (ρ_p) and dielectric constant (ε_p) of the specimens (rectangular bars) were derived directly from their impedance. The impedance of the coils wound on the toroidal specimens and that of the rectangular bars were measured by an HP gain-phase meter.

To study the effect of grain boundary phases on magnetic properties, the interaction of the magnetic domain walls with the Ca-segregated grain boundaries was examined by Lorentz microscopy in a Philips EM301 electron microscope. The theory of Lorentz microscopy can be found[75-80] elsewhere and the principle of operation will be described in detail in the next chapter (Ch. 3). Only the result of the observations on domain wall/Ca-segregated grain boundary interaction and its significance will be discussed in this section. The localized strain in the regions near the grain boundaries caused by the CaO-

addition was examined by convergent beam electron diffraction (CBED)[81-85] using a Philips EM400 electron microscope.

To study the effect of grain boundary phases on electrical properties, the characteristic parameters of the materials, namely bulk resistance, grain boundary resistance and grain boundary capacitance, were derived from the measured impedances of the materials, using the complex impedance technique. The measured resistance (Rx) of the specimen is plotted against the reactance (Xx) over a wide range of frequencies. The characteristic parameters are obtained from the interceptions of the complex impedance dispersion by extrapolating the plot towards very low or very high frequencies. The details of the complex impedance technique and the modelling of the materials are described in Appendix A. Again, only the results of analysis on the materials will be discussed in this section.

II.B.3 Results

(a) Magnetic and electrical properties of the two typical materials. The initial permeability (μ'), magnetic loss (μ'') and loss tangent (tan) of the two typical materials, plotted against operating frequencies, are shown in Fig. II.8. The initial permeability (μ') remains at a constant level up to a certain frequency regime and then drops off quickly (Fig. II.8a) due to magnetic resonance[7,8,86]. This is also indicated by the rapid increase in the magnetic loss (μ'') at the corresponding frequency (solid lines in Fig. II 8b). The loss observed at the low frequency regime (dashed lines in Fig. II 8b) arises from the electrical conducting loss due to the residual resistance of the copper coils and has nothing to do with the magnetic losses.

The initial permeability (μ') of type B material is higher than that of type A material for the low frequency regime but drops off much more quickly at high frequencies (Fig. II 8a). The loss tangent ($\tan\delta$) which describes the ratio of the dissipated energy to the stored energy, is also much higher than for type A material in the high frequency regime (Fig. II 8c). The onset of magnetic resonance, or the frequency of maximum magnetic loss, indicated by arrows in Fig. II 8b, is lower in the case of the higher permeability material (type B material in this case). This is generally true and can be explained in terms of the resonance of rotation magnetization under action of the anisotropic field[87].

The apparent resistivity (ρ_p) of the two materials, plotted against the operating frequencies (Fig. II 9a), behaves in a similar manner to that of the initial permeability (μ'), i.e. it remains at the same level for a certain range of operating frequencies and drops off in the high frequency regime. The type A material shows much higher apparent resistivity (ρ_p) than the type B material. This is ascribed to the formation of the insulating layer along grain boundaries as a result of CaO addition to this material[43]. The effect of the CaO addition on increasing the electrical resistivity in the type A material is, however, not as significant in the high frequency regime. This implies that the space charge polarization becomes more important in this regime; the high resistance provided by the grain boundary layers will be short circuited at extremely high operating frequencies. This will be discussed in detail in Section 3c.

(b) Effect of the grain boundary phase on magnetic properties. The initial permeability (μ') of a magnetic material is believed to arise from the reversible displacement of magnetic domain walls within the material[5-9]. Microstructural defects, such as grain boundaries in the polycrystalline materials, interact with domain wall motion and are expected to play a

significant role in determining the magnetic behavior of the materials. Among many types of defects in the materials, grain boundary segregation causes the most substantial interaction with the domain wall and the most detrimental effect on the magnetic properties.

The interaction of grain boundary segregation with domain walls in the Ca-containing material (Type A) was examined by Lorentz microscopy in TEM and is shown in Fig. II 10. In this figure, the domain configurations are shown in sequence of increasing applied magnetic field. For each applied field a pair of Lorentz images (underfocused and overfocused) is shown. In the accompanying schematic drawings, the magnetic domain walls are shown as solid/dashed lines and grain boundaries, as dotted lines. As the magnetic field increased, the domains B and C grew, while the domain A, which was partly bounded by grain boundaries, did not change at all. In other words, the domain wall was not able to move toward the grain boundary under a moderate applied magnetic field. Only after the magnetic field was raised appreciably did the domain A change its magnetization vector causing the domain wall to abruptly jump to the grain boundary. This domain wall was still not able to move across the grain boundary even when the magnetic field was further increased.

While the Ca-segregated grain boundaries stopped domain wall motion before domains reached the grain boundaries, it has been observed that the domain wall can move toward the clean grain boundaries and microcracks continuously (cf. Ch. 3). The region near segregated grain boundaries is, therefore, suspected of being locally strained. This was found to be true[18] and was confirmed by convergent beam electron diffraction (CBED). In this technique the paths of electrons converge on the specimen[81-85], in contrast to conventional electron diffraction where the paths of the electrons are paral-

lel[78-80]. The CBED pattern consists of discs, each of which corresponds to a Bragg spot in conventional diffraction. The sharp lines in the central disc, termed HOLZ lines for higher order Laue zones, and the intensity distribution in the surrounding discs are sensitive to crystal structure and lattice parameter changes.

The CBED patterns of $(Mn,Zn)Fe_2O_4$, which is a spinel structure, for an [001] zone axis orientation, are shown in Fig. II.11. When the 2000Å diameter electron probe is placed in the interior of the grain, both the HOLZ lines and intensity distribution show 4mm symmetry. This is expected for the Fd3m symmetry of the spinel structure. However, when the probe is placed in the region near a grain boundary the CBED pattern no longer exhibits such a high degree of symmetry. The HOLZ lines indicate a symmetry of 2mm while the intensity distribution indicates only mirror plane symmetry. The lowering of the structure symmetry in the region near the grain boundary thus confirms the presence of strain which is ascribed to the dissolution of a small number of Ca ions, which are much larger than the other cations, into the matrix.

(c) Effect of the grain boundary phase on electrical properties. The conducting mechanism in spinel ferrite is attributed to the hopping of electrons between ferrous (Fe^{2+}) and ferric (Fe^{3+}) ions. The abundance of Fe^{2+} and Fe^{3+} ions in $(Mn,Zn)Fe_2O_4$ results in an unusually high intrinsic conductivity as compared with many ceramics[88,89]. However, the insulating layers along grain boundaries, due to CaO addition, block the transport of electrons between grains such that the apparent resistivity of the material is increased.

Owing to the tremendous difference in the electrical conductivity between the bulk material and the grain boundary phase, motion of electrons occurs readily through grains but is interrupted when it reaches the interfaces.

The grain boundaries behave as a high dielectric constant material and large polarization occurs as a result of the build-up of charges. Electrically, the actual system can be represented by the equivalent series circuit illustrated in Fig. II.12. The bulk grains and grain boundaries are represented by lumped circuits consisting of parallel resistance-capacitance combinations.

In low operating frequencies the high grain boundary resistance significantly contributes to the overall resistance of the specimen. Thus the material containing CaO additives exhibits high apparent electrical resistivity in this regime. However, when the operating frequency increases, the polarization occurring at grain boundaries will lower the effective impedance of the grain boundary and may short circuit the grain boundary resistance in the extremely high frequency regime. The insulating effect of this grain boundary phase is thus totally overcome and the apparent resistance of the specimens appears to be the same as that of bulk materials (Fig. II 9a).

The separation of the electrical behavior of the grain boundary phase from that of the bulk in polycrystalline materials can be achieved by using the complex impedance technique (cf. Appendix A). As shown in Fig. II. 9b, the resistance (R) of the specimens is plotted against reactance (X), over a wide range of frequencies, for both types of material. The interception at the high frequency end (L.H.S.) represents the bulk resistance and that at the low frequency end (R.H.S.) represents the sum of bulk and grain boundary resistances. The characteristic parameters for the two typical materials obtained by using this analysis technique are listed in Table II.

In general, the grain boundary resistivity is much higher than the bulk resistivity, even in the undoped material. This is ascribed to the fact that the grain boundary is disordered and the hopping of electrons is suppressed. The

dramatic increase in the resistivity of the grain boundaries when CaO is added is clearly shown, while the bulk resistivity does not change nor is the dielectric constant of the grain boundary phase affected.

II.B.4 Discussion

The addition of a small amount of CaO to MnZn-ferrite is known to form a secondary phase which is an intermediate compound of CaO and $(Mn,Zn)Fe_2O_4$; this secondary phase exists in an amorphous form. The capability of stopping magnetic domain wall motion in Ca-doped $(Mn,Zn)Fe_2O_4$ is ascribed to this amorphous phase; it acts as a non-magnetic barrier to the domain wall motion. In addition, the regions near the grain boundaries possess higher magnetic anisotropic energy such that the magnetization vectors can change directions only under large applied magnetic fields. This increase in magnetic anisotropic energy is a result of the lowering of the crystal symmetry due to localized strain from the partial dissolution of large Ca ions in the matrix.

The detrimental effect of CaO addition on the magnetic permeability is ascribed to the modification of grain boundary structure and its interaction with magnetic domain wall motion. The magnetic permeability is thought to be determined by the reversible movement of the domain walls rather than by domain rotation. Any microstructural feature which might hinder the domain wall motion will affect the magnetic permeability. Accordingly, an in-situ examination of the domain wall/microstructure interaction is essential in order to understand the magnetic behavior of the materials. This is made possible by Lorentz microscopy in TEM. More examples of the domain wall/microstructure interactions and the significance of the observations will be shown in the next chapter.

The formation of an insulating second phase along grain boundaries due to CaO addition increases the grain boundary resistivity drastically, while the intrinsic resistivity of the bulk material is not changed appreciably. The apparent electrical resistivity drops off rapidly in the high frequency regime caused by the capacitance (space charge polarization) effect of the grain boundary phase. Therefore, in order to improve the electrical behavior of the material, the intrinsic resistivity of the bulk material must be increased. In other words, the amount of ferrous ions, which is presumed to be responsible for the low resistivity of the bulk material, must be minimized. To achieve this, polycrystalline specimens were annealed in a controlled atmosphere. The details of the experiment and results will be described in Chapter 4.

II.B.5 Conclusion

The addition of small amounts of CaO is known to lead to the formation of an amorphous phase along grain boundaries. This secondary phase acts as a non-magnetic barrier to the magnetic domain wall motion. The partial dissolution of Ca ions into the matrix results in higher magnetic anisotropic energy, thus retarding the magnetic domain wall motion. On the other hand, the grain boundary phase acts as an electrical insulating layer. The blockage of electron transport is, however, ineffective in the high frequency regime due to space charge polarization in the material. Therefore, the Ca-addition in this material is not really beneficial to the electrical properties but only results in a detrimental effect to the magnetic properties.

III. INTERACTION OF MAGNETIC DOMAIN WALLS WITH MICROSTRUCTURE

III.1 Introduction

The magnetic properties of ferromagnetic and ferrimagnetic materials depend upon the chemical composition, crystal structures and also the microstructures of the materials. The recognition of the effect of microstructure on some of the magnetic properties has led to the development of various processing techniques and thermomagnetic treatment so as to optimize the microstructural variables for the desired combination of properties[11-38]. Actual studies of the effects of grain boundaries, grain sizes, pores, second phases etc., on coercivity, permeability, maximum energy product and other properties have also received considerable attention.

Development of various experimental techniques such as the Bitter technique, and the Kerr effect, have made it possible to directly examine the effect of microstructures on the domain wall configuration[90]. The development of Lorentz microscopy (in Transmission Electron Microscopy) has enabled magnetic domain walls to be imaged at higher resolution and also has made it possible to study the interaction of the microstructure with magnetic domains. In the latter technique, a magnetic field can be applied in-situ, so that the dynamics of domain wall motion and its interaction with the microstructures can be examined directly. Since the domain wall motion is related to many of the magnetic properties, such dynamic studies are of interest to understand the magnetic behavior of materials. In this chapter, the results of a study of the interaction of magnetic domain walls with grain boundaries, stacking faults, second phase precipitates, grain boundary segregates, pores and internal microcracks in some spinel ferrites are described.

The motion of domain wall is studied in-situ and the possible influence of such motion on the properties is discussed.

III.2. Experimental

Sintered (MnZn)Fe_2O_4 with and without CaO impurities and a flux-grown single crystal of $LiFe_5O_8$ were used for the present study. The detailed composition and processing history of (Mn,Zn)Fe_2O_4 can be found elsewhere[18]. The single crystal $LiFe_5O_8$ was heat treated in air for 1 hr. to obtain a two phase material[92]. Thin electron transparent specimens, suitable for transmission electron microscopy, were prepared from the bulk material by ion thinning technique. The Lorentz microscopy (LM) was done using a Philips EM301 microscope, operating at 100kV. Using the four lens system of the EM301, operated under LM mode, the microstructural image can be focused with the diffraction lens and the Lorentz image can be observed by defocusing the same lens.

A weak magnetic field can be applied to the specimen by exciting the objective lens of the microscope with a very low current. When the specimen is not tilted, the domain configuration will not be affected by the applied magnetic field which is perpendicular to the plane of the untilted specimen, since the magnetization vectors (M) of the specimen are confined to the plane of the specimen due to the shape anisotropy[90,91]. However, when the specimen is tilted slightly, the component of the applied magnetic field in parallel with the plane of specimen ($B_{||}$) will result in rotation of magnetization vectors and change the domain configuration. The strength of the parallel magnetic field ($B_{||}$) can be controlled by appropriate tilting of the specimen and the direction of the magnetic field ($B_{||}$) can be changed by simply rotating the specimen,

using a tilt-rotation holder.

The technique used for the in-situ observation of magnetic domain wall motion is a defocused method known as Fresnel Lorentz Microscopy. The detailed theory and principle of operation can be found elsewhere[75-80]. The simplified principle is shown in Fig. III.1. In the middle of the figure is a diagram of a thin section of a magnetic material. The domain walls are labelled as p-p and n-n, while the domains with their magnetization vector pointing outward are labelled S and those with their magnetization pointing inward are labelled N. The electron beam, upon passing through the specimen, will be subjected to a magnetic force perpendicular to the direction of incidence and the direction of magnetization of the domain. In other words, the electrons will be deflected toward or away from the domain wall resulting in a region which is either deficient or excessive in electrons directly under the domain walls.

When the microscope is focused onto the specimen, there will not be any new observable feature aside from the inherent defect structure of the material. However, when the microscope is overfocused (Fig. III.1c), a bright fringe will be observed for electron excessive regions (c-c) and a dark fringe will be observed for electron deficient regions (a-a,b-b). The positions of these bright and dark fringes correspond to the exact positions of the domain walls but their width has nothing to do with that of domain walls. When the microscope is underfocused (Fig. III.1a), the sense of the electron deficient and excessive regions is reversed as can be seen from the ray diagram. This reversal results in opposite contrast for the over- and underfocused condition. This complementary contrast of fringes in the two defocused conditions is especially important for in-situ observation of magnetic domain wall motion, since it provides a method for confirming that the observed fringes are magnetic do-

main walls rather than bend contours, grain boundaries, stacking faults or other kinds of planar defects.

III.3. Results and Interpretation

Under the application of a magnetic field, some of the domains will grow and some will shrink as a result of the rotation of magnetization vectors in the domains. The domain wall motion and their interaction with microstructural features can thus be examined. In the following figures, which show an applied magnetic field from top to bottom of each figure (except in the cases which are labeled by a negative number). A pair of domain configurations were shown for each stage of magnetization; the domain walls which appear as bright fringes in the over-focused situation, labeled O, are plotted as a solid line in the corresponding sketch, while those which appear as bright fringes in the underfocused condition, labeled U, are plotted as dashed lines. Defects such as grain boundaries and stacking faults are plotted as dotted lines.

(a) Effect of grain boundaries. The interaction of a domain wall with a grain boundary depends, among other things, on the angle between the domain wall and grain boundary. As shown in Fig. III.2, when the moving wall is parallel to the grain boundary, the boundary acts as a pinning site for the wall (wall 1 - 1, 2 - 2 and 3 - 3). On the other hand, if the wall makes an angle with the grain boundary, the motion of the wall is only retarded, there being the least retardation for walls normal to the grain boundary. When the grain boundary is inclined to the specimen surface, the effect is similar (wall 1 - 1 in Fig. III.3), since the domain wall is normal to the specimen surface which results from the fact that the magnetization vectors are confined to the plane of specimen due to shape anisotropy.

(b) Effect of grain boundary segregates. In the case of materials containing an intergranular phase, as the domain wall approaches the boundary,

its motion is retarded and the wall stops at a distance from the boundary (wall 1 - 1 in Fig. III.4 stages 1 and 2). As the applied field is increased, the wall suddenly "jumps" as a result of magnetization reversal by rotation in the region between the grain boundary and the impeded wall (wall 1 - 1 in Fig. III.4, stage 3). Domains are also nucleated at these grain boundaries and at junctions containing the second phase (domain C in Fig. III.4, stage 2). When the applied magnetic field is reduced, the domain wall motion is not reversed. For example, domain wall 1 - 1 (Fig. III.4, stage $\overline{4}$) does not retreat; instead, it splits and nucleates a new closure domain E and domain wall 4 - 4 cannot move at all until a new domain is nucleated.

(c) Effect of pores and cracks. Pores and cracks are regions where the material has a small enclosed free surface. As shown in Fig. III.5, pores act as pinning sites for domain walls in (MnZn)Fe_2O_4. Similarly, a crack can stop a moving domain wall (Fig. III.6). It is observed that, unlike the case of grain boundaries, a domain wall moves continuously towards the crack until it is finally pinned. Since small pores can be found in many ceramics, not only at the grain boundaries, but also inside the grains, the effective distance between the domain wall barriers will be reduced.

(d) Effect of second phases. The size and nature of the second phase determine the effect it may have on the motion of domain walls. The nonmagnetic $LiFeO_2$ precipitates in $LiFe_5O_8$ (d,e,g, Fig. II.7) can act as barriers to domain wall motion (wall 1 - 1) or as sites for nucleation of reverse domains (domain B in stage 1 and C in stage 3). It is observed that if the precipitate is too small (< 300nm), it acts only as a barrier to the wall motion. However, if the precipitate is too large, the semicoherent interface acts as a site for nucleating the reverse domain in addition to pinning the domain walls. The

effectiveness on enhancing the coercivity in both cases will not be as good as in the case where only coherent precipitates are present.

(e) Effect of stacking faults. The most common stacking faults found in spinel ferrites are {110} cation faults [93] and several of these faults can be seen in Fig. III.8. The Lorentz image of the corresponding area shows that the magnetic domain walls are pinned to the faults and each faulted region has a domain attached to it. This occurs as a result of modification of the cation arrangement by the faults such that the superexchange interaction is enhanced[94]. Also it can be seen that as a magnetic field is applied, new domains such as (a) are created at the stacking fault and the domain wall away from the fault (wall 2 - 2) sweeps through the unfaulted region easily. The wall close to the stacking fault (wall 3 - 3) is not able to move across the fault. In some unfaulted regions the magnetization can only be reversed as a whole (domain b).

III.4. Discussion

The typical microstructure of a ceramic ferrite contains grain boundaries, cracks, pores, etc.. It has been recognized that grain boundaries act as barriers to domain wall motion. The retarding behavior of grain boundaries depends upon whether the boundaries have any segregates or not. In the case of $(Mn,Zn)Fe_2O_4$ containing CaO additives, it has been shown that the Ca rich intergranular phase strains the spinel lattice in the vicinity of the boundary. This, in turn, leads to a higher anisotropic energy, or a stronger coupling between the magnetic moment and the lattice, such that the magnetization vector rotates only when a sufficiently large field is applied. Such a material inevitably will have a higher coercivity and lower permeability compared to

materials with no intergranular phase or strain centers near the grain boundaries.

The formation of reverse domains at pores and second phases are due to the demagnetizing field at these inhomogeneities[5]. When the precipitate or pore is large, the demagnetizing field will be large enough to magnetize the region of the material near the inhomogeneities in a direction reverse to the surrounding magnetic domain. The reversal of the magnetization vector of this domain, under the action of an applied magnetic field, is facilitated by the presence of reverse domains near inhomogeneities. Thus materials containing these large precipitates are expected to have lower coercivity compared to those materials which contain coherent precipitates only.

The formation of a nonmagnetic second phase can be used in some ceramic systems to enhance the coercivity or modify the shape of the hysteresis loop. However, the size and distribution of the precipitates must be precisely controlled since they determine the effect the precipitates may have on magnetic domain wall motion. This can be achieved by manipulating the composition of materials and thermal processing. Moreover, the existence of pores and microcracks must be taken into account when designing the processing schemes of ceramic ferrites, since these features act as barriers to domain wall motion. For instance, if either pores or microcracks are present within the grains and not only at the grain boundaries, the distance over which a wall can travel without any obstacle is shortened and the effective grain size is reduced.

Finally, it must be emphasized that the above observations are only qualitative. In order to make quantitative studies of domain wall motion vs. applied magnetic field, a specially designed stage with proper field compensation is needed. In addition, the domain wall/microstructural feature inter-

actions which actually happen in bulk materials will not be exactly the same as that seen in thin foils. As the thickness of the specimen is diminished from the bulk materials, the magneto-static energy becomes more important than the anisotropic energy such that the magnetization vectors are confined to the plane of the foil. In other words, the preferred directions on which the magnetization vectors tend to lie are not the same as the easy axes of the bulk materials. The response of the domain walls to the applied magnetic field is, therefore, expected to be different. Meanwhile, the effect of pores and second phases on retarding the domain wall motion in the bulk materials will not be as large as that observed in thin foils. The size of these defects is often small compared to the dimensions of the domain wall in bulk materials, while they are of comparable size in the case of thin foils. It is thus very important to bear these in mind when attempting to correlate the observed domain wall/microstructural feature interaction, in the thin foil, with the magnetic behavior of bulk materials.

III.5. Conclusions

The interaction of magnetic domain walls with various microstructural features has been examined by Lorentz microscopy in TEM. All the microstructural defects, such as grain boundaries, pores, cracks, second phase precipitates and stacking faults, are observed to affect the dynamic behavior of domain walls. They act not only as barriers for domain wall motion, but also as nucleation sites for domains in reverse magnetization.

The retarding behavior depends upon the nature of the defects and is ascribed either to the formation of nonmagnetic phases or to an increase in the anisotropy energy. The nucleation of domains in reverse magnetization, on the

other hand, is attributed to the presence of a demagnetization field at the inhomogeneities. The influence of the existence of these microstructural defects on the magnetic properties of the materials has been discussed, based upon the observed domain wall/microstructure interactions.

IV. CONTROLLED ATMOSPHERE ANNEALING

IV.1. Introduction

The outstanding characteristic of ferrites, as compared with magnetically soft alloys such as silicon iron and permalloy, is that they combine extremely high electrical resistivity with reasonably good magnetic properties. These materials can thus be used at high frequencies with virtually no eddy current loss, a factor which renders the metal cores completely useless. The eddy current induced by the high frequency alternating magnetic field not only reduces the effective magnetic flux imposed upon the magnetic specimen but also produces a direct power loss in the form of electrical heat. Increasing the electrical resistivity is necessary to minimize the eddy current losses of the ferrite materials. A small amount of CaO has been added in MnZn-ferrite to raise the electrical resistivity through the formation of an insulating layer along the grain boundaries[18]. While the electrical resistivity of the specimens is improved drastically at low operating frequencies as a result of CaO addition, the space charge polarization effect renders the insulating layer completely useless at high operating frequencies (cf. Chapter II.B). Therefore, for high frequency performance, it is necessary to increase the electrical resistivity of the bulk material, rather than that of grain boundary layers.

The basic electron conduction mechanisms in ferrites have been studied by many investigators[95-97] and reviewed by Klinger et al.[98]. Among the various models proposed, such as the standard band theory model, a small-polaron mechanism, and the thermally activated hopping model, the latter model has the merit of simplicity and has been well applied to explain qualitatively the electrical behavior of MnZn-ferrites. The extra electron on a ferrous (Fe^{2+}) ion requires little energy to move to an adjacent ferric (Fe^{3+}) ion

sitting in a similar interstitital site. Under the influence of the electric field, these extra electrons, hopping from one iron ion to the next, constitute the electrical conduction. The ferrous ions are thus acting as donors in this semiconducting material. The minimization of the divalent iron content in MnZn-ferrite is, therefore, a more radical approach to increase the intrinsic resistivity of the bulk materials. Furthermore, it eliminates side effects such as the localized strain induced by CaO additions.

The equilibrium Fe^{2+}content in MnZn-ferrite is known to be sensitive to the oxygen partial pressure of the environment at high temperatures[99-104]. Control of the amount of divalent iron in polycrystalline material can thereby be achieved by annealing the specimens in an atmosphere with controlled PO_2 level. Specimens having low resistivity (high divalent iron content) were annealed in a controlled atmosphere to reduce the Fe^{2+} content. The results of the heat treatment, the effect of annealing upon electrical and magnetic properties, and the significance of these observations are discussed in this chapter.

IV.2. Experimental

Commercial high magnetic permeability material (type B MnZn-ferrite) was used to study the effect of controlled atmosphere annealing on the electrical and magnetic properties, since this type of material possesses low electrical resistivity. The shape and dimensions of the sample have been described previously (cf. chapter II.B).

Since the oxidation state of the iron ions is very sensitive to the oxygen partial pressure of the atmosphere at annealing temperature, the heat treatment must proceed in a strictly controlled environment. A furnace

system, in which both the temperature and oxygen partial pressure can be precisely controlled, was thereby constructed for this purpose. The temperature of the platinum tube furnace was monitored by Eurotherm model 211 temperature programmer/controller and was measured by Pt-Pt10%Rh thermocouples. The PO_2 level of the annealing atmosphere was varied by carefully adjusting the flow rate of the inlet nitrogen and oxygen (or air) gas. The flow rates were controlled/monitored by a Tycon model FC-260 gas controller. A Westinghouse Model 209 oxygen analyzer was used to measure the exact oxygen partial pressure of the gas mixture after it reacted with the specimens in the furnace.

The annealing conditions were determined from the thermodynamic data derived by other investigators[102-104]. The temperature of the furnace was increased slowly to 1100°C, and retained at this annealing temperature for eight hours to ensure the completeness of oxidation-reduction reaction and then specimens were cooled at a rate of 200°C/hr. The annealing atmosphere was maintained at the same level during the heating cycle. The PO_2 levels used in annealing are indicated in the corresponding figures to be discussed shortly.

The ferrous ion content of the specimens was determined by titration[105-107]. The oxidation of Fe^{2+} during titration was avoided by dissolving the sample in an inert atmosphere in a sealed tube. Concentrated HCl (2ml) acid contained in an ampoule was deoxygenated by bubbling nitrogen through it just before, and after the sample was inserted. The sample-containing ampoule was sealed immediately and subsequently immersed in 100°C water to dissolve the sample; 2-10 hrs is necessary for MnZn-ferrite materials. The solution containing the dissolved sample was mixed with a 30ml deoxygenated matrix solution consisting of 1M H_2SO_4 and 0.5M HPO_4. The mixture was then titrated

with 0.004871M ceric sulfate acid, the end point being determined by a barium diphenylamine indicator. A standard solution, which was made by dissolving $Fe(NH_4)_2SO_4.6H_2O$ in 0.5M H_2SO_4, was titrated in each run to calibrate the solutions used.

The electrical and magnetic properties of the specimens were calculated from the measured impedance, as described in Chapter II.B and appendix.

IV.3. Results and Discussion

(a) Effect of annealing on ferrous (Fe^{2+}) ion content. As shown in Fig. IV.1, the ferrous ion content of the specimens changes as a result of annealing. It decreases when a high oxygen partial pressure (PO_2) is used for annealing; a low oxygen partial pressure results in increased ferrous ion concentration. The Fe^{2+} concentration of an unannealed specimen, labelled S in the figure, is included for comparison. The oxidation of ferrous ions is more sensitive to the PO_2 level in the low Fe^{2+} region than in the high Fe^{2+} region. Only a small change in the degree of oxidation results from a large change of the PO_2 level in the high Fe^{2+} region, while a large change in the degree of oxidation is produced by the same change of the PO_2 level in the low Fe^{2+} region. The control of divalent iron content at a low level is more difficult; stringent control of the PO_2 level during annealing is necessary in this region.

A model for oxidation-reduction equilibria in MnZn-ferrite has been proposed by Morineau et al.[104]. In the model, equilibrium equations between ions, defects and oxygen partial pressure are suggested, taking into account the site preference of different cations. The model fits their data very well[102]. An Fe^{2+}/PO_2 response curve corresponding to 1100°C annealing temperature obtained by the same authors[103] using thermogravimetric measurement is

shown as a dashed line in Fig. IV.1. The trends in the change of ferrous ion content with PO_2 levels in their study are similar to those reported above. Discrepancies arise mainly from the difference in specimen composition and morphology. The specimens used in this study contain smaller amounts of MnO and are polycrystalline. The presence of multivalent Mn ions affects the oxidation-reduction behavior of iron ions[108] and the reaction in polycrystalline materials is much slower than in powder due to the slow diffusion through the sintered specimens.

The annealing temperature can also affect the degree of oxidation of the heat treated specimens. For constant oxygen partial pressure, the ferrous ion content is higher for a specimen annealed at higher temperature (light dashed line in Fig. IV.1). It also has been observed that there exists a phase boundary corresponding to each annealing temperature, indicated as shaded lines in Fig. IV.1. The secondary phases such as Fe_2O_3 (hematite) or Mn_2O_3 might precipitate if the PO_2 level of the annealing atmosphere is higher than that of the phase boundary. When the annealing temperature increases, the critical PO_2 level also increases and the critical divalent ion content decreases, as indicated by the arrows in Fig. IV.1.

The consequence of this behavior is that the divalent iron content of the specimen will decrease when it is cooled from high temperature with oxygen partial pressure kept at a constant level. In the extreme case where the Fe^{2+} content of the specimen is too low, the phase boundary will be encountered during cooling and either precipitation will occur or the high temperature structure will remain as a metastable phase at room temperature. Both enhanced oxidation and precipitation of the secondary phase will have detrimental effects on the magnetic properties of the material; both are likely to occur

preferentially along grain boundaries in polycrystalline specimens. This will be discussed shortly.

(b) Effects of annealing on electrical resistivity. The apparent resistivities (ρ_p) of the annealed type B specimens are plotted versus operating frequencies (the dispersions) and are shown in Fig. IV.2 as solid lines with the annealing PO_2 level indicated. The dispersion curves of unannealed type A and type B materials are also included for the convenience of comparison and are plotted as dotted and dash-dotted lines respectively. In general, a higher apparent resistivity (ρ_p) was obtained for the specimen annealed in a higher PO_2 level. The resistivity has been raised as much as two orders of magnitude for the specimen annealed in 7000 ppm oxygen partial pressure. It is even higher than the resistivity of low loss MnZn-ferrite (type A). On the other hand, the resistivity is lowered when the specimen is annealed in a PO_2 level lower than 300ppm.

The increase in apparent resistivity as a result of annealing is attributed to the oxidation of ferrous (Fe^{2+}) ions to ferric (Fe^{3+}) ions, while the decrease in apparent resistivity is ascribed to the reverse reaction, i.e. reduction of ferric ions to ferrous ions. The variation of apparent resistivity with divalent iron content is shown in Fig. IV.3 for low and moderately high operating frequencies (freq. < 1KHz = 1 MHz). The data labelled Sa and Sb are the resistivities of type A and type B untreated materials respectively. The accompanying question marks (?) indicate that the data are included only for comparing the resistivity of the material, while the amount of Fe^{2+} contained in the specimen is not the same as the corresponding value represented by the data point. The behavior by which the apparent resistivity of the specimen increases as the amount of divalent iron decreases, is in agreement with the

hopping model of electrical conduction in MnZn-ferrite[98]. The ferrous ions can be considered as donors containing an extra electron, which will jump to the adjacent ferric ions easily and constitute the electrical conduction. The oxidation of divalent iron by annealing reduces the donor concentration in the material such that the electrical resistivity increases.

The apparent resistivity drops off in the high frequency regime (Fig. IV.2) and is more prominent for high resistivity material. This behavior is similar to that of type A material (cf. Chapter II.B) and is an indication that the annealed type B material consists of low resistivity bulk materials separated by high resistivity layers, presumably the grain boundary phase. The space charge polarization occurs at high operating frequencies and short circuits the high resistivity layers causing the apparent resistivity to drop off rapidly. The electrical behavior of the presumed grain boundary layers can be separated from the bulk materials by the complex-impedance technique, described in detail in the appendix.

Analysis of the impedance data of the specimens using the above-mentioned technique shows that both the bulk and grain boundary resistances of the annealed specimens increase as the Fe^{2+} concentration decreases (Fig. IV.4). The improvement of the electrical behavior due to annealing is much more prominent in the grain boundary phases than in the bulk materials. The marked difference of annealing effect is even more clearly demonstrated when the specific resistance (resistivity) of the two phases are plotted against divalent iron content, as shown in Fig. IV.5. The grain boundary resistivity is seen to be at least three orders of magnitude higher than the bulk resistivity, and it increases much more rapidly as the ferrous ion content of the specimen decreases. The fact that the grain boundary phases contain less divalent iron

than the bulk materials as a result of annealing is strongly implied. The preferential oxidation along grain boundaries during annealing can thus be concluded.

The dielectric constant of the grain boundary phases, as analyzed by the complex impedance technique, does not change appreciably with the specimens and is in the range of 15 ε_o to 40 ε_o, where ε_o is the dielectric constant of free space. The bulk resistance is observed to be comparable with the overall grain boundary resistance for all the specimens (Fig. IV.4), although the exact resistivity of the bulk materials is much lower than that of grain boundary phases (Fig. IV.6). These observations are consistent with the assumptions made in modelling the electrical response of the polycrystalline MnZn-ferrite (cf. appendix). That is, the grain boundary phases are thin layers of high resistivity materials while the bulk materials are low resistivity materials.

(c) Effect of annealing on magnetic properties. The high magnetic permeability (μ') and low magnetic loss (μ'') are the two most important magnetic properties desired for MnZn-ferrite. While the eddy current loss is improved due to the increase in resistivity, the magnetic permeability of the material is, unfortunately, lowered as a result of controlled atmosphere annealing (Fig. IV 6a). The $\tan\delta$, which describes the ratios of dissipated energy to stored energy, and the magnetic loss (μ'') are, however, improved by annealing (Fig. IV.6b,c).

In the figures showing the dispersion of magnetic properties, the curves are plotted as solid lines, with the PO_2 level indicated, for annealed samples and are plotted as dotted and dash-dotted lines for unannealed type A and type B specimens respectively. The magnetic permeability (μ'), loss (μ'') and $\tan\delta$ are all decreased as a result of annealing; the amount of change is larger for

specimens heat treated at higher oxygen partial pressures. In other words, all the magnetic responses are suppressed when the ferrous ion concentration in the specimens is reduced. The dependence of these magnetic properties on the divalent iron content is shown in Fig. IV.7. The magnetic permeabilities (μ') are plotted as solid lines for two operating frequencies (1 KHz and 100 KHz); the maximum magnetic loss (μ''_{max}) is plotted as a dash-dotted line; and the tan δ is shown as a dotted line for 6 Meg.Hz operating frequency.

It is interesting to notice that for the specimen annealed in 4800ppm oxygen partial pressure, all the resultant magnetic properties are the same as those of the unannealed type A material, within the error of measurement. The effect of annealing on the grain boundary structure/composition is thus suggested to be similar to that of CaO addition. The degree of modification of the grain boundary characteristics and properties can, however, be controlled by using the appropriate PO_2 level of the annealing atmosphere.

While the dependence of electrical resistivity on ferrous ion content can be well explained by the electron hopping mechanism, the dependence of magnetic permeability on the divalent iron content is totally unclear and a mechanism which can predict this behavior is not well-established[109-116]. Although there are reports concerning the variation of permeability with Fe^{2+} concentration[117-121], the observations are still far from conclusive. The investigation on this aspect and exploration of the basic mechanisms are necessary. The degradation of the permeability as a result of annealing observed in this study can, however, be explained by preferential oxidation of ferrous ions at regions near grain boundaries.

In polycrystalline materials, the diffusion of ionic species along grain boundaries is known to be much faster than the diffusion in the bulk mater-

ials[122-125]. The grain boundary regions are, therefore, expected to be oxidized more readily when sintered MnZn-ferrite specimens are annealed in a controlled atmosphere. Since the formation of cationic vacancies is inevitable when oxidation takes place in the spinel lattice, as more anions are bound to ferric ions than to ferrous ions, a dilation of lattice parameter (a_o) in the oxidized regions is expected[126]. Localized strain will be induced when there are regions which are oxidized preferentially to their adjacent regions. The magnetic anisotropy energy in those regions will thus be increased and domain wall mobility lowered.

The preferential oxidation of grain boundary phases is enhanced when the oxygen partial pressure is kept at a constant level during cooling. The equilibrium Fe^{2+} concentration is decreasing with the temperature and diffusion is fast enough to reach equilibrium only in the grain boundary region. This will lead to a higher magnetic anisotropy energy in the regions near the grain boundaries. Although the separate measurement of divalent iron content in the bulk material and grain boundary phase is practically impossible by current techniques, the fact that the grain boundary phase contains fewer ferrous ions is strongly implied by the overwhelmingly high resistivity of the grain boundary phase. The decrease in permeability due to annealing can, therefore, be ascribed to the local strain in the regions near the grain boundaries induced by preferential oxidation.

IV.4. Conclusion

Controlled atmosphere annealing is capable of improving the apparent resistivity (ρ_p) of the MnZn-ferrite sintered material through the reduction of the ferrous ion content. The annealing effect is more pronounced on grain

boundary phases than on bulk materials. The magnetic permeability (μ') is, however, degraded due to annealing and is ascribed to the preferential oxidation along grain boundaries in polycrystalline specimens.

The electrical resistivity of the materials could be improved without seriously deteriorating the magnetic permeability if the inhomogeneity in oxidation could be eliminated. In other words, a stringent control of the oxygen partial pressure at an earlier stage of processing rather than post fabrication annealing is called for, in order to raise the intrinsic electrical resistivity of the bulk materials by reducing Fe^{2+} concentration and not affect the magnetic permeability detrimentally.

V. CONCLUDING REMARKS

The grain boundaries and the regions near them have been shown to influence the magnetic and electrical properties of MnZn-ferrites by virtue of their physical and chemical nature. They affect the properties through (i) providing a region where impurities may segregate or liquid phase may form (cf. Chapter IIa), (ii) acting as high resistivity and non-magnetic layers, (iii) increasing the magnetic anisotropy energy in the nearby regions (cf. Chapter IIb), and (iv) providing an easy path for oxygen diffusion and producing the oxidation of Fe^{2+} to Fe^{3+} near grain boundaries (cf. Chapter IV).

In addition to the understanding of grain boundary effects, there are other factors which must be known in order to be able to tailor the materials to the desired properties. Zinc-depletion, both at the surfaces of the specimens and at the grain boundaries, has been reported[119,127-129]. The correlation between Zn-depletion and permeability degradation is, however, still unexplained and the observations reported are not consistent. Furthermore, more needs be known about the exact role of powder characteristics, additives and binders on influencing the microstructure and hence the properties of the materials[130-136]. The divalent ion content has been observed to affect the magnetic properties[117-121]. The observations are still far from conclusive and the basic mechanisms of interaction are not well understood. Further exploration of these factors is necessary.

The understanding of microstructure/properties interaction is still far from complete. Nevertheless, some conclusions can be made from the observations in this study, i.e. in order to achieve the goal of making high permeability and low loss MnZn ferrite material, the elimination of grain boundary segregation and internal pores, and the optimization of ferrous (Fe^{2+}) ion content are

necessary. Grain boundary segregation and pores have been observed to hinder magnetic domain wall motion and hence decrease the permeability, while the divalent iron concentration has been found to affect the electrical resistivity.

The use of high purity raw material to prevent the segregation at grain boundaries and the modification of the production processing scheme to avoid the formation of internal pores are essential to improve magnetic permeability. These conclusions arise from the fact that CaO addition in type A material was observed to result in grain boundary segregation; rapid rising of sintering temperature in processing type B material was found to lead to the formation of internal pores.

Moreover, the optimum ferrous ion concentration should be controlled in order to raise the electrical resistivity but not seriously deteriorate the magnetic properties. The optimum Fe^{2+} concentration can be obtained, without inducing any inhomogeneity, by stringent control of oxygen partial pressure of the environment, at early stages of processing. The Fe^{2+} content/PO_2 level equilibria, however, must be established for the specific material under study, since it is composition sensitive[102-104]. The preferential oxidation and second phase precipitation at grain boundaries must be prevented by programming the cooling conditions carefully; the divalent ion concentration varies sensitively with temperature and environmental PO_2 level, and diffusion along the grain boundaries is rapid.

In summary, the optimum magnetic and electrical properties of the MnZn-ferrite can be obtained by using high purity material and careful control of processing parameters such that both the microstructure and chemical composition, including Fe^{2+} content, can be optimized.

APPENDIX: Complex Impedance (Admittance) Technique for Magnetic and Electrical Measurement

A.1. Magnetic Measurement

Initial permeability (μ_i), which is the most important magnetic property desired in MnZn-ferrite, is believed to arise as a result of reversible displacements of magnetic domain walls within the materials. Rotation of spins within a domain, referred to as domain rotations, contribute little due to the magnetocrystalline anisotropy[109-117]. In a sinusoidally varying magnetic field, a phase angle δ arises between the magnetic field (H) and the magnetic induction (B) due to energy losses associated with magnetic resonance and relaxation phenomena. Such losses, resulting physically from the reorientation of the of the magnetic moments, can be described phenomenologically by a complex permeability:

$$\mu_i^* = \mu' - j\mu'' \qquad \text{(A1.1)}$$

The real part μ' describes the stored energy and the imaginary part μ'' describes the energy dissipated apart from hysteresis loss and eddy-current loss. The dissipated energy can be described by a loss factor, $\tan\delta$:

$$\tan\delta = \frac{\mu''}{\mu'} \qquad \text{(A1.2a)}$$

or by a normalized loss factor

$$\frac{\tan\delta}{\mu'} = \frac{\mu''}{(\mu')^2} \qquad \text{(A1.2b)}$$

Both stored energy μ' and dissipated energy μ' are found to be frequency dependent. In certain high frequency regions permeability drops off and magnetic losses increase because of magnetic resonance.

The complex permeability (μ^*) can be derived from the complex impedance of a coil wound on the magnetic materials; a toroidal geometry is usually used to avoid demagnetization effects. The self-inductance of the coil, on the insertion of the magnetic core with complex permeability μ^*, will be $\mu^* L_o$. The complex impedance (Z) of this coil is then expressed as

$$Z = R + jX = j\omega L_o \mu^* = j\omega L_o(\mu' - J\mu'') \qquad \text{(A1.3)}$$

The permeability μ'' is related to the reactive part by

$$\mu' = \frac{X}{\omega L_o} \ , \qquad \text{(A1.4a)}$$

and the magnetic loss μ'' to the resistive part by

$$\mu'' = \frac{R}{\omega L_o} \ , \quad \omega = 2\pi f \ , \qquad \text{(A1.4b)}$$

where f is the measuring frequency. L_o is the inductance of a toroid with a nonmagnetic core and is derived geometrically[137] (Fig. A1)

$$L_o = 0.2972\, N^2 h \log \frac{d_o}{d_i} \quad \text{(microhenrys)}$$

where N is the number of the turns of the coil; h, d_o and d_i are the thickness, outside diameter and inside diameter (in mm) of the toroid, respectively.

A.2. Electrical Measurement

A.2.1. Equivalent Circuit.

Measurements of frequency-dependent complex impedance of the specimen permit one to separate the electrical behavior of the grain boundary phase from that of the bulk material in polycrystalline ceramic specimens under ideal conditions. Interpretation of the results is based on being able to represent the sample by an equivalent circuit. Complex impedance techniques have been successfully applied to the characterization of polycrystalline solid electrolytes[89,138-143]. The modelling of this sample, however, must be modified. The various physical processes which enter into the conduction mechanisms in the polycrystalline MnZn-ferrite must all be considered.

In general, a single phase ceramic materials can be mathematically described as dielectric materials with complex dielectric constants[137,138]. The imaginary part of the dielectric constant is associated with dielectric losses which sum over all dissipative effects. The material response can also be mathematically formulated on the basis of complex conductivity. These approaches are similar in that they describe the material by an equivalent circuit consisting of a parallel combination of a resistance and capacitance (Fig. A2). In other words, the response of a single phase material can be represented by a dielectric constant ε and a dielectric conductivity σ (or resistivity ρ).

In polycrystalline ceramic materials, the grain boundary phase often exhibits different behavior from the bulk material, such that two R-C lumped circuits, one for the grain boundary phase and the other for the bulk material,

are necessary to describe the material response. The complicated microstructure of the polycrystalline material often makes modelling of the material by an equivalent circuit practically impossible. Fortunately, the situation is less serious in the case of the MnZn-ferrite, in which the bulk conductivity is significantly higher than that of the grain boundary phase. Simplification is, however, still necessary in order to model this material by an equivalent circuit.

A polycrystalline MnZn-ferrite is simplified by a cubic microstructure shown in Fig. A3a, where all grains are assumed to be identical with grain boundaries of uniform thickness. The behavior of the top layer will be considered first and the rest added later. The top layer contains cubic grains separated by grain boundaries (Fig. A.3.b); each of them can be represented by a lumped circuit: r_2 and C_2 for grains and r_1 and C_1 for grain boundaries. The response of these layers is equivalent to the parallel combination of these lumped circuits.

For a unit consisting of only one grain and its surrounding grain boundaries, indicated by dashed lines in Fig. A.3b, the resultant resistance and capacitance is:

$$r' = \frac{1}{r_1} + \frac{1}{r_2} \quad \text{where} \quad r_i = \rho_i \frac{d_i}{A_i}$$

$$c' = c_1 + c_2 \qquad c_i = \varepsilon_i \frac{A_i}{i} \qquad \text{(A2.1)}$$

i = 1 for grain boundary; 2 for grain, respectively.

ρ_i, ε_i, d_i and A_i are resistivity, dielectric constant, length and cross-sectional area, respectively.

In this special case,

$$\frac{A_1}{A_2} = \frac{2\ell_1\ell_2}{\ell_2^2} = 2x \qquad (\ell_1 = x\ell_2) \qquad \text{(A2.2)}$$

$$d_1 = d_2 = \ell_2$$

Since the bulk material is assumed to be much more conductive than the grain boundary phase ($\sigma_2 \gg \sigma_1$ or $\rho_1 \gg \rho_2$) and the thickness of the grain boundary is much smaller than the grain size ($x \ll 1$),

$$\frac{r_1}{r_2} = (\rho_1 \frac{d_1}{A_1})/(\rho_2 \frac{d_2}{A_2}) = \frac{\rho_1}{\rho_2} \frac{1}{2x} \gg 1 \qquad r' \simeq r_2$$

and (A2.3)

$$\frac{c_1}{c_2} = (\varepsilon_1 \frac{A_1}{d_1})/(\varepsilon_2 \frac{A_2}{d_2}) = \frac{\varepsilon_1}{\varepsilon_2} 2x \ll 1 \qquad c' \simeq c_2$$

Therefore, the contribution of the grain boundary phase to overall resistance and capacitance in this layer is negligible; any layer having this microstructure can be approximated by a layer consisting of bulk material only. Thus, polycrystalline materials can be modelled more simply by sections of bulk material separated by thin layers of grain boundary phase (Fig. A.3c) and represented by a series combination of lumped circuits. The resistance and capacitance of bulk material sections (layer 2) are:

$$r_b = \rho_2 \frac{\ell_2}{A} \qquad \text{(A2.4a)}$$

$$c_b = \varepsilon_2 \frac{A}{\ell_2}$$

where A is the cross-sectional area of sample and ℓ_2 the grain size and of grain boundary layers (layer 1) are

$$r_g = \rho_1 \frac{\ell_1}{A}$$
$$c_g = \varepsilon_1 \frac{A}{\ell_1} \qquad \text{(A2.4b)}$$

where ℓ_1 is the thickness of the grain boundaries.

Since the size of the grains (ℓ_2) is much larger than the thickness of the grain boundaries (ℓ_1), the total resistance contribution from the bulk layers is comparable to the total contribution from grain boundary layers. This is true, even though the resistivity of the bulk material (ρ_2) is much smaller than that of the grain boundary phase (ρ_1) since they are connected in series. For the same reason, the overall capacitance of the bulk layers is small compared to that of the grain boundary layers, since the dielectric constant does not vary appreciably with material. (This is true for ceramics in general, but not in the case of ferroelectric materials.) Also, the reactance resulting from the bulk capacitance ($1/\omega C_b$), connected in parallel with the bulk resistance, may be neglected since it is large compared with the bulk resistance (r_b) for moderately high operating frequencies ($f \leq 10$ Meg Hz). This leads to a simple equivalent circuit for semiconducting MnZn-ferrite specimens, namely, a series combination of bulk materials (R_2) and the grain boundary lumped circuit, which consists of a parallel combination of resistance (R_1) and capacitance (C_1)(Fig. A3c).

$$R_2 = nr_b;\ R_1 = nr_g \text{ and } C_1 = \frac{1}{n} c_g \qquad \text{(A2.5)}$$

where n is the number of grains in the length of specimen.

The characteristic parameters of the materials, namely, R_1, C_1, and R_2, can be obtained from the complex impedance plot, which is generated by

measuring the complex impedance of the sample over a broad range of frequencies.

A.2.2. Characteristic Parameters

The impedance of the equivalent circuit in Fig. A3c can be found by standard circuit analysis and will be a complex function of frequency. If the apparent resistance (R) is plotted against the apparent reactance (X) over a broad range of frequencies, a semicircle results with its center on the R-axis (Fig. A4a). The intercepts on the R axis give the DC resistance and the infinite frequency resistance. The former corresponds to a sum of grain boundary and bulk resistance ($R_1 + R_2$), since the grain boundary capacitance (C_1) acts as an open circuit at DC. The latter corresponds to the bulk resistance (R_2) since the grain boundary resistance is short-circuited by the grain boundary capacitance at infinite frequency. Both the grain boundary and bulk resistance can thus be obtained by extrapolating the R-X plot toward DC and toward high frequency, respectively. The grain boundary capacitance can be calculated from the formula $2\pi f_o R_1 C_1 = 1$, where f_o is the frequency at which the maximum of the R-X plot occurs.

Complex admittance may also be used to represent sample response. The characteristic parameters of the sample can be obtained from the interceptions and the maximum of the complex admittance plot, in which the conductance G is plotted against the susceptance B (Fig. A4b). The choice of representation depends on the behavior of the specimen. In some cases the determination of the characteristic parameters may be facilitated by employing the complex admittance representation. However, for a sample with exceptionally high grain boundary resistance, such as MnZn-ferrite, the complex impedance

representation is preferable. Since the intercept on the impedance plot (R_1 + R_2) is very far from the origin, extrapolation from the observed data will generally result in smaller uncertainties.

A more elaborate approach used by Koops[89] for analyzing these characteristic parameters is by fitting the complex impedance data with the complicated theoretical curve. In this method the apparent resistivity (ρ_p) and the apparent dielectric constant (ε_p) of the materials are expressed in terms of grain boundary /bulk resistivity and dielectric constant:

for resistivity

$$\rho_p = \rho_p^{\infty} + \frac{\rho_p^0 - \rho_p^{\infty}}{1 + \tau_p^2\omega^2}$$

with

$$\rho_p^{\infty} = \frac{\rho_1\rho_2(\varepsilon_1 + x\varepsilon_2)^2}{\rho_1\varepsilon_1^2 + x\rho_2\varepsilon_2^2}$$

$$\rho_p^0 = x\rho_1 + \rho_2 \qquad \text{(A2.6a)}$$

$$\tau_p = \left[\frac{\rho_1\rho_2(\rho_1\varepsilon_1^2 + x\rho_2\varepsilon_2^2)}{x\rho_1 + \rho_2}\right]^{1/2}$$

and for the dielectric constant

$$\varepsilon_p = \varepsilon_p^{\infty} + \frac{\varepsilon_p^0 - \varepsilon_p^{\infty}}{1 + \tau_\varepsilon^2\omega^2}$$

with

$$\varepsilon_p^{\infty} = \frac{\varepsilon_1 \varepsilon_2}{\varepsilon_1 + x\varepsilon_2}$$

$$\varepsilon_p^{o} = \frac{x\rho_1^{\,2}\varepsilon_1 + \rho_2^{\,2}\varepsilon_2}{(x_{\,1} + {}_{2})^2} \qquad \text{(A2.6b)}$$

$$\tau_\varepsilon = \frac{\rho_1\rho_2(\varepsilon_1 + x\varepsilon_2)}{x\rho_1 + \rho_2}$$

where ρ_1, ε_1 are the resistivity and dielectric constant of the grain boundary phase

ρ_2, ε_2 are the resistivity and dielectric constant of the bulk material

x is the ratio of the thickness of the grain boundaries to the size of the grains

The apparent resistivity (ρ_p) and dielectric constant (ε_p) are calculated from the measured impedance using the formula

$$R = \rho_p \frac{L}{A}\,; \qquad c = \varepsilon_p \frac{A}{L} \qquad \text{(A2.7)}$$

where L and A are the overall length and the cross-sectional area of the specimen, respectively.

The complex impedance technique, though not as precise when compared with Koops' elaborate approach, is still preferable because of its simplicity. It is capable of analyzing the characteristic parameters of the material without tedious data-fitting processes. Furthermore, it demonstrates more clearly the physical significance of the analyzing process.

A.2.3. Discussion

The measurement of complex impedance is a useful tool for isolating bulk and interfacial phenomena. However, considerable uncertainty still remains with respect to the adequacy and uniqueness of the equivalent circuits used to interpret the data. The layer model and equivalent circuit shown in Fig. A.3c are evidently an oversimplification of the complicated microstructure. Sideways conducting between the grains and a wide distribution of grain sizes and boundary thicknesses are inevitable in real materials, although not treated in the layer model. Moreover, the dielectric constant ε and dielectric conductivity σ (or dielectric resistivity ρ) are strongly frequency-dependent, due to the relaxation of the polarization process[137,138,144,145]. Consequently, the observed dispersion of complex impedance is generally not a semicircle and cannot be interpreted by a simple equivalent circuit. In fact, the appropriateness of the simple network for representing the materials response has been questioned by a number of investigators[142,143]. More extensive correlation of microstructure with impedance measurement as well as theoretical modelling is definitely necessary. Nevertheless, owing to the special structure of MnZn-ferrite, viz., a composite of sections of conductive bulk material separated by layers of insulating grain boundary phase, the interpretation of the dispersion of complex impedance is still possible by extrapolating the plot toward either high

or low frequency ranges. The intercepts at the resistance axis physically represent the material characteristics, namely, the grain boundary and bulk resistance.

A.3. Apparatus

Complex impedance was measured using a 2-probe technique[139,143]. A block diagram of the set up is shown in Fig. A5a (courtesy of Buechele). A sine wave, generated by an HP-3312A Function Generator was applied to the specimen ($\tilde{Z_u}$) and standard resistors ($\tilde{Z_s}$) connected in a series. The ratio of the two voltage impressed on input A and B, in decibels, and the phase angle between them, in degrees, were measured using an HP-3575A gain-phase meter. The voltage drop through the specimen and standard are proportional to the corresponding impedance, such that the complex impedance of the specimen is given by

$$\tilde{Z}_u = \tilde{Z}_s \left[\frac{\tilde{V}_A}{\tilde{V}_B} - 1 \right] \qquad \text{(A3.1a)}$$

and

$$\frac{\tilde{V}_B}{\tilde{V}_A} = 10^{\frac{B/A}{20}} e^{j\theta} \qquad \text{(A3.1b)}$$

where B/A is the decible output and θ the phase angle output of the gain-phase meter.

For magnetic measurements, the impedance of the coil winding on a toroidal specimen was measured. To facilitate the measurement, an insulating jig was made in the shape of a rectangular bar with conducting copper plates mounted at the two ends was made. The wires of the coil were connected to the two copper plates and the jig was sandwiched in between the two electrodes

for impedance measurement (Fig. A5b). For electrical measurements, the impedance of the specimen in the shape of a rectangular bar was directly measured. The contacting surfaces of the specimen were coated with silver paste. The specimen was then sandwiched between the electrodes. The electrodes were made of gold and spring-loaded to ensure good electrical contact. Electrical connections were made as short as possible and coaxial lines were used throughout to minimize the effect of stray capacity on the measurements at high frequency.

The standard box, which contains metal film resistors ranging from 10Ω to 1 MΩ, was used to facilitate the choice of standard resistances. The actual impedance value of the standards was calibrated at 1 MHz operating frequency using an HP-4271B LCR meter and the results are listed in Table A1. The performance of the apparatus has been tested by Buechele[139], who concluded that, in general, extrapolation from high frequency data could be made with confidence.

A.4. Data Analysis and Typical Results

Analysis of data for magnetic and electrical measurements was carried out with the aid of an HP-85 personal computer. The apparent impedance (admittance) was calculated from the gain-phase meter readouts, using equation A.3.1a. The standard impedance ($\tilde{Z}_s$) was obtained from the calibrated resistance and capacitance/inductance (Table A.1), using the following equations (Fig. A6a):

$$\tilde{Z}_s = R_s + jx_x$$

$$R_s = [r_s(1 - \omega c_p x_s) + \omega c_p r_s x_s]/[(1 - \omega c_p x_s)^2 + \omega^2 c_p{}^2 r_s{}^2] \quad (A4.1)$$

$$X_s = [x_s(1 - \omega c_p x_s) - \omega c_p r_s{}^2]/[1 - \omega c_p x_s)^2 + \omega^2 c_p{}^2 r_s{}^2]$$

where

$$r_s = r_o/[(1 - \omega^2 \ell_o c_o)^2 + \omega^2 c_o{}^2 r_o{}^2]$$

$$x_s = [\omega \ell_o(1 - \omega^2 \ell_o c_o) - \omega c_o r_o{}^2]/[(1 - \omega^2 \ell_o c_o)^2 + \omega^2 c_o{}^2 r_o{}^2]$$

and r_o, C_o, ℓ_o are resistance, capacitance and inductance of the standards, respectively,

and C_p = 30pf is the input capacitance, and input resistance is assumed to be infinite.

The magnetic permeability μ', energy dissipation μ'' and loss factor tan δ were calculated from the impedance of the coil wound on the toroidal specimen using Eqs. A1.4. The apparent electrical resistivity ρ_p and dielectric constant, ε_p, were calculated from the impedance of the bar specimen using the formula (Fig. A6b);

$$\rho_p = \frac{A}{L}\frac{1}{G_x} = \frac{A}{L}\frac{(R_x{}^2 + X_x{}^2)}{R_x}$$

$$\varepsilon_p = \frac{H_x}{\omega}\frac{L}{A} = -\frac{L}{A}\frac{X_x}{\omega(R_x{}^2 + X_x{}^2)} \quad (A4.2)$$

where A, L are the cross-section and length of the bar specimen and Gx, Hx, Rx, and Xx are the apparent conductance, susceptance, resistance and reactance respectively (Fig. A6b).

The dispersions of magnetic and electrical properties of two typical materials, labelled A for low loss and B for high permeability MnZn-ferrites, are shown in Figs. A7 and A8a. The significance of these plots was discussed in detail in Chapter 2B. The permeability decreases and the magnetic loss increases because of magnetic resonance, whereas the overall resistivity decreases because of the grain boundary capacitance effect. The complex impedance dispersions (R - X) of the two materials are shown in Fig. A8b. The characteristic parameters are listed. The inserts show that the complex admittance dispersion (G - B) is not suitable for analyzing the characteristic parameters in these materials.

ACKNOWLEDGEMENTS

It is a pleasure to express my appreciation to Professor G. Thomas for his encouragement and support throughout the course of this investigation. I am also grateful to Professor D. W. Hess for reading and commenting on this thesis and especially to Professor de Jonghe for helpful discussions and for the use of his equipment to make complex-impedance measurements.

The great measure to which my friends and colleagues have contributed to the completion of this work is also gratefully acknowledged. In particular, I would like to thank Dr. R. K. Mishra for his guidance and active interest in this research. My thanks are also extended to L. Rabenberg and R'Sue Caron for editorial assistance.

Special thanks are due to TDK Electronics Co. of Japan for supplying the MnZn ferrite samples and Professor H. Fujita for arranging the hot stage HVEM experiments. Drs. H. Mori and M. Komatsu performed the in-situ HVEM experiments on the 2MeV microscope at Osaka University. Appreciation is also extended to K. Gaugler for his assistance in AES analysis.

Finally, I am greatly indebted to my family, especially to my wife, Hsiu-Fung, for their love and understanding which made this work possible.

This research was financially supported by the Institute of Nuclear Energy Research (R.O.C.). Technical staff and facilities were provided by the Director, Office of Energy Research, Office of Basic Energy Sciences, Division of Materials Science of the U. S. Department of Energy under Contract No. DE-AC03-76SF00098.

VI. REFERENCES

1. P. I. Slick, "Ferrites for Non-Microwave Application" in Ferromagnetic Materials; vol. 2, ed. E. P. Wohlfarth, North-Holland, New York (1980).
2. D. J. Craik, Magnetic Oxide, John Wiley and Sons, New York (1975).
3. E. C. Snelling, Soft Ferrites, Properties and Applications, Iliffe, London (1969).
4. L. L. Hench and D. B. Dove, Ch. VIII, "Magnetic Ceramics" in Physics of Electronic Ceramics, Marcel Dekker, Inc., New York (1972).
5. B. D. Cullity, "Soft Magnetic Materials", Ch. 13 in Introduction to Magnetic Materials, Addison-Wesley Publishing co., London (1972).
6. J. Smit and H. P. J. Wijn, Ferrites, John Wuley and Sonc, Inc. New York (1959).
7. J. Smit, Magnetic Properties of Materials, McGraw-Hill, New York (1971).
8. K. J. Standley, Oxide Magnetic Materials, Clarendon Press, Oxford (1962).
9. R. S. Tebble, D. J.Craik, Magnetic Materials, Wiley-Interscience, New York (1969).
10. W. D. Kingery, H. K. Bowen and D. R. Uhlmann, "Magnetic Properties", Ch. 19 in Introduction to Ceramics, John Wiley and Sons, New York (1976).
11. E. Ross, "Magnetic Properties and Microstructure of High-Permeability MnZn Ferrites", in Ferrites; Proc. International Conference, Japan (1970), pp.203-209.

12. Y. Hoshino, S. Iida and M. Sugimoto, "Preparation of Ferrite Materials", ibid, pp. 69-137 and 179-236.

13. A. Broess van Groenou and J. G. M. deLau, "Effect of Microstructure on the Properties of Ferrites" in Conference on Electrical Magnetic and Optical Ceramics, London, British Ceramic Society (1972).

14. T. Inui and N. Ogasawara, "Grain Size Effect in Microwave Ferrite Magnetic Properties", IEEE Trans. Mag. Mag-13, p. 1729-1744 (1977).

15. M. I. Alam, N. R. Nair and T. V. Ramamuriti, "Effect of Raw Material and Process Conditions on Properties of MnZn-Ferrous Ferrites", IEEE Trans. Mag. Mag-18, pp. 950-952 (1982).

16. B. B. Ghate, "Processing and Magnetic Properties of Low-Loss and High-Stability MnZn-Ferrites", in Materials Science Research, Vol. 11: Processing of Crystalline Ceramics, eds. H. Palmour III, R. F. Davis and T. M. Hare, Plenum Press, New York (1978).

17. S. Krupicka, "Soft-Ferrites, Achievements and Problems", J. Mag. Mag. Materials 19, 86-88 (1980).

18. H. Tsuenekawa, A. Nakata, T. Kamijo, K. Okutani, R. K. Mishra and G. Thomas, "Microstructure and Properties of Commercial Grade Manganese Zinc Ferrites", IEEE Trans. on Mag. Mag-15, pp. 1855-1857 (1979)..

19. M. Yan and D. W. Johnson, Jr., "Impurity-Induced Exaggerated Grain Growth in MnZn Ferrites", J. Amer. Ceram. Soc. 61, 342-349 (1978).

20. A. Beer and J. Schwarz, "New Results on the Influence of Sintering Conditions on the Magnetic Properties of Mn-Zn Ferrites", IEEE Trans. Mag. 2, 470-472 (1966).

21. N. Yoneda, S. Ito and I. Katah, "Effect of Binder Materials (PVA) and Starch on the Formation of Duplex Microstructure in Sintered $Mn_{.5}Zn_{.5}Fe_2O_4$", Ceram. Bull. 59, 549 (1980).

22. T. Inui and N. Ogasawara, "Grain Size Effects on Microwave Ferrite Magnetic Properties", J. Appl. Phys. 49, 2019-2024 (1978).

23. H. Watanabe and S. Takeda, "Growth and Properties of Mn-Zn-Sn Ferrite Single Crystals", J. de Physique colloque. C1, 51-55 (1977).

24. S. Gasiorek and M. Szynkarczuk, "Magnetic Materials Obtained by the Compacting of Reactive MnZn Ferrites Powders", J. Mag. Mag. Mater. 19, 105-106 (1980).

25. S. Gasiorek and A. Miracka, "Preparation of (Reactive) MnZn Ferrite Powders by the Wet Method", J. Mag. Mag. Mater. 19, 97-98 (1980).

26. Z. Krysicki and T. Lubanska, "Effect of the Presintered Process on the Microstructure and Initial Permeability of Mn-Zn Ferrite", J. Mag. Mag. Mater. 19, 107-108 (1980).

27. T. S. Plaskett, S. A. Shivashankar, B. L. Gilbert, B. L. Okon, C. L. Chien and D. A. Herman, Jr., "Synthesis of MnZnFerrite from Na_2O-Ba_2O_3 Flux under CO-CO_2 Ambients", J. Appl. Phys. 53, 2428-2430 (1982).

28. E. Takama and M. Ito, "New MnZn Ferrite Fabricated by Hot Isostatic Pressing", IEEE Trans. Mag. Mag-15, 1858-1860 (1979).

29. U. Wagner, "Spray Firing for Preparation of Presintered Powder for Soft Ferrites", J. Mag. Mag. Mater. 19, 99-104 (1980).

30. R. J. Willey, "Effects of Post Sinter-Cooling Cycle on MnZn-Ferrites", J. Mag. Mag. Mater. 19, 126-129 (1980).

31. M. I. Alan et al., "Multilayer Sintering of MnZn Ferrites in Controlled Atmosphere", J. de Physique Colloque C1, Supplement au no. 4, Tome 38, Avril, C1-303-309 (1977).

32. M. F. Yan and D. W. Johnson, Jr., "Sintering of High Density ferrites", in Materials Science Research, Vol. 11: Processing of Ceramic Crystalline, eds. H. Palmour, III et al. Plenum Press, New York (1978).

33. A. Morell and A. Hermosin, "Fast Sintering of Soft Mn-Zn and Ni-Zn Ferrite Pot Cores", Ceram. Bull. 59, 626-629 (1980).

34. S. Murakami and T. Shinokaro, "High B Polycrystalline Mn-Zn Ferrite", Ferrites: Proc. ICF 3, Japan (1980), pp. 321-323.

35. S. Natansohn and D. H. Baird, "Effect of Synthesis Parameters on the Magnetic Properties of MnZn-Ferrite", J. Amer. Ceram. Soc. 52, 127-132 (1969).

36. J. Tasaki, "Effect of Sintering Atmosphere on the Permeability of Sintered Ferrites", in Ferrite, Proc. Inter. Conf., Japan (1970), pp. 84-86.

37. A. Withop, "Manganese Zinc Ferrite Processing, Properties and Recording Performance", IEEE Trans. Mag. Mag-14, 439-441 (1978).

38. T. Yamaguchi, "Effect of Powder Parameters on Grain Growth in MnZn-Ferrite", J. Amer. Ceram. Soc. 47, 131-133 (1964).

39. P. F. Bongers, F. J. A. den Broeder, J. P. M. Damen, P. E. C. Franken and W. J. Stacy, "Defects, Grain Boundary Segregation and Secondary Phases of Ferrites in Relation to Magnetic Properties", in Ferrites; Proc. ICF3, Japan, eds. H. Watanabe, S. Iida and M. Sugimoto (1980).

40. R. C. Sundall, Jr., B. B. Ghate, R. J. Holmes and C. E. Pass, "The Grain Boundary Chemistry and Magnetic Properties of $Mn_{0.5}Zn_{0.4}Fe_{0.08}O_4$", in Adv. in Ceram. Vol. 1: Grain Boundary Phenomena in Electronic Ceramics, ed. L. M. Levinson, Amer. Ceram. Soc. Inc., Columbus, Ohio (1981), pp. 502-511.

41. B. B. Ghate, "Boundary Phenomena in Soft Ferrites--A Review", ibid, Ref. 40, pp. 477-493.

42. J. D. Livingston, "Effect of Grain Boundaries on Physical Properties", in Grain Boundaries in Engineering Materials, eds. J. L. Walter, J. H. Westbrook, D. A. Woodford, Claitor's Publishing Division, Baton Rouge, LA (1975), pp. 165-180.

43. T. Akashi, Trans. Japan Inst. Metals 2, 171 (1961).

44. T. Akashi, "Precipitation in Grain Boundaries of Ferrites and their Electrical Resistivities", Part I. NEC Research and Development 8, 89-106 (1966); Part II, ibid, 66-82 (1970).

45. M. Paulus, "Properties of grain Boundaries in Spinel Ferrites", in Materials Science Research, Vol. 3: the Role of Grain Boundaries and Surfaces, eds. W. W. Kriegel and H. Palmour III. Plenum Press, New York (1966).

46. P. E. C. Franken, H. Van Dovoren and J. A. T. Verhoeven, "The Grain Boundary Composition of Mn-Zn Ferrites with CaO, SiO_2, and TiO_2 Addition", Ceramurgia Inter. 3, 122-123 (1977).

47. P. E.C. Franken, "The Influence of the Grain Boundary on the Temperature Coefficient of Ti-substituted Ferrites", IEEE Trans. Mag. Mag-14 [5], 898-899 (1978).

48. W. C. Johnson, "Grain Boundary Segregation in Ceramics", Met. Trans. 8A, 1413-1422 (1977).

49. P. J. Jorgensen, "Grain Boundary Phenomena in Ceramic Materials", ibid., Ref. 42, pp. 205-222.

50. W. D. Kingery, "Grain Boundary Phenomena in Electronic Ceramics", ibid., Ref. 40, pp. 1-23.

51. R. C. Bradt and R. E. Tressler, Deformation of Ceramic Materials, Plenum, New York (1975).

52. V. Cirilli and A. Burdese, "The Calcium Oxide-Wurtzite System", in International Symposium on the Reactivity of Solids, Part II (1952), pp. 867-79.

53. A. Burdese and C. Brisi, Ricerca Sci. 22, 1566 (1952).

54. L. E. Davis et al. Handbook of Auger Electron Spectroscopy, 2nd ed., Physical Electronics Industries, Inc. (1972).

55. P. M. Hall and J. M. Morabito, "Compositional Depth Profiling by Auger Electron Spectroscopy", CRC Critical Review in Solid State and Materials Science 53 (1978).

56. D. L.Wilcox, et al., "Electron Beam Effects in Depth Profiling Measurements with Auger Electron Spectroscopy", J. Appl. Phys. 46, 4581-4583 (1975).

57. P. W. Palmberg, "Use of Auger Electron Spectroscopy and Inert Gas Sputtering for Obtaining Chemical Profile", J. Vac. Sci. Tech. 9, 160-163 (1972).

58. P. W. Palmberg, "Quantitative Auger Electron Spectroscopy Using Elemental Sensitivity Factors", J. Vac. Sci. Tech. 13, 214-248 (1976).

59. J. M. Morabito, "First Order Approximation to Auger Analysis", Surf. Sci. 49, 318-324 (1975).

60. C. C. Chang, "General Formalism for Quantitative Auger Analysis", Surf. Sci. 48, 9-21 (1975).

61. P. E. C. Franken, "Secondary Phases and Segregation Layers at Grain Boundaries in Electronic Ceramics Materials", ibid., Ref. 40 (1981), pp. 39-52.

62. P. E. C. Franken and H. van Doveren, "Determination of the Grain Boundary Composition of Soft Ferrites by Auger Electron Spectroscopy", Ber. Dt. Keram. Ges. 55, 287-289 (1978).

63. P. E. C. Franken and W. T. Stacy, "Examination of Grain Boundaries of MnZn Ferrites by AES and TEM", J. Amer. Ceram. Soc. 63, 315-319 (1980).

64. G. Thomas, R. Gronsky, O. L. Krivanek and R. K. Mishra, "Physical and Chemical Characterization of Interfaces by Electron Optical Methods", in Materials Science Research, vol. 14: Surfaces and Interfaces in Ceramics and Ceramic-Metal System, eds. J. Pask and A. Evans, Plenum Press, New York (1980), pp. 35-49.

65. R. K. Mishra and G. Thomas, "Electron Microscopy of Ferrites", J. Amer. Ceram. Soc. 62 294 (1979).

66. R. K. Mishra and G. Thomas, "Recent Progress in Electron Microscopy of Ferrites", ibid, Ref. 39, pp. 257-264.

67. O. L. Krivanek, T. M. Shaw and G. Thomas, " Imaging of Thin Intergranular Phases by High-Resolution Electron Microscopy", J. Appl. Phys. 50, 4223 (1979).

68. E. K. W. Goo, R. K. Mishra and G. Thomas, "Transmission Electron Microscopy of $Pb(Zr_{0.52}Ti_{0.48})O_3$", J. Amer. Ceram. Soc. 64, 517 (1981).

69. R. Raj, "Morphology and Stability of the Glass Phase in Glass-Ceramic Systems", J. Amer. Ceram. Soc. 64, 245 (1981).

70. W. D. Kingery, "Plausible Concepts Necessary and sufficient for Interpregation of Ceramic Grain Boundary Phenomena", Part I. J. Amer. Ceram. Soc. 57, 1-8; Part II, ibid., 57, 74-83 (1974).

71. I. Tsutomu, "A Study on Grain Growth in Mn-Zn Ferrite", ibid, Ref. 39, pp. 128-130.

72. D. Kolar and S. Pejovnik, "Migrating Grain Boundaries and Sintering in Multicomponent Systems", ibid., Ref. 39, pp. 445-452.

73. M. L. Huckabee, T. M. Hare and H. Palmour, III, "Rate Controlled Sintering as a Processing Method", ibid., Ref. 32, pp. 205-215.

74. F. M. A. Carpay, "The Effect of Pore Drag on Ceramic Microstructure", in Ceramic Microstructure '76, eds. R. M. Fulrath and J. A. Pask, Westview Press, Inc., Boulder, Colorado (1977), pp. 261-275.

75. P. J. Grundy and R. S. Tebble, "Lorentz Electron Microscopy", Advances in Physics 17, 153-242 (1968).

76. D. Wohlleben, "Diffraction Effects in Electron Microscopy", J. Appl. Physics 38, 3341 (1967).

77. M. S. Cohen, "Wave-Optical Aspects of Lorentz Microscopy", J. Appl. Physics 38, 4966 (1967).

78. G. Thomas and M. T. Goringe, Ch. 3 in Transmission Electron Microscopy of Materials, John Wiley and Sons, Inc. New York (1979).

79. P. B. Hirsch, A. Howie, R. B. Nicholson, D. W. Pashky and M. J. Whelan, in Electron Microscopy of Thin Crystal, Ch. 16, Butterworths, London (1971).

80. J. W. Edington, in Practical Electron Microscopy in Materials Science, Sec. 3.23, MacMillan Philips Technical Library (1975).

81. J. W. Steeds, "Convergent Beam Electron Diffraction", in Introduction to Analytical Electron Microscopy, Ch. 15, eds. J. J. Hren, J. I. Goldstein and D. V. Joy, Plenum Press, New York (1979).

82. R. C. Ecob, M. P. Shaw, et al., "The Application of Convergent-Beam Electron Diffraction to the Detection of Small Symmetry Changes Accompanying Phase Transformation. I. General and Methods, Phil. Mag. A 44, 1117-1133 (1981).

83. P. Goodmann, "Setting Up Convergent Beam Diffraction for Materials Analysis Using a TEM", Scanning Electron Microscopy I (1980).

84. P. Goodmann, "A Practical Method for 3-dim. Space Group Analysis Using Convergent Beam Electron Diffraction", Acta Cryst. A31, 804 (1975).

85. J. W. Steeds and N. S. Evans, "Practical Example of Point and Space Group Determination in CBD", in Proceedings of EMSA (38th) Meeting, Claitors Publishing House, New Orleans (1981).

86. S. Chikazumi, Physics of Magnetism, John Wiley and Sons, New York (1964).

87. J. L. Snoek, "Dispersion and Absorption in Magnetic Ferrites at frequencies Above One Megacycle", Physica 14, 207 (1948).

88. W. D. Kingery, H. K. Bowen and D. R. Uhlmann, in Introduction to Ceramics, Ch. 17, John Wiley and Sons, Inc. (1976).

89. C. G. Koops, "On the Dispersion of Resistivity and Dielectric Constant of Some Semiconductors at Audio Frequencies", Phys. Rev. 83, 121 (1951).

90. M. S. Cohen, "Ferromagnetic Properties of Films", in Handbook of Thin Film Technology, Ch. 17, eds. L. I. Maissel and R. Glange, McGraw-Hill Co. (1970).

91. C. Kittel, "Physical Theory of Ferromagnetic Domains", Rev. Modern Phys. 21, 541 (1949).

92. R. K. Mishra, "Defects, Phase Transformations and Magnetic Properties of Lithium Ferrites", IEEE Trans. Mag. Mag-15, 1855 (1979).

93. O. Van der Biest and G. Thomas, "Cation Stacking Faults in Li-Ferrites Spinel", phys. stat. sol. (a) 24, 65 (1974).

94. J. P. Jakubovics, A. J. Lapworth and T. W. Jolly, "Electron Microscope Studies of Ferromagnetic Ordered Structure", J. Appl. Phys. 49, 2002 (1978).

95. N. F. Mott and W. D. Twose, "The Theory of Impurity Conduction", Adv. in Physics 10, 107 (1961).

96. D. G. Austin and N. F. Mott, "Polarons in Crystalline and Non-Crystalline Materials", Adv. in Physics 18, 42-102 (1969).

97. A. J. Bosman and H. J. Van Daal, "Small-polaron versus band Conduction in Some Transition-Metal Oxides", Adv. in Physics 19, 1-117 (1970).

98. M. I. Klinger and A. A. Samokhvalov, "Electron Conduction in Magnetite and Ferrites", phys. stat. sol. (b) 79, 9-48 (1977).

99. J. M. Blank, "Equilibrium Atmosphere Schedules for the Cooling of Ferrites", J. Appl. Phys. Suppl. 32, 378S-379S (1961).

100. E. D. Macklen, "Thermogravimetric Investigation of Fe^{2+} in Ferrites Containing Excess Iron", J. Appl. Phys. 36, part II, 1022-1024 (1965).

101. P. I. Slick, "A Thermogravimetric Study of the Equilibrium Relations between a MnZn-ferrite and an O_2-N_2 Atmosphere", in Ferrites: Proceedings of the International Conference, Japan (1970), pp. 81-83.

102. R. Morineau and M. Paulus, "Oxygen Partial Pressures of Mn-Zn Ferrites", phys. stat. sol. (a) 20, 373-380 (1973).

103. R. Morineau and M. Paulus, "Chart of PO_2 versus Temperature and Oxidation Degree for Mn-Zn Ferrites", IEEE Trans. Mag. Mag-11, 1312-1314 (1975).

104. R. Morineau, "Structural Defects and Oxidation-Reduction Equilibrium in Mn, Zn Ferrites", phys. stat. sol. (a) 559 (1976).

105. G. W. van Oosterhout and J. Visser, "Determination of Active Oxygen and Iron (II) in Oxide Compound" Anal. Chim. Acta 33, 330-332 (1965).

106. P. S. Farrington, W. P. Schaefer and J. M. Duhnam, "Coulometric Titration of Iron (II) with Chlorine", Anal. Chem. 33, 1318-1320 (1961).

107. P. K. Gallagher, "A Coulometric Analysis of Iron (II) in Ferrites Using Chlorine", Ceram. Bull. 57 576-578 (1978).

108. H. J. Van Hook, "Phase Equilibria in Magnetic Oxide Materials", in Phase Diagrams. Vol. IV, Materials Science and Technology, Ch. 4, Academic Press, Inc., New York (1976).

109. D. Stoppels, "Relationship between Magnetic Crystalline Anisotropy and Initial Magnetic Permeability for Monocrystalline MnZn-Ferrite:, J. Appl. Phys. 51, 2789 (1980).

110. D. Stoppels and P. G. T. Boonen, "The Influence of the Second-Order

Magnetocrytalline Anisotropy on the Initial Magnetic Permeability of MnZn Ferrous Ferrite", J. Mag. Mag. Mater. 19, 409 (1980).

111. A. Seeger, H. Kronmüller, H. Rieger and H. Träuble, "Effect of Lattice Defects on the Magnetization Curve of Ferromagnets", J. Appl. Phys. 35, 740 (1964).

112. J. E. Knowles, "Permeability Mechanism in Mn-Zn Ferrites", J. de Physique, Colloque C-1, supplement au no. 4, Tome 38, C1-28 (1977).

113. G. C. Jain et al., "On the Origin of Core Losses in a Manganese Zinc Ferrite with Appreciable Silia Content", J. Appl. Phys. 49, 2894 (1978).

114. B. Hoekstra, "Initial Permeability and Intrinsic Magnetic Properties of Polycrystalline MnZn-Ferrite", J. Appl. Phys. 49, 4902 (1978).

115. G. C. Jain et al. "Effect of Intragranular Porosity on Initial Permeability and Coercive Force in a MnZn-Ferrite", J. Mater. Sci. 11, 1135 (1976).

116. A. D. Giles and F. F. Westerndrop, "Some Loss Relationships in Mn-Zn Ferro Ferrites and their Response to Magnetic Disturbance", IEEE Trans. Mag. Mag-18, 944 (1982).

117. M. Dixon, T. S. Stakelon and R. C. Sundahl, "Complex Permeability Variation of Iron Excess CoNiZn Ferrites with Annealing Temperature", IEEE Trans. Mag. Mag-13, 1351 (1977).

118. T. Iimura, "Effect of Fe^{2+} Ion on the Initial Permeability of MnO-ZnO-MgO-Fe_2O_3 Ferrites", J. Amer. Ceram. Soc. 59, 458-459 (1976).

119. P. K. Gallagher, E. M. Gyorgy and D. W. Johnson, Jr., "Relation Between Magnetic Permeability and Stoichiometry of $Mn_{0.510}Z_{0.417}Fe_{2.073}O_{4+}$ ", Ceram. Bull. 57, 812-813 (1979).

120. T. Tanaka, "Effects of the Oxygen Nonstoichiometry on the Domain Structure and the Initial Permeability in MnZn-ferrite", Japan J. Appl. Phys. 17, 349-354 (1978).

121. A. Morita and A. Okamoto, "Effect of Oxygen Content on the Properties of Low Loss MnZn Ferrites", in Ferrites: Proceedings ICF, Japan 1980, pp. 313-316.

122. W. D. Kingery, "Grain Boundary Phenomena in Electronic Ceramics", in Advances in Ceramics, Vol. I., Amer. Ceram. Soc., Columbus, Ohio (1981), pp. 1-23.

123. M. F. Yan and D. W. Johnson, Jr., "Impurity-induced Exaggerated Grain Growth in MnZn-ferrites", J. Amer. Ceram. Soc. 61, 342-349 (1978).

124. M. F. Yan, R. M. Cannon and H. K. Bowen, "Grain Boundary Migration in Ceramics", in Ceramic Microstructures '76, eds. R. M. Fulrath and J. A. Pask, Westview Press, Boulder, Colorado, p. 276.

125. W. D. Kingery, "Plausible Concepts Necessary and Sufficient for Interpretation of Ceramic Grain-Boundary Phenomena, I. Grain Boundary Characteristics, Structure and Electrical Potential", J. Amer. Ceram. Soc. 57, 1-8 (1974).

126. T. Tanaka, "Lattice Constant and Nonstoichoimetry in Mn-Zn Ferrites", Japan J. Appl. Phys. 13, 1235 (1974).

127. M. Dixon and C. E. Pass, "Influence of Processing on Very High Permeability MnZn-Ferrites", Ceram. Bull. 57, 735 (1978).

128. T. Tanaka, "Effects of the Oxygen Nonstoichiometry on the Domain Structure and the Initial Permeability in MnZn Ferrites", Japan J. Appl. Phys. 17, 349 (1978).

129. N. J. Hellicar and A. Sicignamo, "Dynamic Role of ZnO in the Sintering of MnZn Ferrites", Ceram. Bull. 61, 502 (1982).

130. T. Yamaguchi, "Effect of Powder Parameters on Grain Growth in MnZn Ferrites", J. Amer. Ceram. Soc. 47, 131 (1964).

131. E. M. Voget et al., "Disaccommodation of MnZn Ferrite after Temperature Cycling", J. Amer. Ceram. Soc. 64, 624 (1981).

132. H. P. Peloschek and D. J. Perduijn, "High Permeability MnZn-Ferrite with Flat μ-T Curve", IEEE Trans. Mag. Mag-4, 453 (1968).

133. J. Tasaki and T. Izushi, "Behavior of Additives in Ferrites", J. de Physique, Colloque C1, Supplement 4, C1-175 (1977).

134. J. W. Harvey and D. W. Johnson, Jr., "Binder Systems in Ferrites", Ceram. Bull. 59, 637 (1980).

135. N. Yoneda, S. Ito and I. Katoh, "Effect of Binder Materials (PVA) and Starch on the Formation of Duplex Structure in Sintered $Mn_{0.5}Zn_{0.5}Fe_2O_4$", Ceram. Bull. 59, 549 (1980).

136. A. D. Giles, F. F. Westendorp, "Simultaneous Substitution of Co and Ti in Linear MnZn Ferrites", J. de Physique, Colloque C1, Supplement 4, C1-47 (1977).

137. A. Von Hippel, Dielectric Materials and Application, John Wiley and Sons, Inc., New York (1976).

138. W. D. Kingery et al., "Dielectric Properties", in Introduction to Ceramics, Ch. 18, John Wiley and Sons, Inc., New York (1976).

139. A. C. Buechele, "Effect Produced by the Introduction of Calcium into Sodium Beta-Alumining Solid Electrolyte", M.S. Thesis, Cornell University (1978).

140. J. E. Bauerle, "Study of Solid Electrolyte Polarization by a Complex Admittance Method", J. Phys. Chem. Solids 30, 2657 (1969).

141. S. H. Chu and M. A. Seitz, "The AC Electrical Behavior of Polycrystalline ZrO_2-CaO", J. Solid State Chem. 23, 297 (1978).

142. T. G. Stratton, D. Reed and H. L. Tuller, "Study of Boundary Effects in Stabilized Zirconia Electrolytes", ibid, Ref. 40, p. 114.

143. L. C. DeJonghe, "Grain Boundaries and Ionic Conduction in Sodium Beta Alumina", J. Mat. Sci. 14, 33 (1979).

144. K. S. Cole and R. H. Cole, "Dispersion and Absorption in Dielectrics", J. Chem. Phys. 9, 341 (1941).

145. K. L. Ngai and C. T. White, "Frequency Dependence of Dielectric Loss in Condensed Matter", Phys. Rev. B 20, 2475 (1979).

Figure Captions

Fig.II.1. (a) The eutectic liquid (dark background) coexists with a solid intermediate phase (white particles, P), (b) A secondary phase, s, is nucleated from the supersaturated liquid at the solid-liquid interface. (c) remelting of the secondary phase by electron beam heating.

Fig..II.2 Room temperature microstructure of the same specimen as in Fig. II.1. (a) Thin CaO coating region; the Ca rich precipitates (P) are distributed in the Ca deficient matrix. (b) Thick CaO coating region; round Ca deficient precipitates (q) are distributed in the Ca rich matrix.

Fig.II.3. Ca-map and corresponding fracture micrograph of in-situ fractured MnZn-ferrite. (a) Auger electron spectrum of a transgranular fractured surface (A). (b) Auger electron spectrum of intergranular fractured surface (B).

Fig.II.4. Bright field (B.F.) and diffuse scattering dark field (DF) images of MnZn-ferrite showing an amorphous phase at the grain boundary.

Fig.II.5. Auger electron spectrum of a freshly fractured MnZn-ferrite surface (AES); Ca map of high temperature fractured specimen and the corresponding fracture micrograph corresponding to the Ca-map.

Fig.II.6. HVEM images of the specimen heated to 1300°C and 1400°C, respectively. (i) the grain boundary images become diffuse at higher temperature, (ii) grain boundary migration occurs at 3-grain junctions a,b,c. (iii) preferential sublimation occurs at grain junction d.

Fig.II.7. Microstructure of (a) type A and (b) type B MnZn-ferrite. The grain size of type A material is smaller and the grain boundaries can be etched readily. The internal pores are observed in type B material only.

Fig.II.8. Frequency dispersion of (a) initial permeability (μ'), (b) magnetic loss (μ'') and (c) loss tangent ($\tan \delta$) for both low loss (Type A and high μ_i (Type B) MnZn-ferrite.

Fig.II.9. (a)Frequency dispersion of resistivity and (b)complex impedance plots for type A and B MnZn-ferrite.

Fig.II.10. Interaction of magnetic domain wall motion with segregated grain boundaries in type A material. A pair of Lorentz images is shown in the accompanying sketch. Domains B and C grew when the applied field increased and domain A was not able to shrink (stages 1 and 2). Only at a higher applied field does the domain wall surrounding A jump to the grain boundary (dotted lines).

Fig.II.11. [001] zone axis CBED pattern of type A material with an electron probe placed (a) at the interior of a grain and (b) at a region near grain boundary. (a) shows 4-fold symmetry and (b) shows only 2-fold symmetry.

Fig.II.12. (a) Typical microstructure of a polycrystalline material; (b) a rectangular bar cut out from the material and (c) schematic of lumped circuits corresponding to each phase.

Fig.III.1. Principle of Lorentz Microscopy: (a) underfocused Lorentz image, (b) rays diagram shows electron excessive (E) and deficient (D) regions right beneath the domain walls and (c) overfocused Lorentz image of the same area as (a).

Fig.III.2. Interaction of the domain wall with pure grain boundaries (dotted line): Domain walls parallel to grain boundaries are stopped completely at grain boundary (1 - 1, 2 - 2 and 3 - 3), while the domain wall perpendicular to the grain boundary can move up and down.

Fig.III.3. Interaction of the domain wall with an inclined grain boundary (dotted line). The domain wall (1 - 1) is perpendicular to the foil, while the grain boundary is inclined to the foil surface, such that the domain wall can move across the grain boundary.

Fig.III.4. Interaction with a segregated grain boundary (dotted lines): The domain wall (1 - 1) is stopped at a distance from the grain boundary (stages 1 and 2) and jumps to the grain boundary as the applied field increases further (stage 3). It splits and nucleates a new closure domain E as the applied field decreases (stage 4). The grain boundary also acts as a nucleation site for domain C (stage 2).

Fig.III.5. Interaction of a pore: The domain wall (1 - 1) moves toward the left when the applied field is increased, and it moves toward the right when the applied field is decreased. The lower end of the domain wall is pinned by pore (P).

Fig.III.6. Interaction with a crack: Domain walls move toward the crack (C) continuously and are stopped by the crack.

Fig.III.7. Interaction with the second phases: The domain wall (1 - 1), moving to the right, is stopped by the precipitates (d, e and g). Nucleation of the domains with reverse magnetization occurs at precipitates (domain B nucleated at stage 2 and domain C nucleated at stage 3).

Fig.III.8. Interaction with the stacking faults: Domain walls are pinned to the faults (dotted lines). Nucleation of domain (a) occurred at stage 2.

Fig. IV.1. Oxidation/reduction of ferrous (Fe^{2+}) ions in type B MnZn-ferrite caused by controlled atmosphere annealing. The divalent iron content decreases as either the PO_2 level of annealing atmosphere increases or the annealing temperature decreases for same PO_2 level. Precipitation might occur when the PO_2 level exceeds the phase boundary limit.

Fig.IV.2. Dispersions (frequency dependence) of apparent electrical resistivity for annealed and unannealed MnZn-ferrite specimens. A higher resistivity is obtained for a specimen annealed in a higher PO_2 level. The resistivities drop off in the high operating frequency regime due to the grain boundary capacitance effect.

Fig. IV.3. Fe^{2+} dependence of apparent electrical resistivity of the same materials as in Fig. IV.2. The resistivities are higher for specimens containing smaller amounts of ferrous (Fe^{2+}) ions. The annealing atmospheres are indicated in Fig. IV.2.

Fig.IV.4. Fe^{2+} dependence of grain boundary and bulk resistances. They are comparable in magnitude and increase as the amount of divalent iron decreases. The change of grain boundary resistance is more pronounced as a result of annealing.

Fig.IV.5. Fe^{2+} dependence of grain boundary and bulk resistivity. The grain boundary resistivity is overwhelmingly higher than the bulk resistivity and it increases more rapidly.

Fig.IV.6. Dispersions of (a) magnetic permeability μ', (b) loss μ'', and (c) tan δ for annealed and unannealed MnZn-ferrite. The magnetic properties decrease as the annealing PO_2 level is increased.

Fig.IV.7. Fe^{2+} dependence of magnetic permeability (at 1KHz and 100KHz), maximum magnetic loss and tan δ (at 6MHz) of the same specimens as fig. IV.6. The magnetic properties decrease with the ferrous (Fe^{2+}) ions content.

Fig. A.1. Self-inductance (L_o) of the coil wound on the toroid.

Fig. A.2. Mathematical models of a dielectric material. It can be described in terms of a complex dielectric constant ($\overset{*}{\varepsilon}$) or complex conductivity ($\overset{*}{\sigma}$).

Fig. A.3. Modelling of polycrystalline materials (a) cubic grain microstructure, (b) top layer and equivalent circuits and (c) simplified layer model and equivalent circuits.

Fig. A.4. (a) Complex impedance and (b) complex admittance dispersions corresponding to the equivalent circuit of layer model in Fig. A.3c.

Fig. A.5. (a) Block diagram of apparatus for complex impedance measurement and (b) specimen jig for magnetic measurement, which is done through measuring the impedance of a coil wound on the magnetic specimen.

Fig. A.6. Formula for calculating (a) input impedance and (b) the apparent resistivity and dielectric constant.

Fig. A.7. Typical frequency dispersions of (a) permeability (b) magnetic loss and (c) tan δ.

Fig. A.8. (a) Typical frequency dispersions of apparent resistivity and (b) complex impedance/admittance dispersions.

TABLE I. CHEMICAL COMPOSITION OF REACTED

MnZn-FERRITE (cf. Fig.II.2)

		Ca	Mn	Fe	Zn
Region A	matrix	0.48	20.08	79.44	-
	ppt.	52.22	10.57	37.21	-
Region B	matrix	82.73	4.91	12.35	-
	ppt.	7.95	29.39	62.67	-

Note: these composition should be used to indicate relative amount only.

TABLE II. CHARACTERISTIC PARAMETERS OF MnZn-FERRITE

Materials	Type A	Type B
Bulk Resistance (Ω)	55.5	19.7
G.B. Resistance (Ω)	4,000.0	100.3
G.B. Capacitance(pf)	630.0	1,590.0
x	$1x10^{-3}$	$0.33x10^{-3}$
bulk resistivity(Ωm)	0.078	0.028
g.b. resistivity(Ωm)	16,560.0	420.0
dielectric const.(ε_0)	50.8	43.6

x=g.b.thickness/grain size; $\varepsilon_0=8.85x10^{-12}$farad/m

Specimen Dimensions: 2.67mmx5.5mmx10.53mm

Type A : low loss MnZn-ferrite

Type B : high μ_i MnZn-ferrite

Table A.1 Calibrated Standard Resistance

Nominal Resistance	1M	100K	10K	1K	100	50	21	10
Calib. $R_0(\Omega)$	0.85 M	103 K	9.87 K	0.998 K	99.5	50.3	21.1	10.2
C_0 (pf)	8.24	8.54	9.04	8.89	—	—	—	—
L_0 (μH)	—	—	—	—	0.22	0.268	0.283	0.284

XBL8211-6845

Table A.1 Calibrated Standard Resistance

Nominal Resistance	1M	100K	10K	1K	100	50	21	10
Calib. $R_0(\Omega)$	0.85 M	103 K	9.87 K	0.998 K	99.5	50.3	21.1	10.2
C_0 (pf)	8.24	8.54	9.04	8.89	—	—	—	—
$L_0(\mu H)$	—	—	—	—	0.22	0.268	0.283	0.284

XBL8211-6845

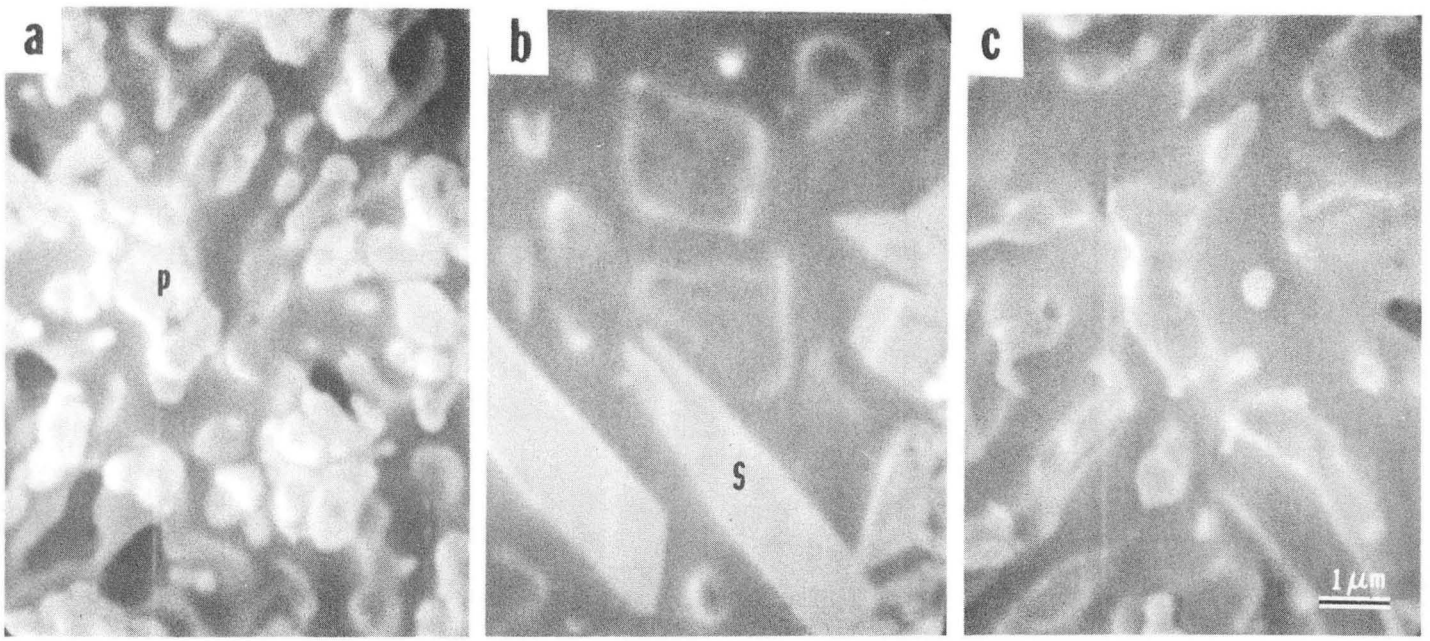

XBB 826-5214

Fig.II.1

Figure 1 a) The eutectic liquid (dark) coexists with solid intermediate phase (white particles). b) A secondary phase is nucleated from the super saturated liquid at the solid-liquid interface. c) remelting of the secondary phase by electron beam heating.

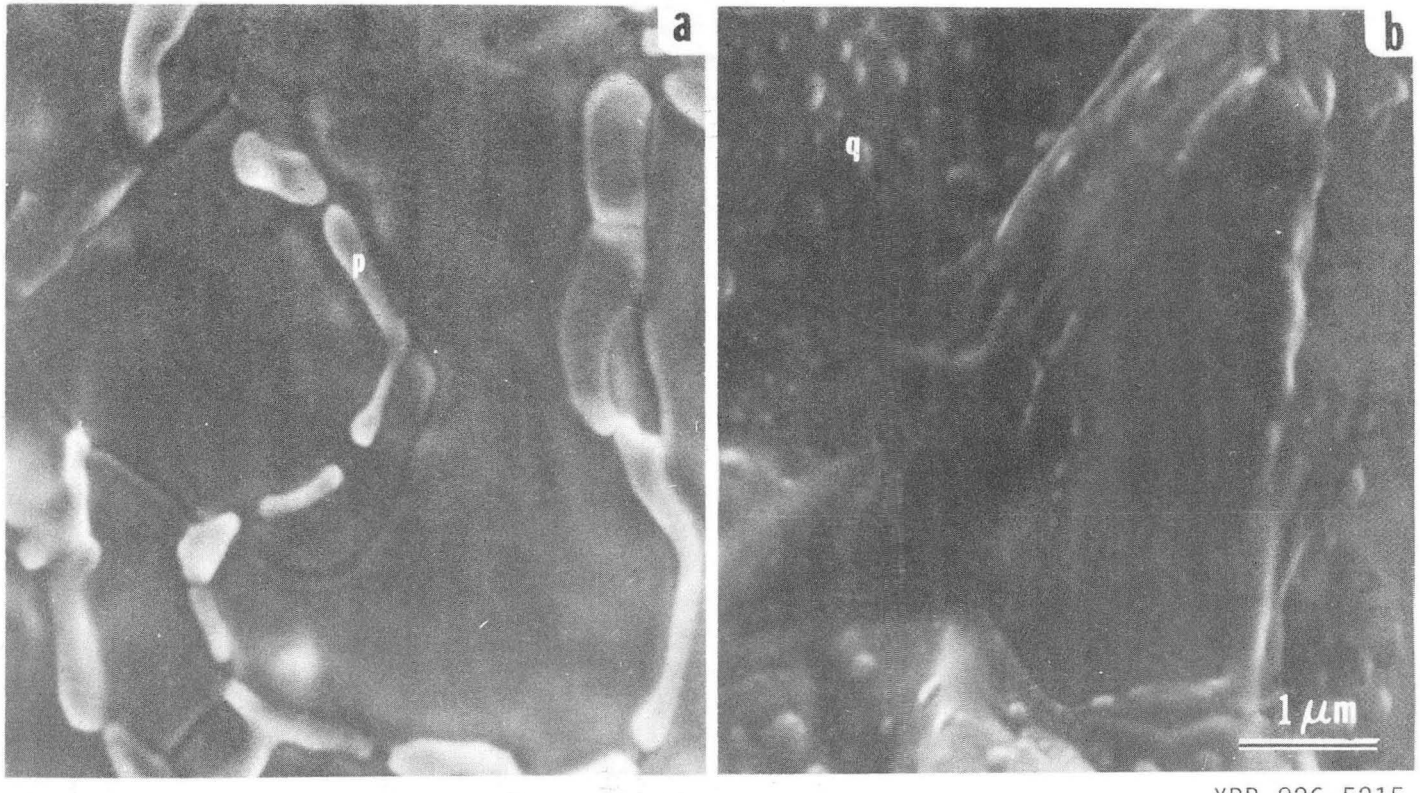

XBB 826-5215

Figure 2 Room temperature microstructure of the same specimen as in figure 1:a) thin CaO coating region, the Ca rich precipitates are distributed in the Ca deficient matrix. b) thick CaO coating region, the round shaped Ca deficient precipitates are distributed in the Ca rich matrix.

Fig.II.2

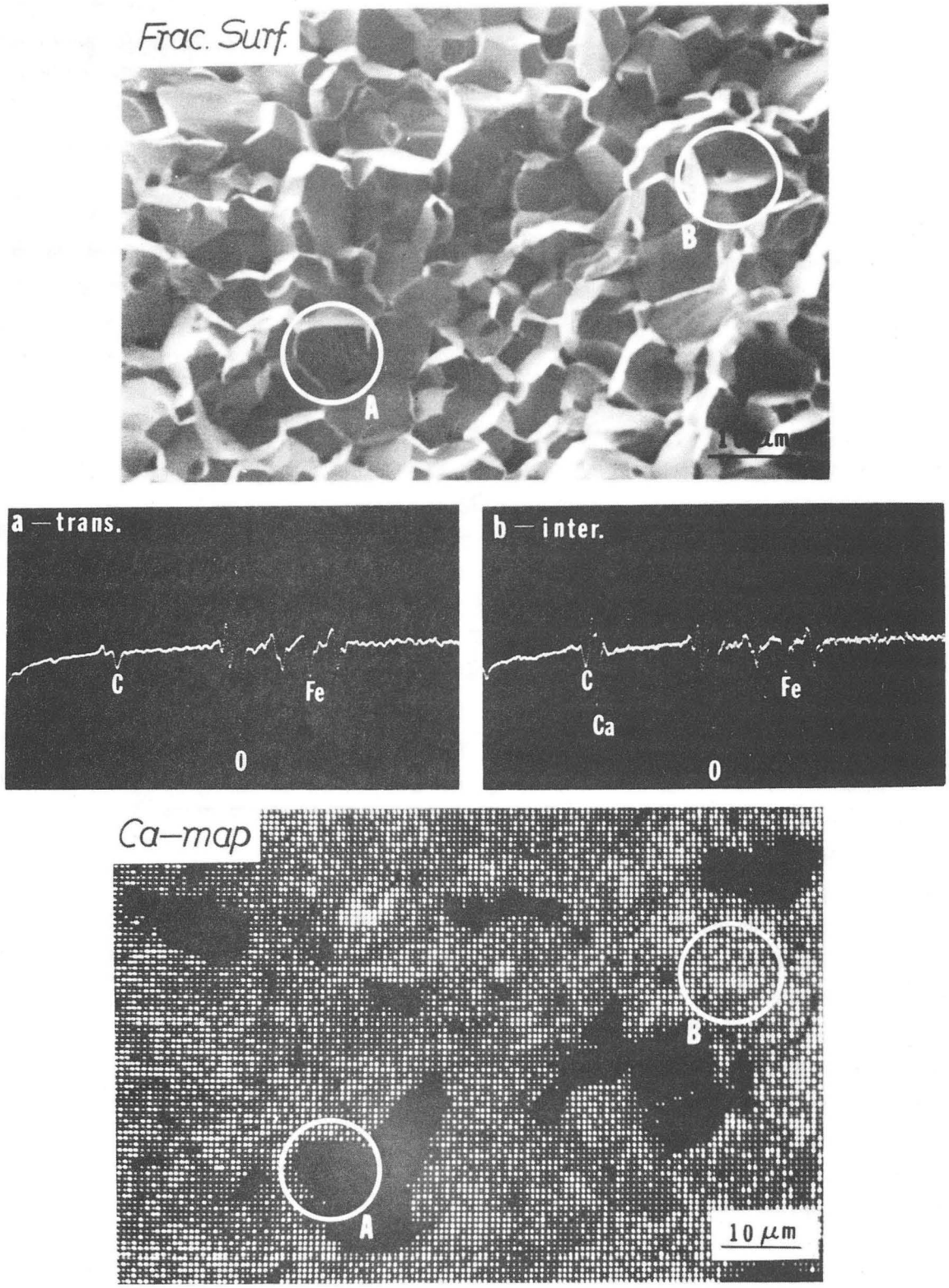

XBB 817-7041

Fig.II.3

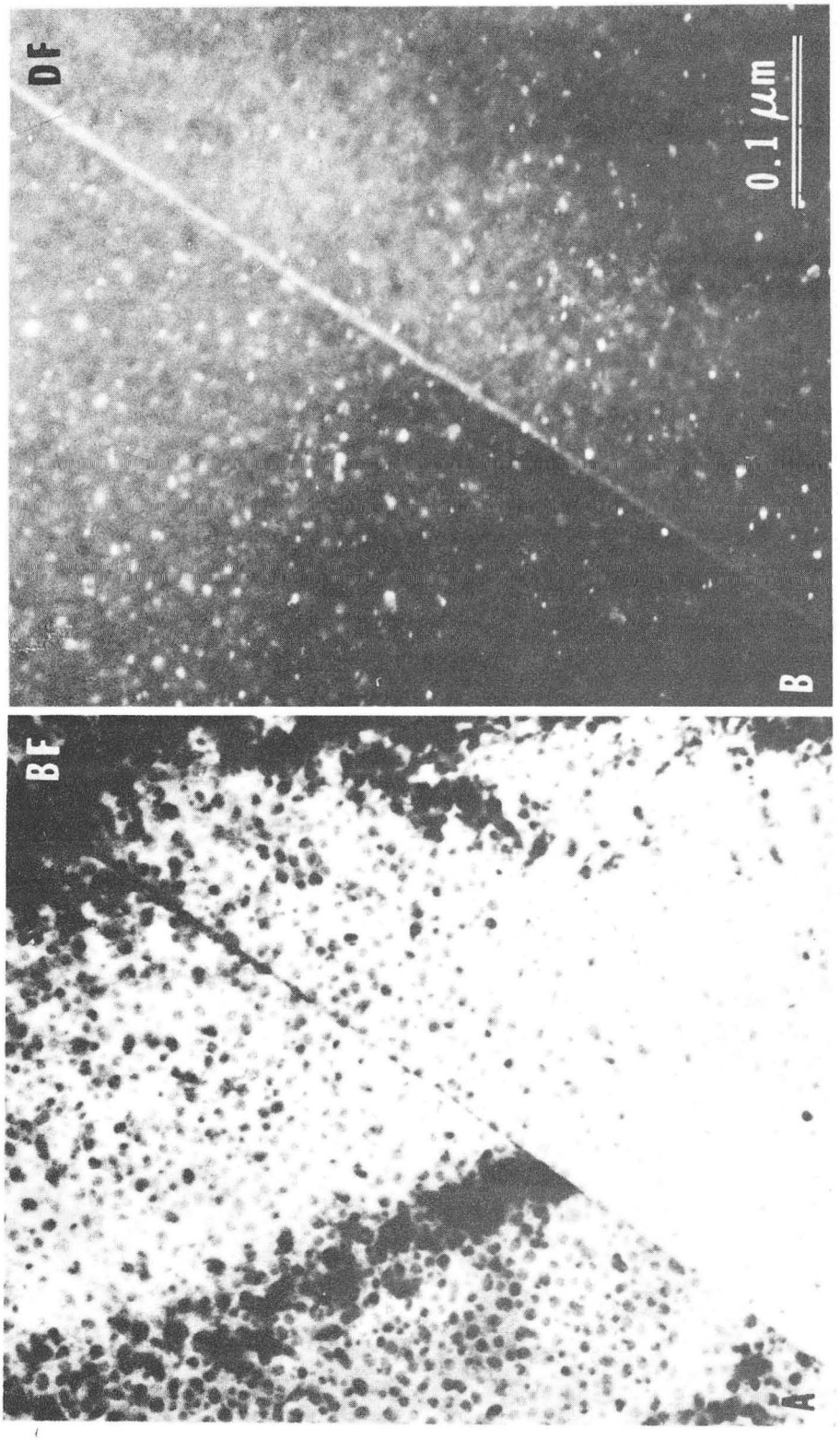

XBB 826-5216

Fig.II.4

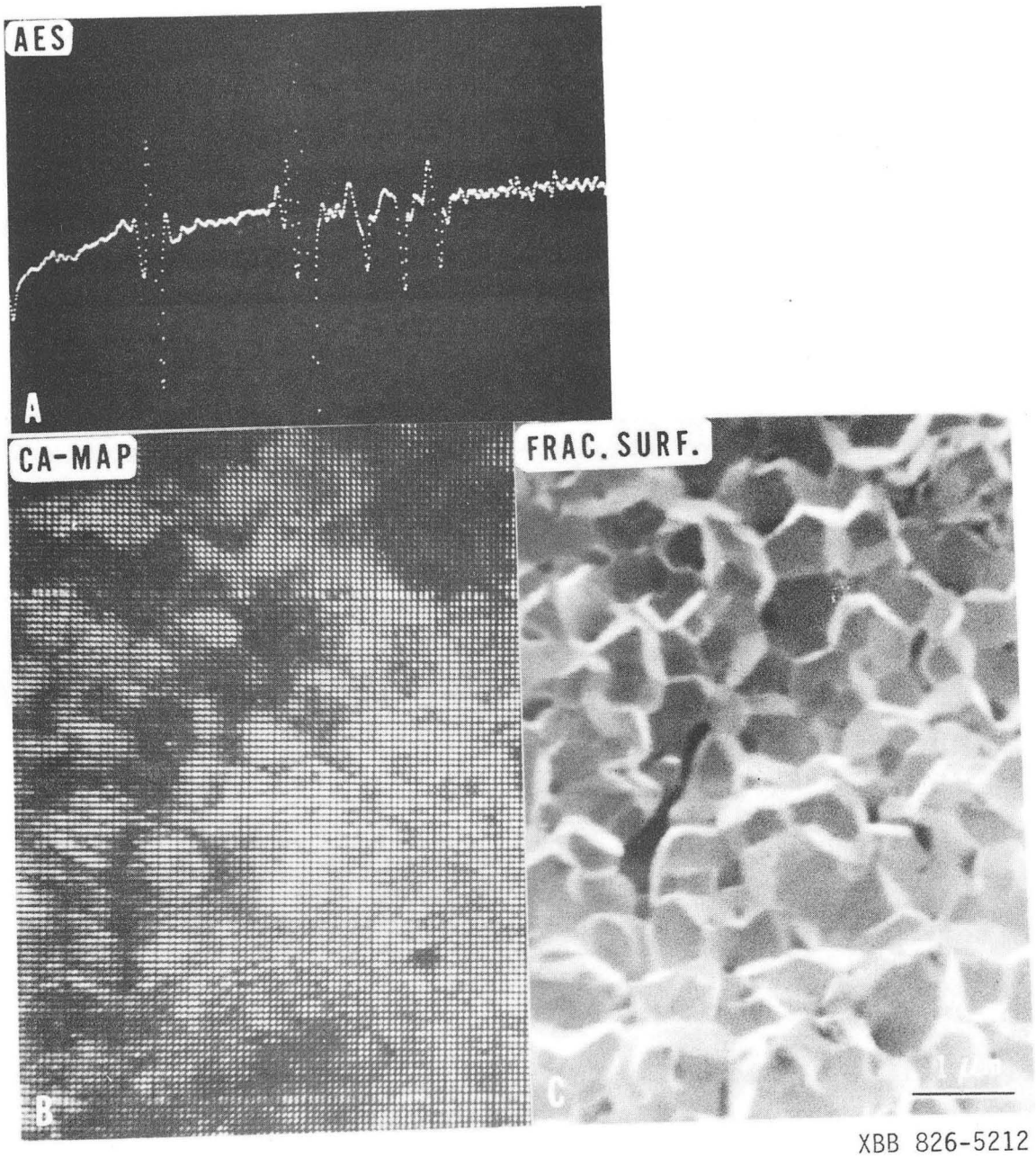

XBB 826-5212

Fig.II.5

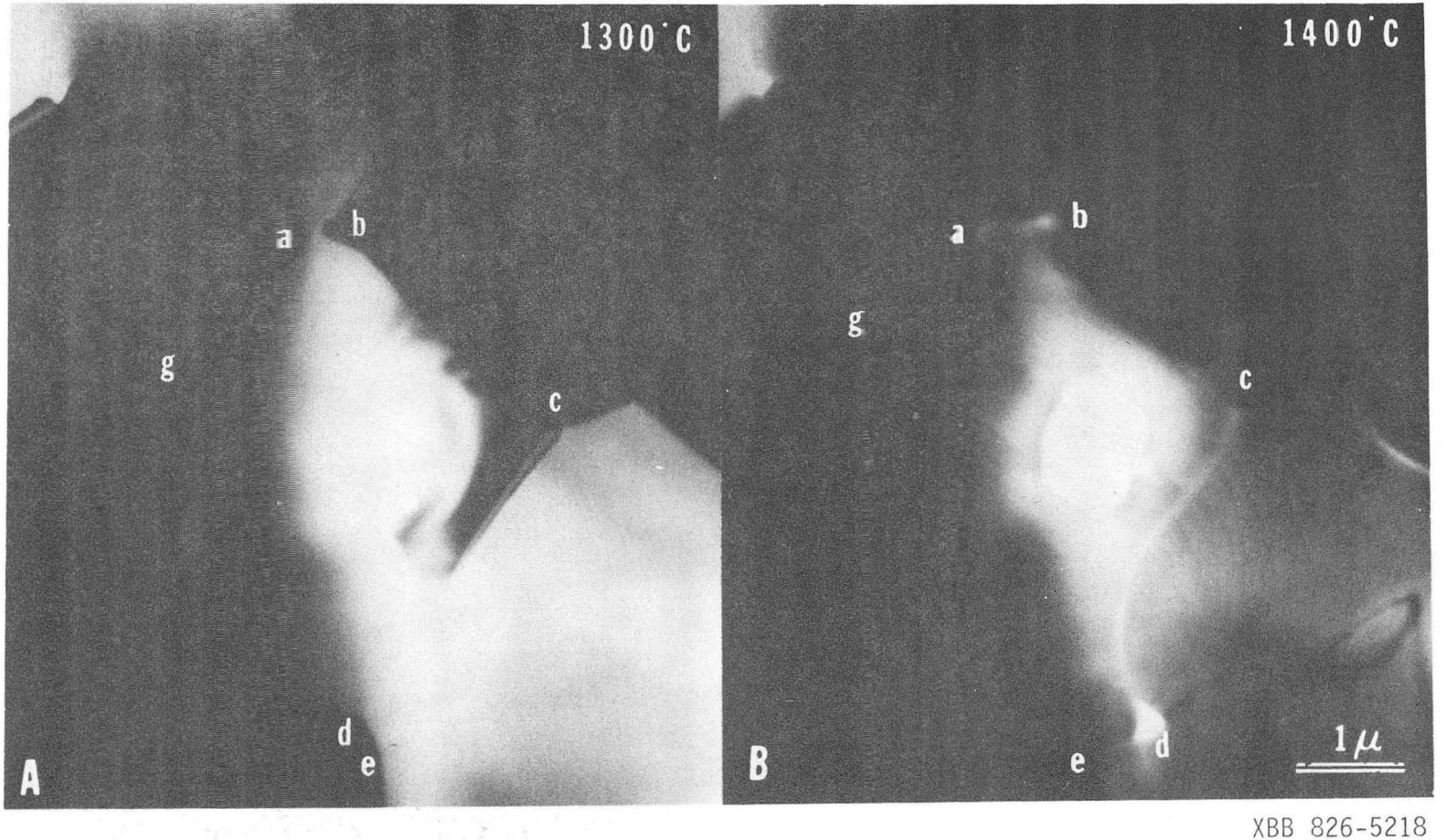

XBB 826-5218

Fig.II.6

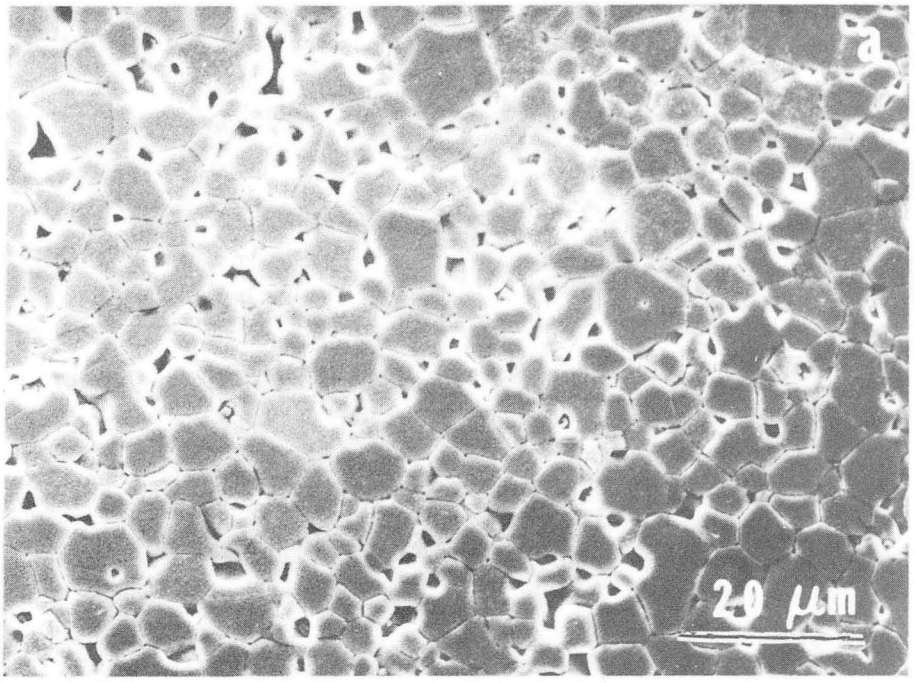

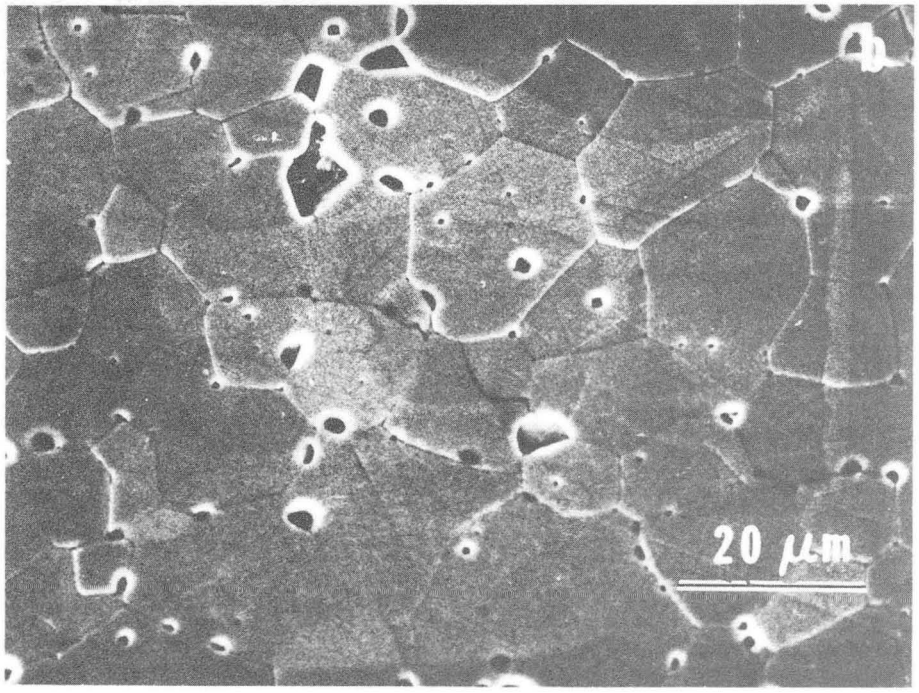

XBB 820-10672

Fig.II.7

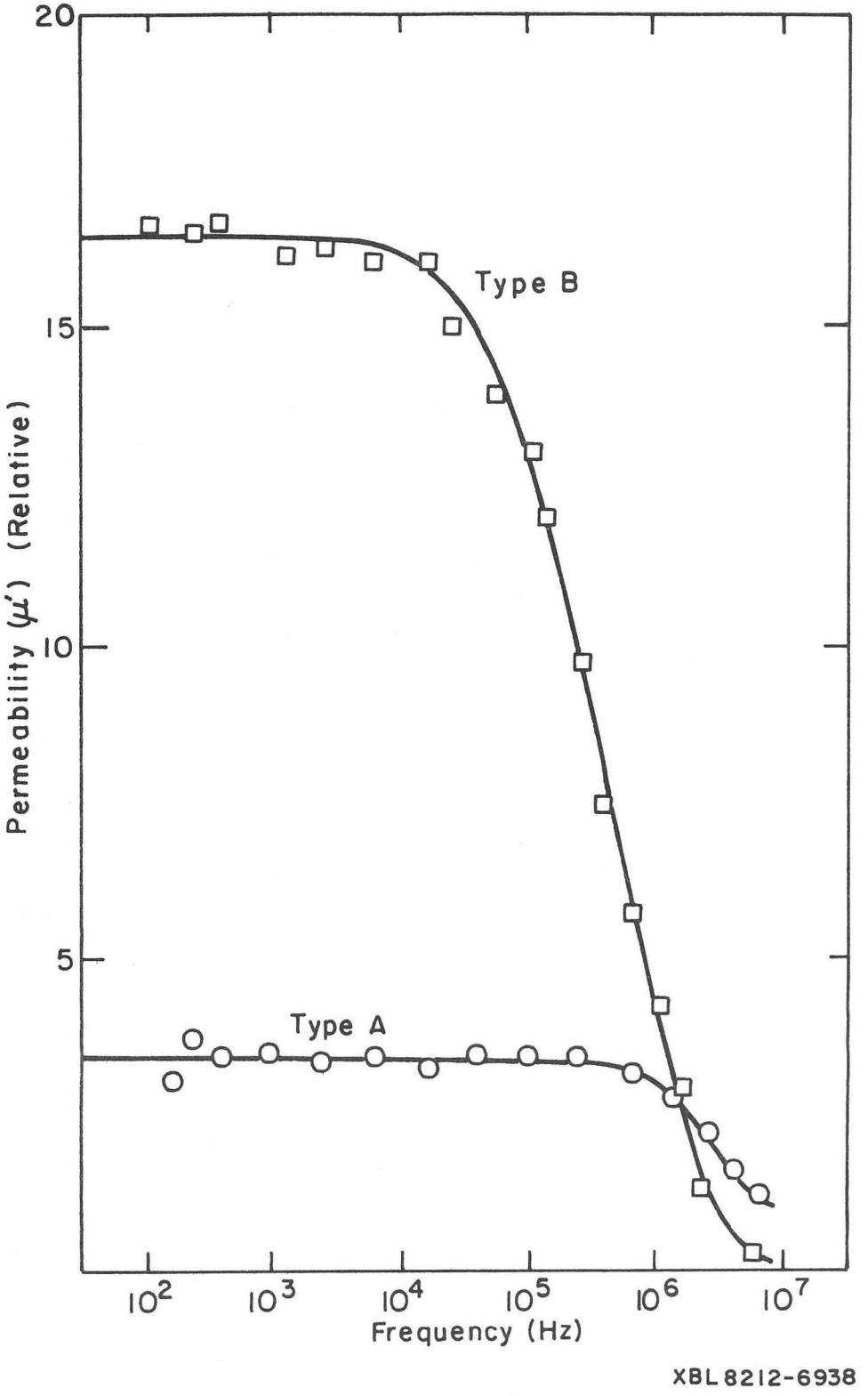
20
15
10
5
Permeability (μ') (Relative)
Type B
Type A
10^2
10^3
10^4
10^5
10^6
10^7
Frequency (Hz)
XBL 8212-6938

Fig.II.8a

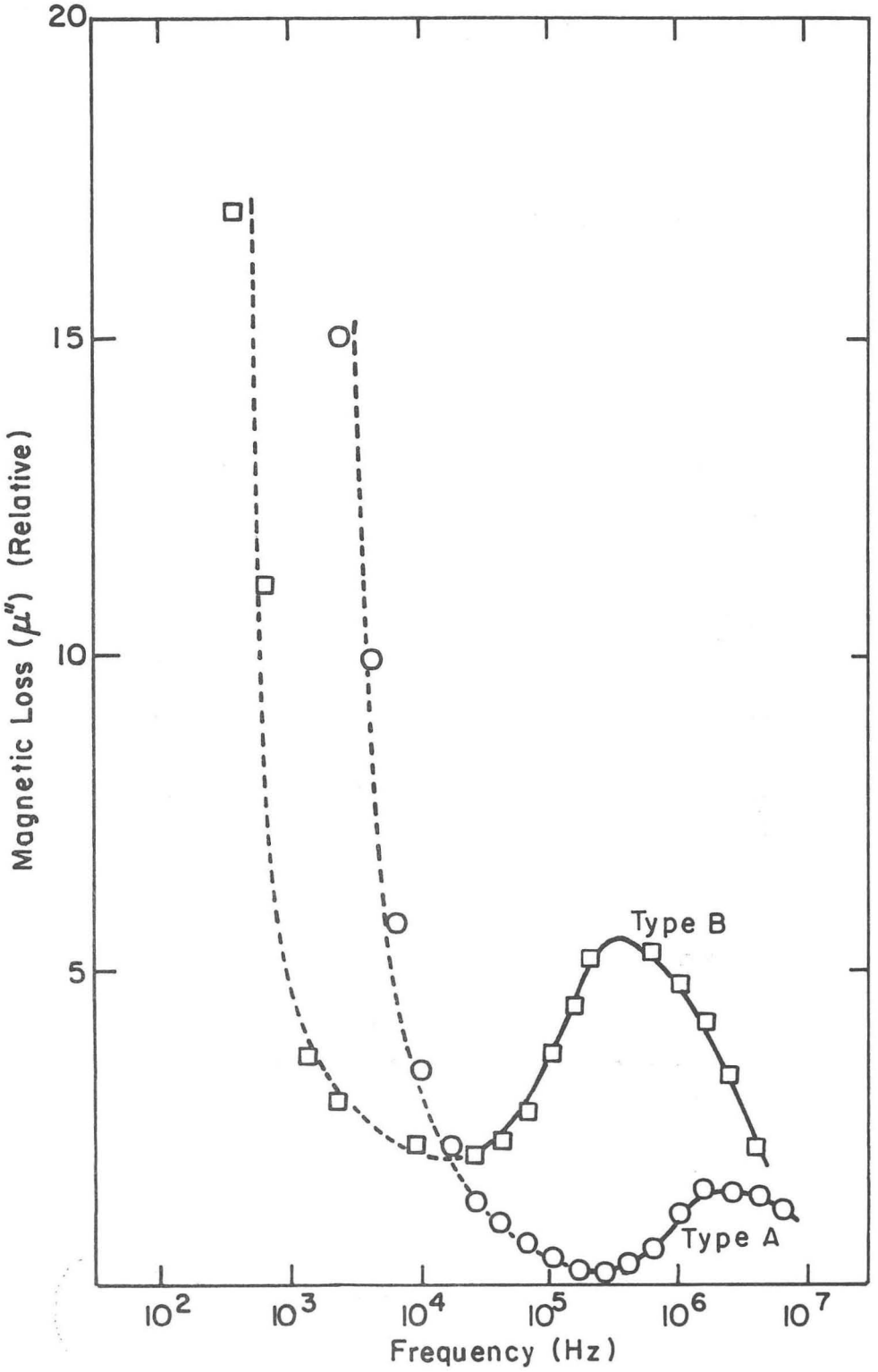
20
15
10
5
Magnetic Loss (μ'') (Relative)
Type B
Type A
10^2
10^3
10^4
10^5
10^6
10^7
Frequency (Hz)
XBL 8212-6939

Fig.II.8b

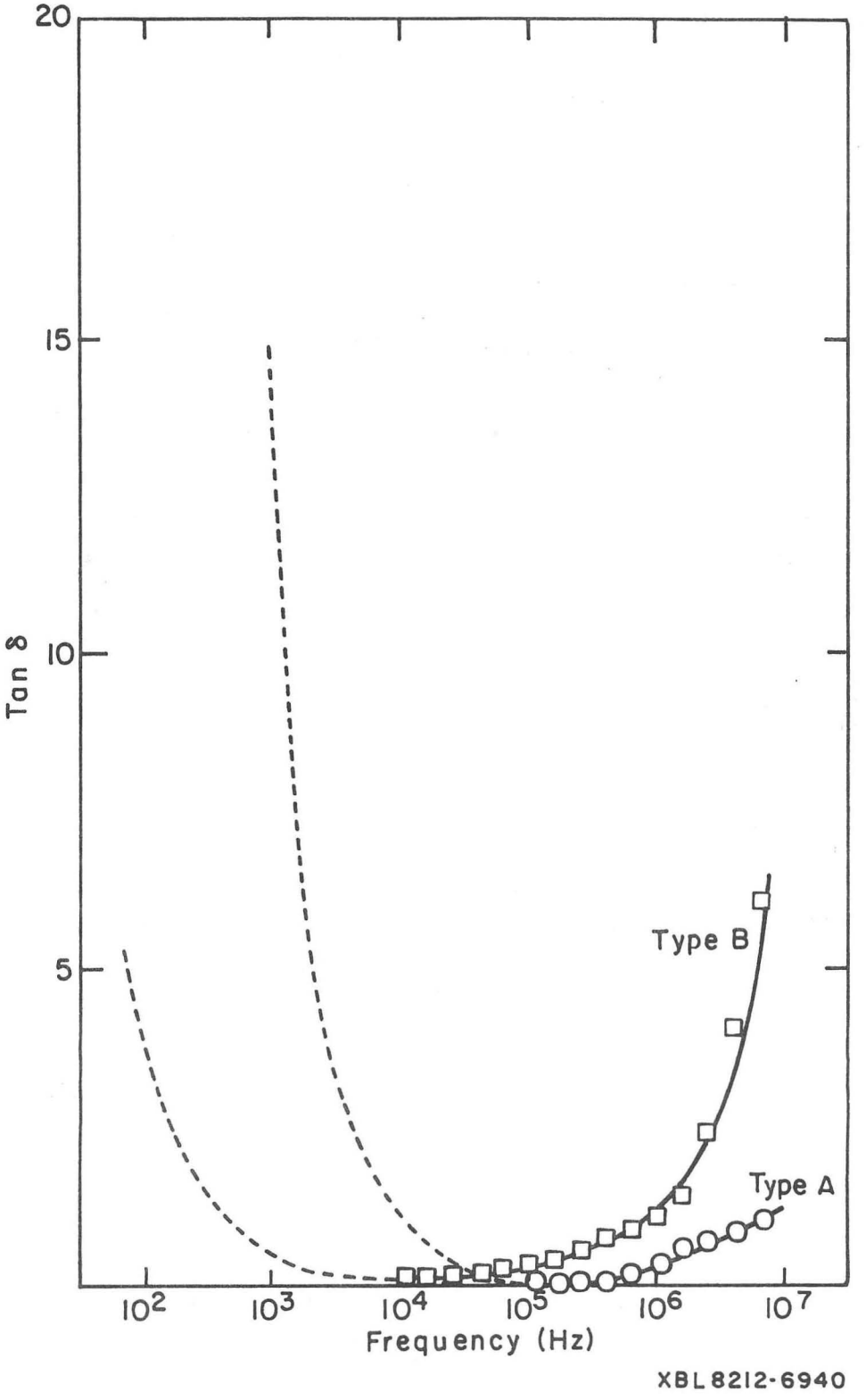
20
15
10
5
Tan δ
Type B
Type A
10^2
10^3
10^4
10^5
10^6
10^7
Frequency (Hz)
XBL8212-6940

Fig.II.8c

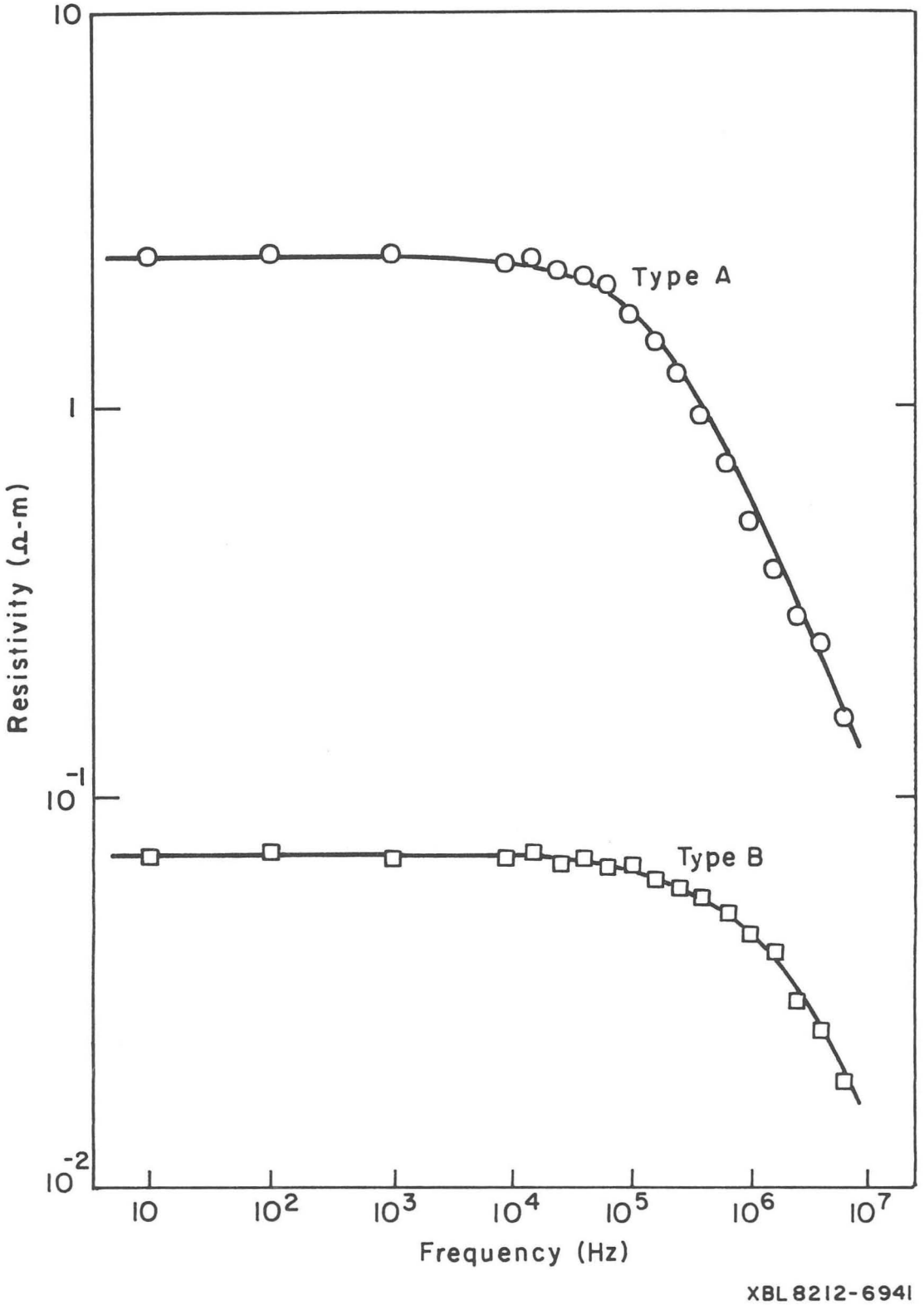
10
1
10^{-1}
10^{-2}
Resistivity (Ω-m)
Type A
Type B
10
10^2
10^3
10^4
10^5
10^6
10^7
Frequency (Hz)
XBL 8212-6941

Fig.II.9a

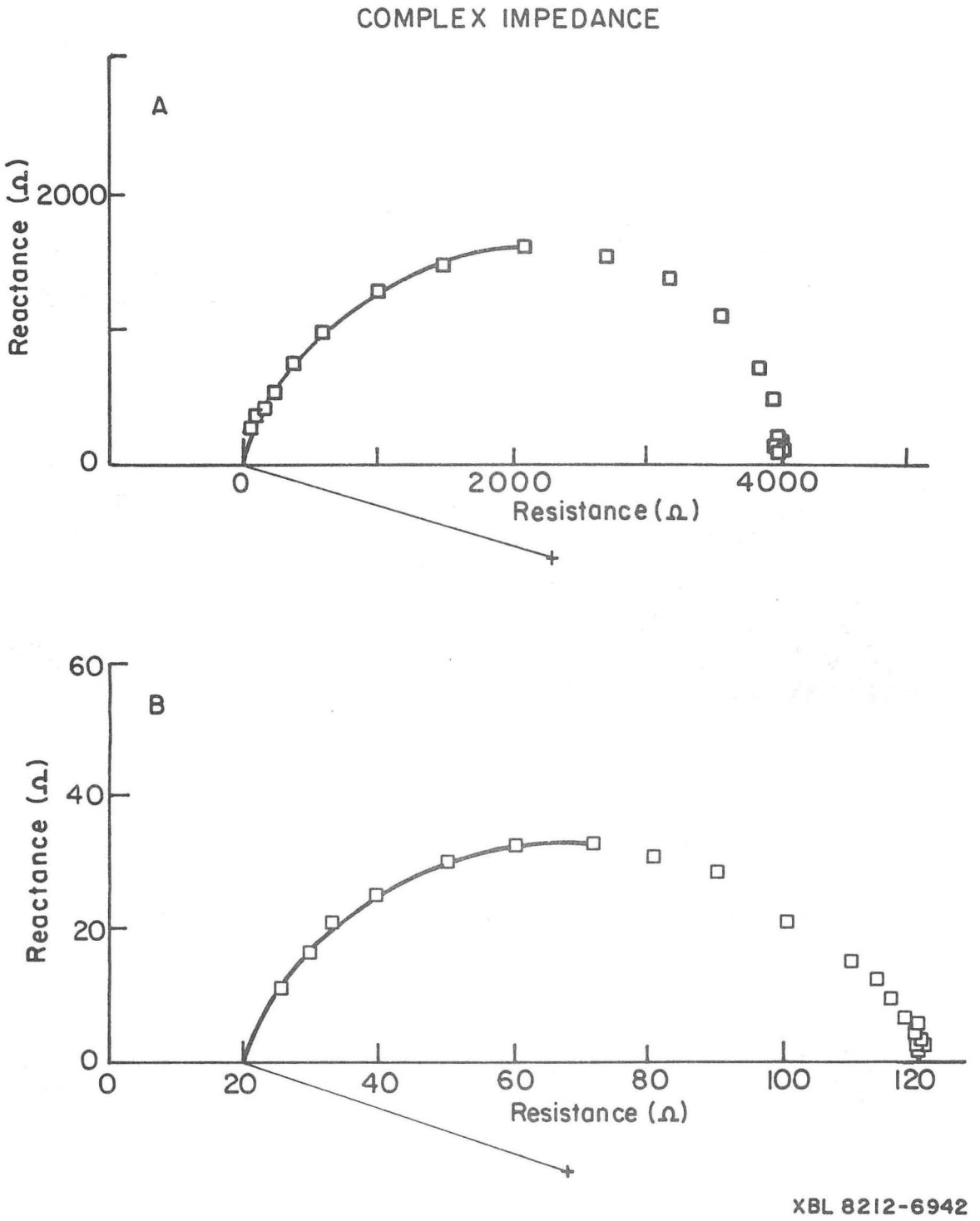
COMPLEX IMPEDANCE
A
Reactance (Ω)
2000
0
0
2000
4000
Resistance (Ω)
B
Reactance (Ω)
60
40
20
0
0
20
40
60
80
100
120
Resistance (Ω)
XBL 8212-6942

Fig.II.9b

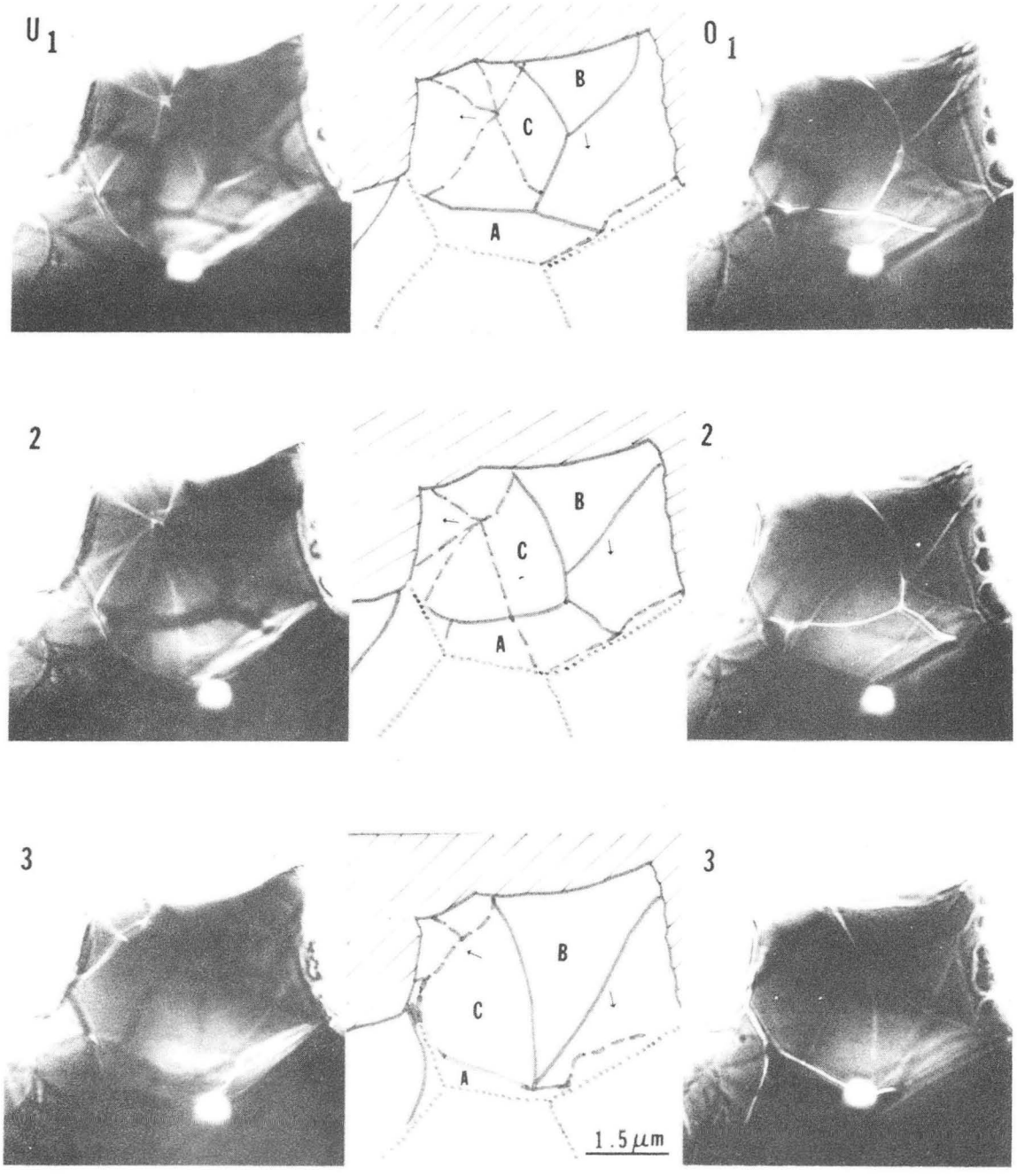

XBB 800-11965

Fig.II.10

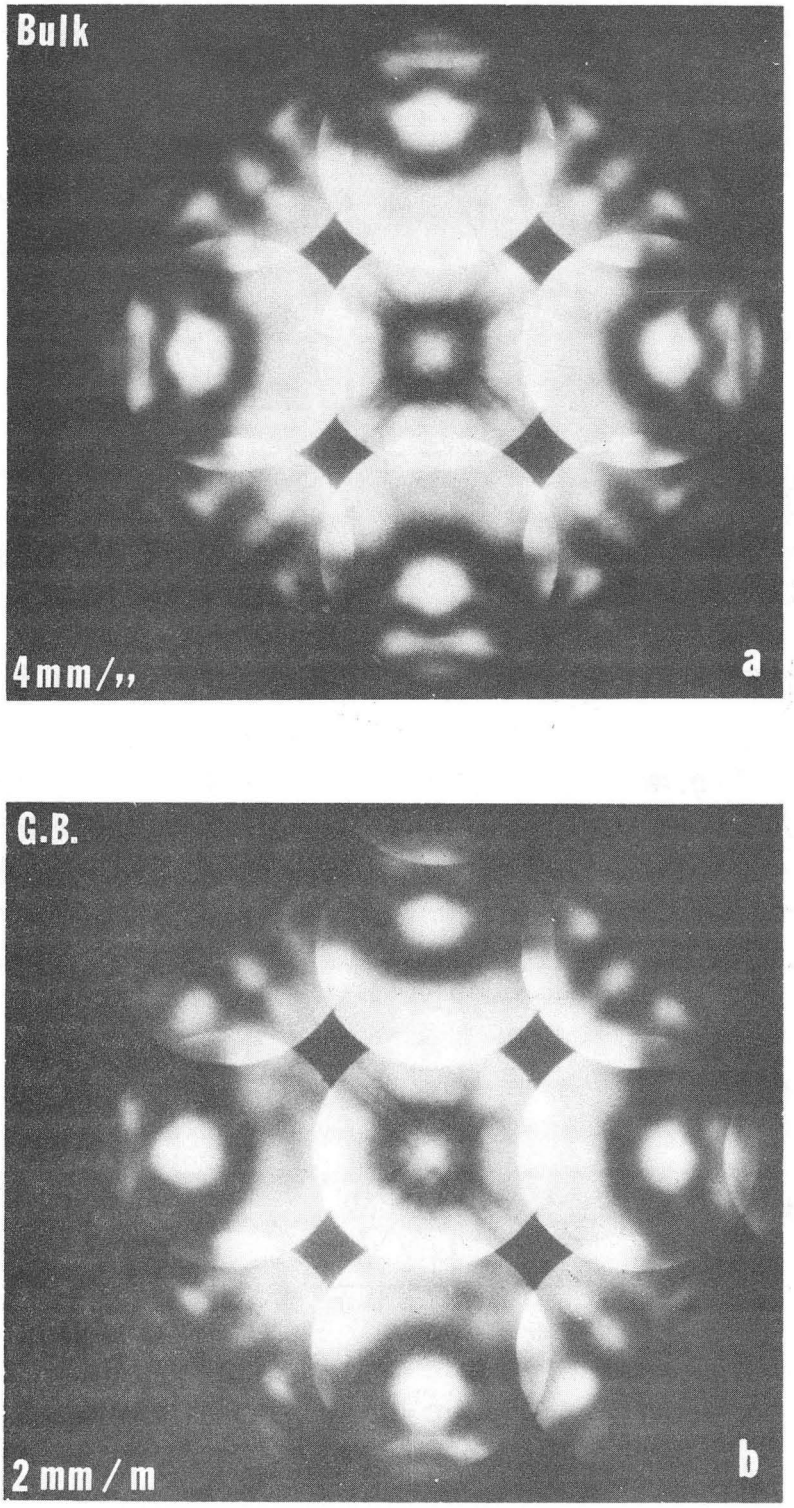

XBB 817-7040

Fig.II.11

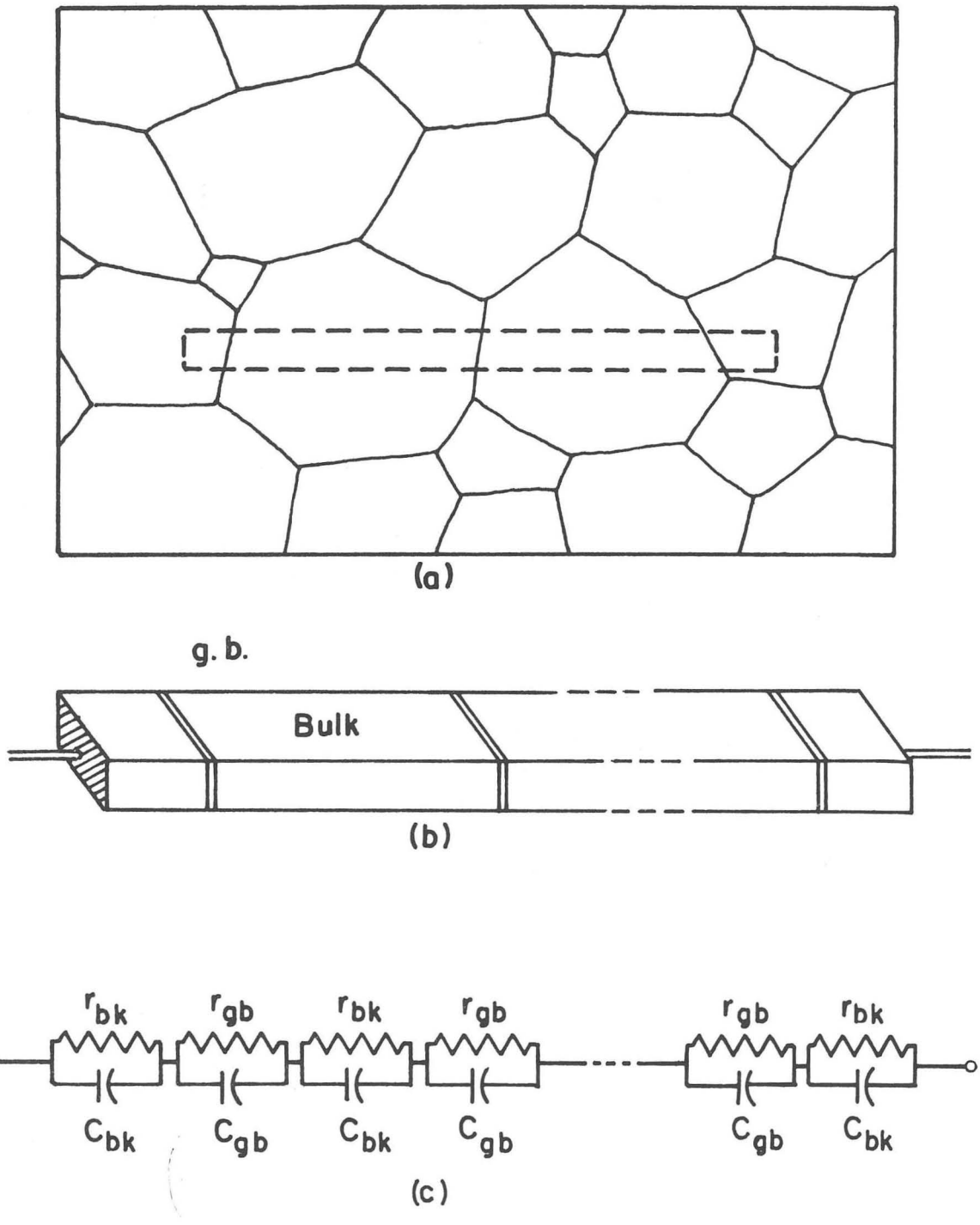
(a)
g. b.
Bulk
(b)
r_{bk}
r_{gb}
r_{bk}
r_{gb}
r_{gb}
r_{bk}
C_{bk}
C_{gb}
C_{bk}
C_{gb}
C_{gb}
C_{bk}
(c)
XBL8212-6943

Fig.II.12

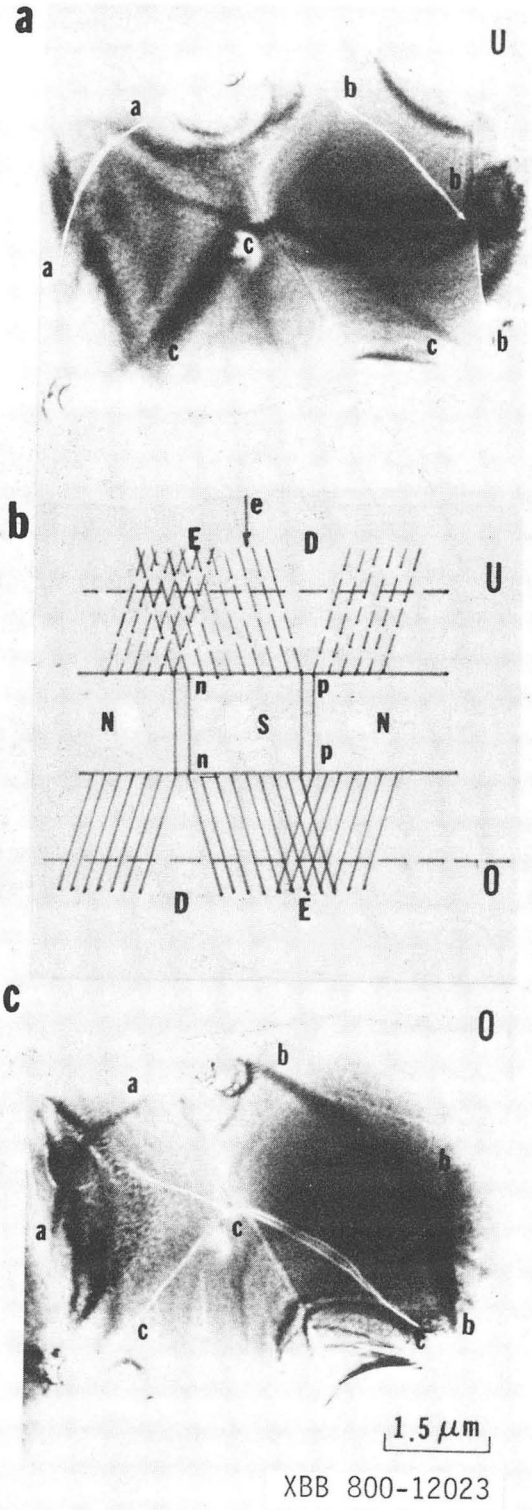

XBB 800-12023

Fig.III.1

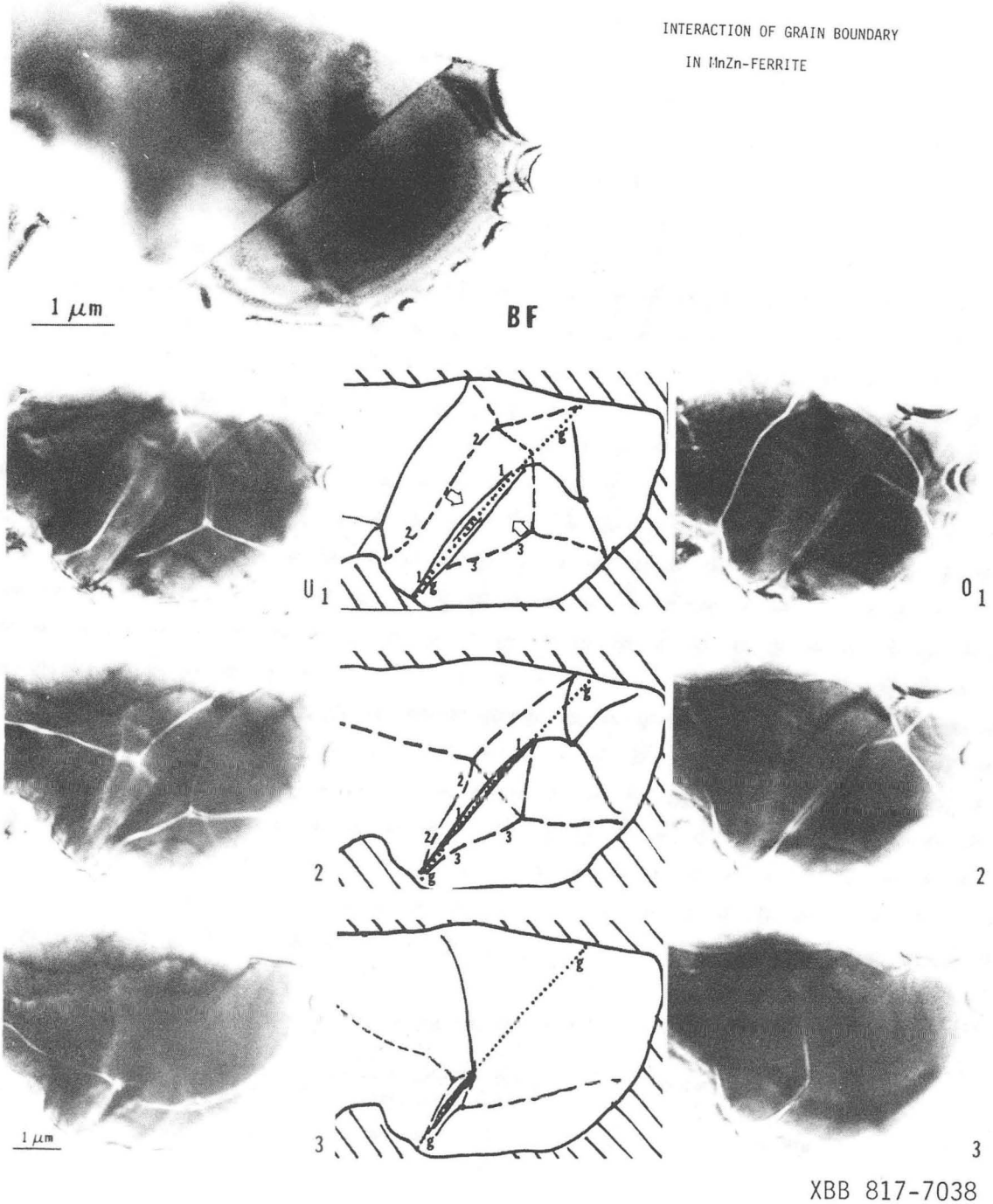
INTERACTION OF GRAIN BOUNDARY
IN MnZn-FERRITE
1 μm
BF
U 1
O 1
2
2
3
3
1 μm
XBB 817-7038

Fig.III.2

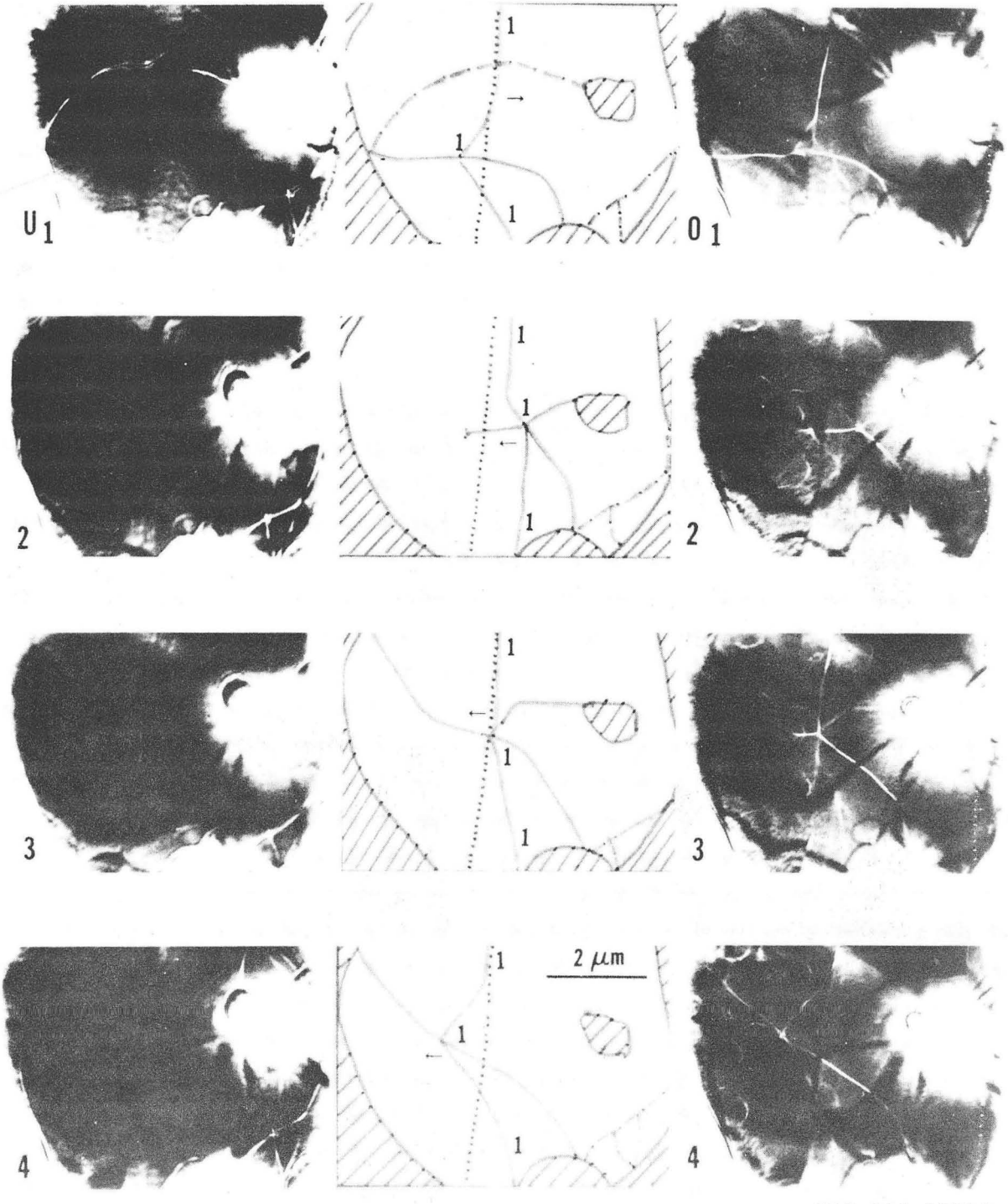

XBB 800-12016

Fig.III.3

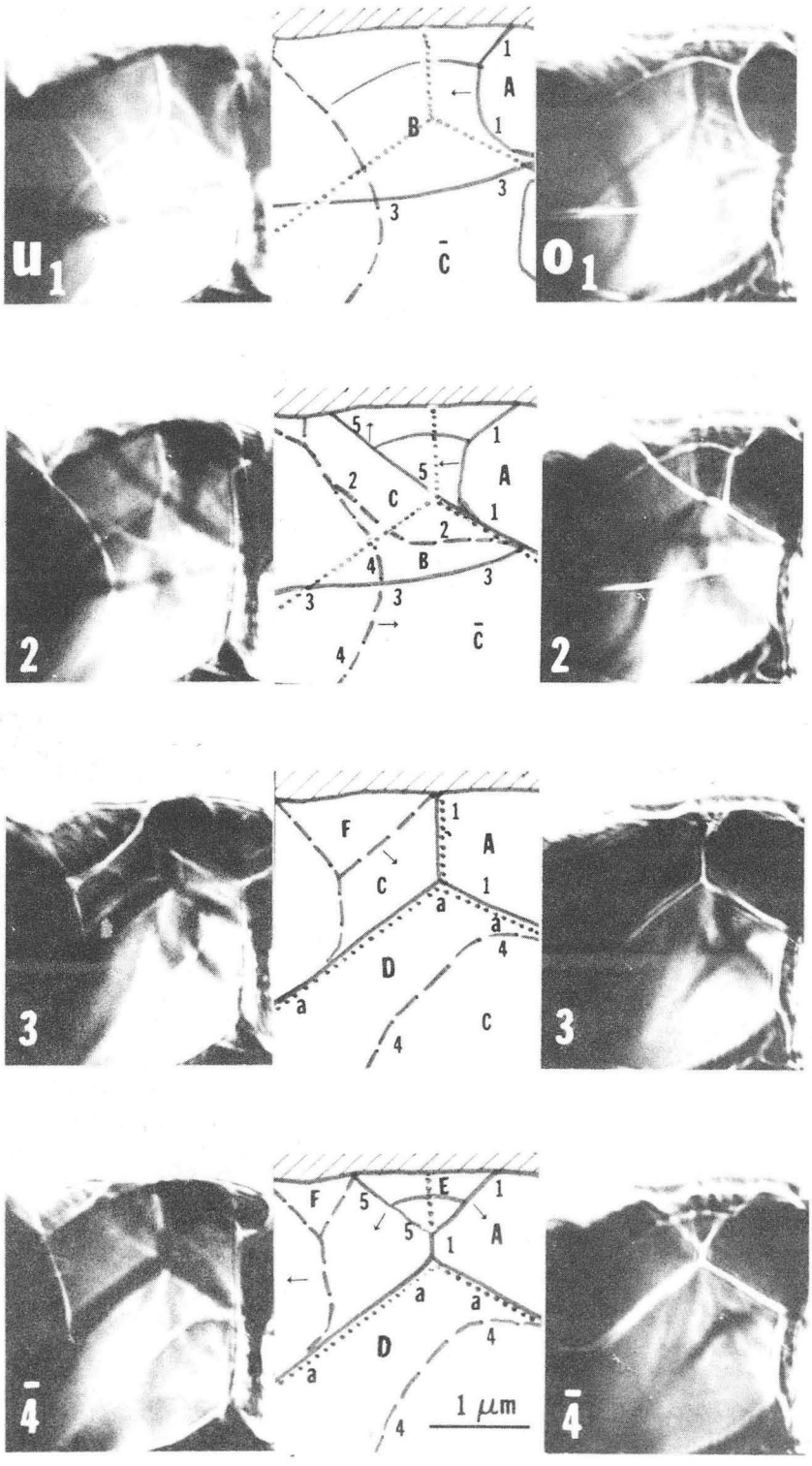

XBB 800-11966

Fig.III.4

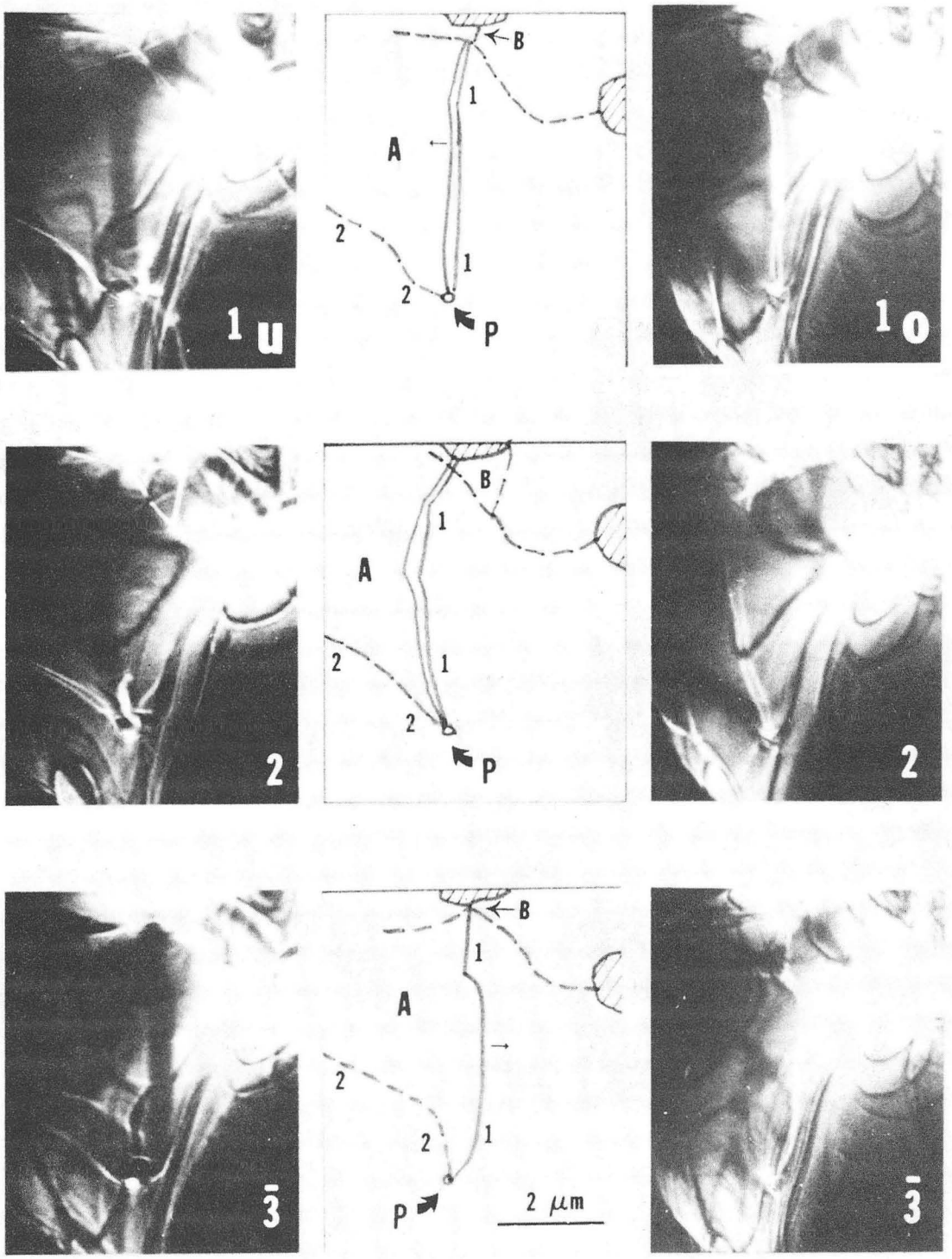

XBB 800-11964

Fig.III.5

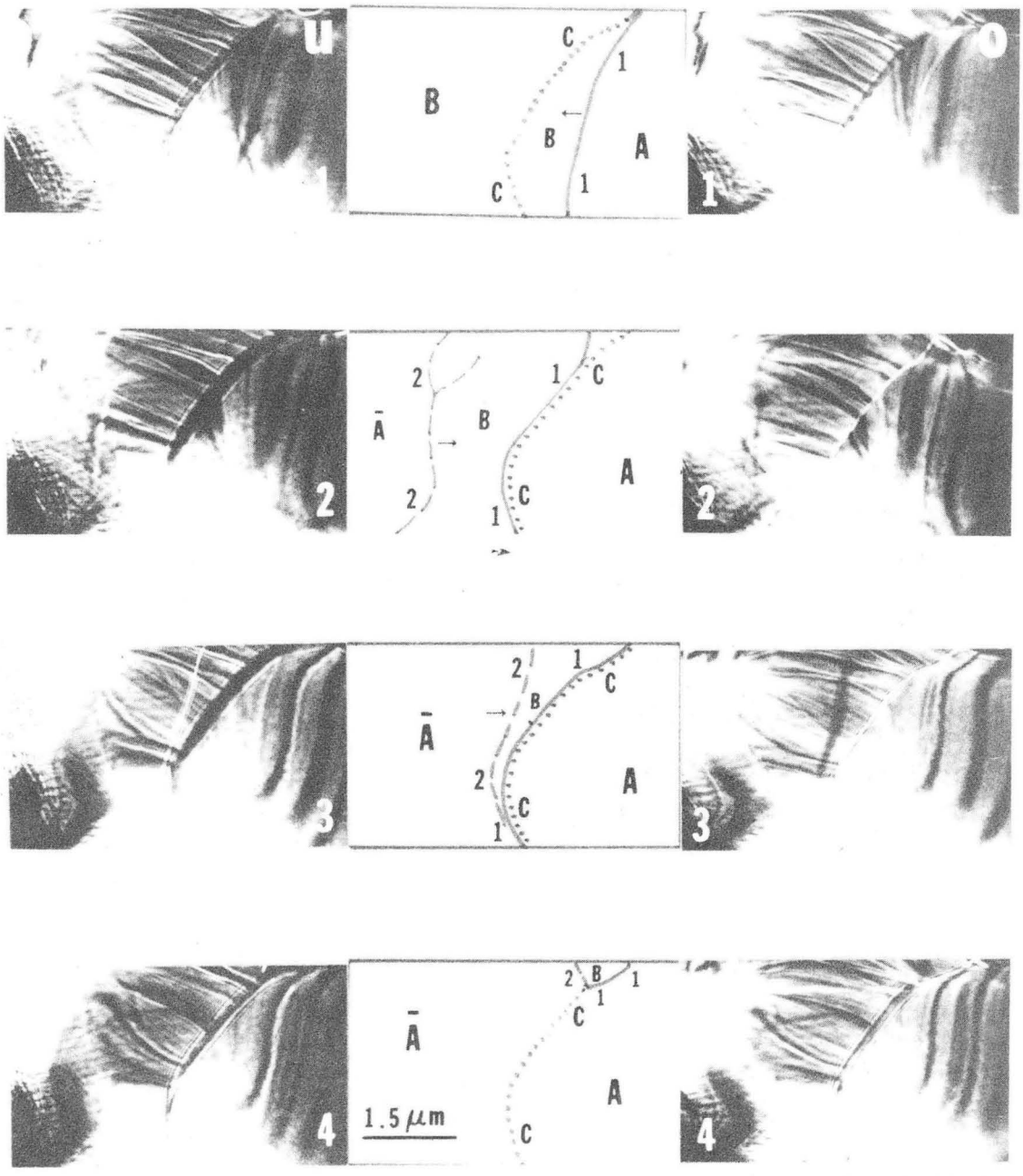

XBB 800-11962

Fig.III.6

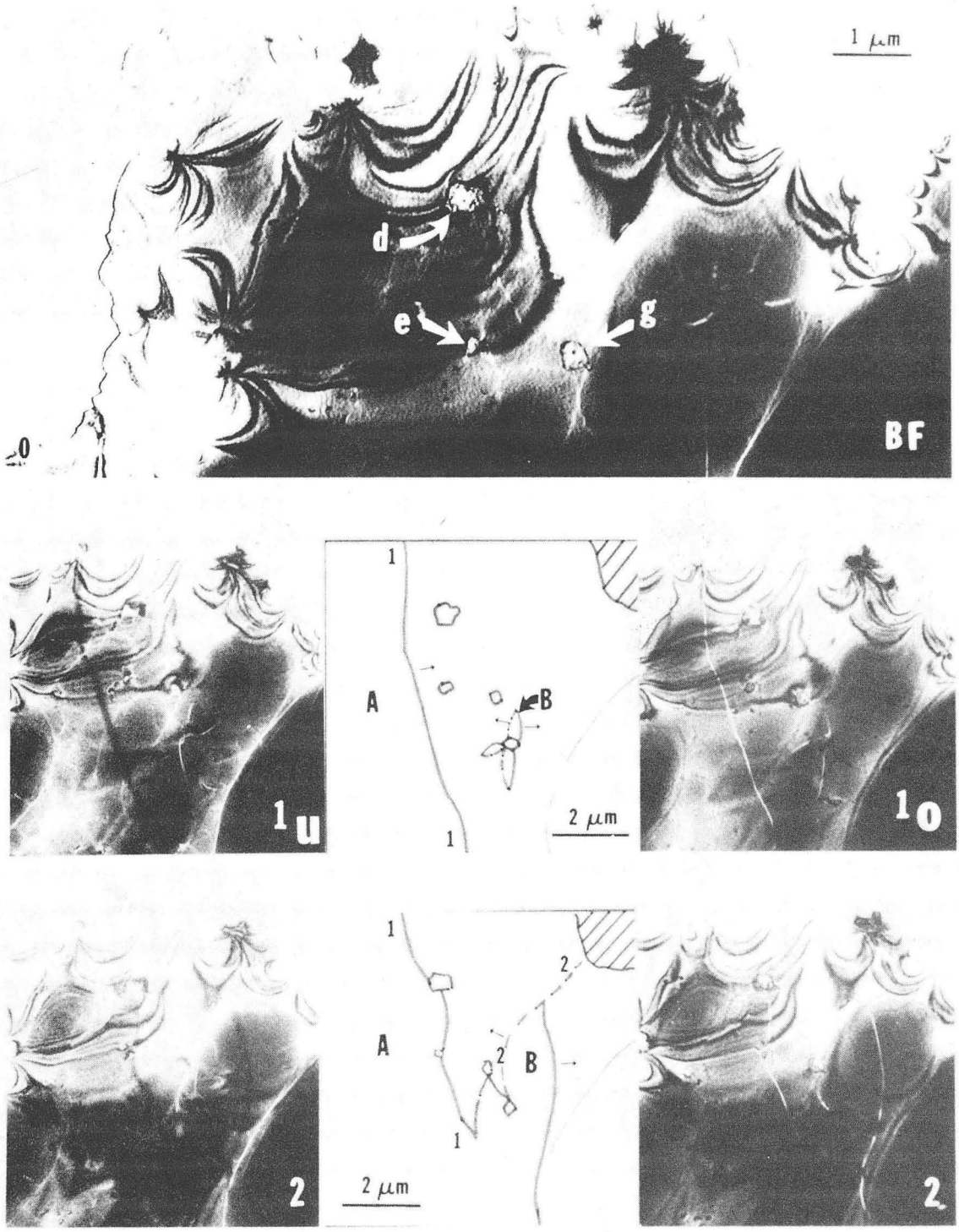

XBB 800-11967

Fig.III.7a

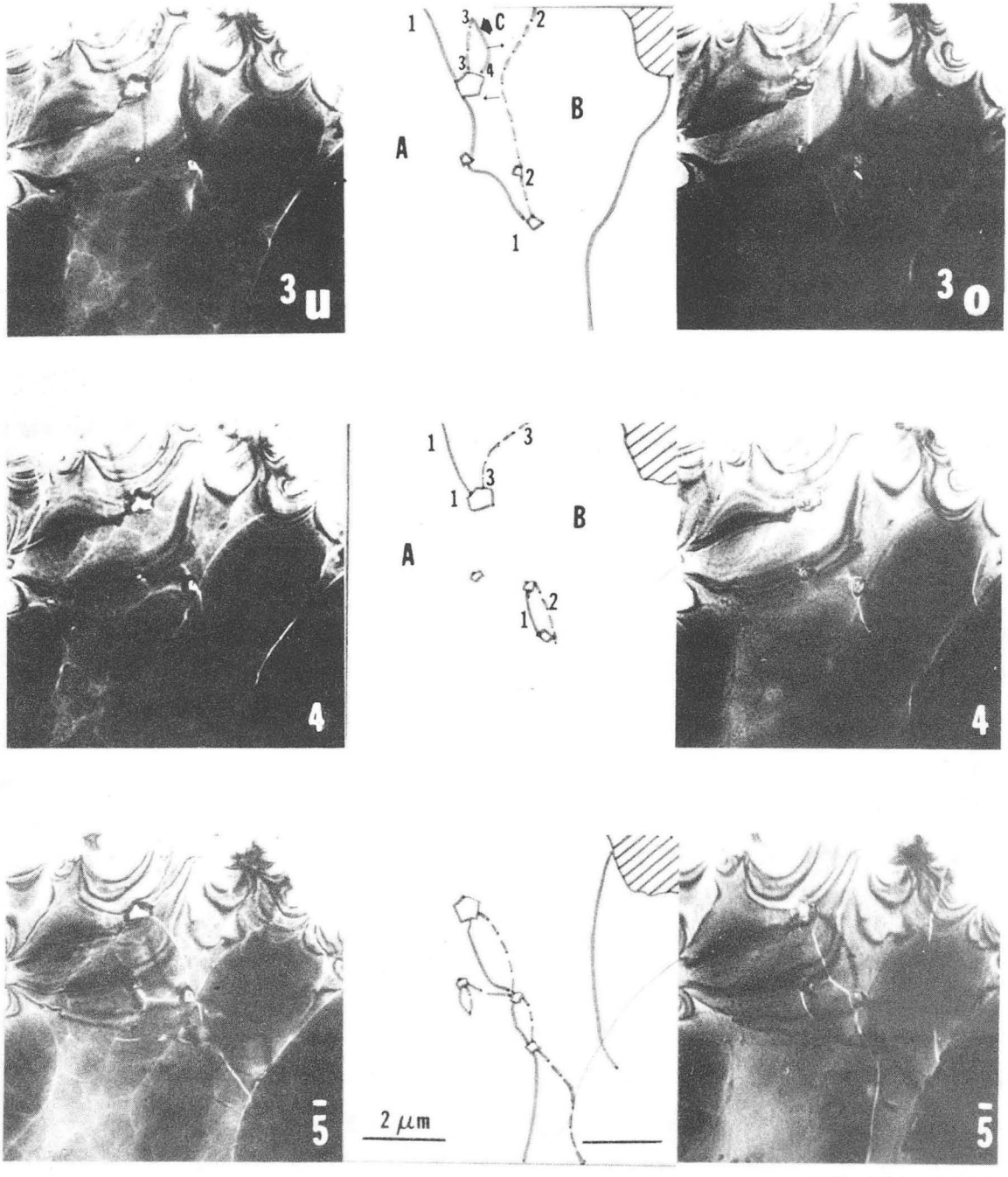

XBB 800-11968

Fig.III.7b

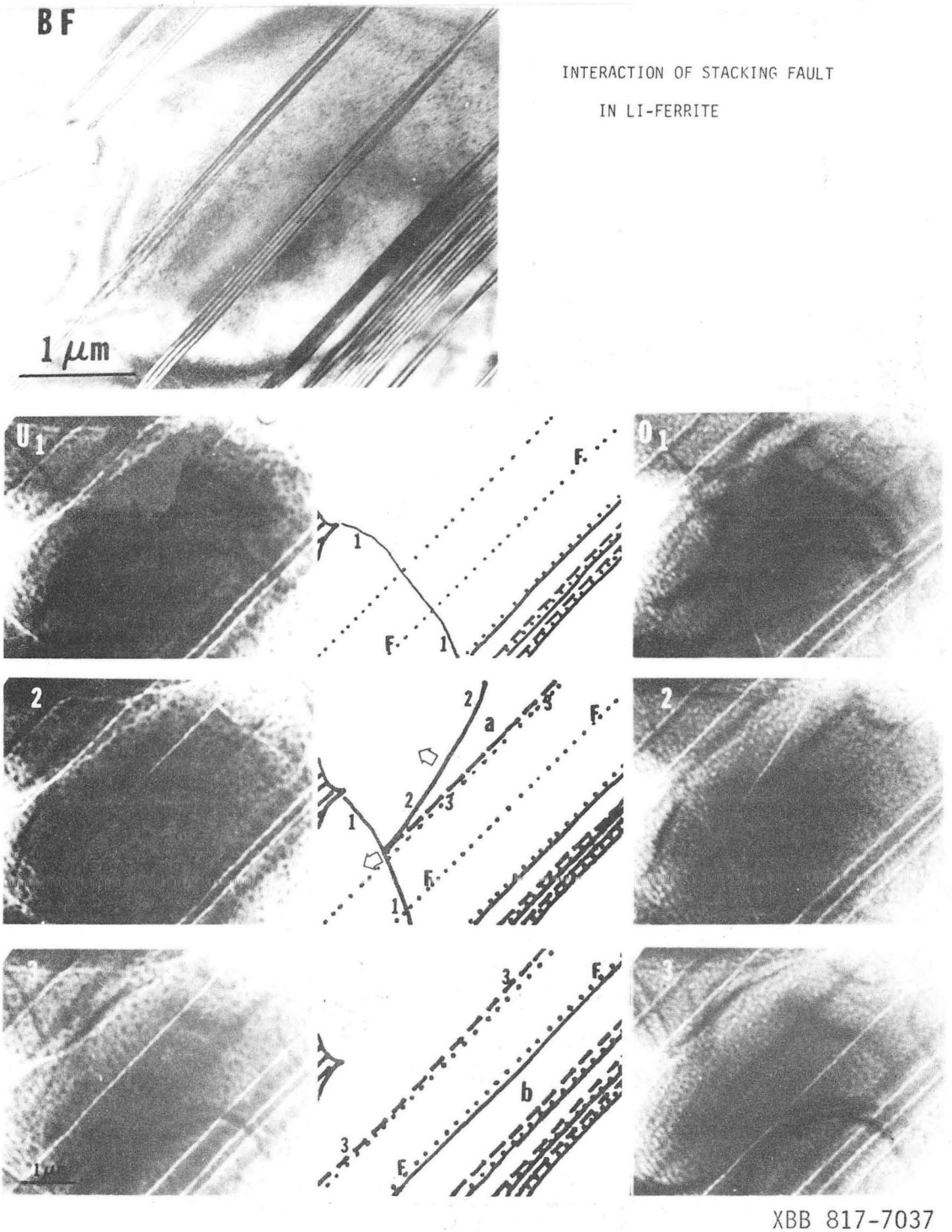
BF
1 μm
INTERACTION OF STACKING FAULT
IN LI-FERRITE
U1
O1
2
3
F
a
b
1 μm
XBB 817-7037

Fig.III.8

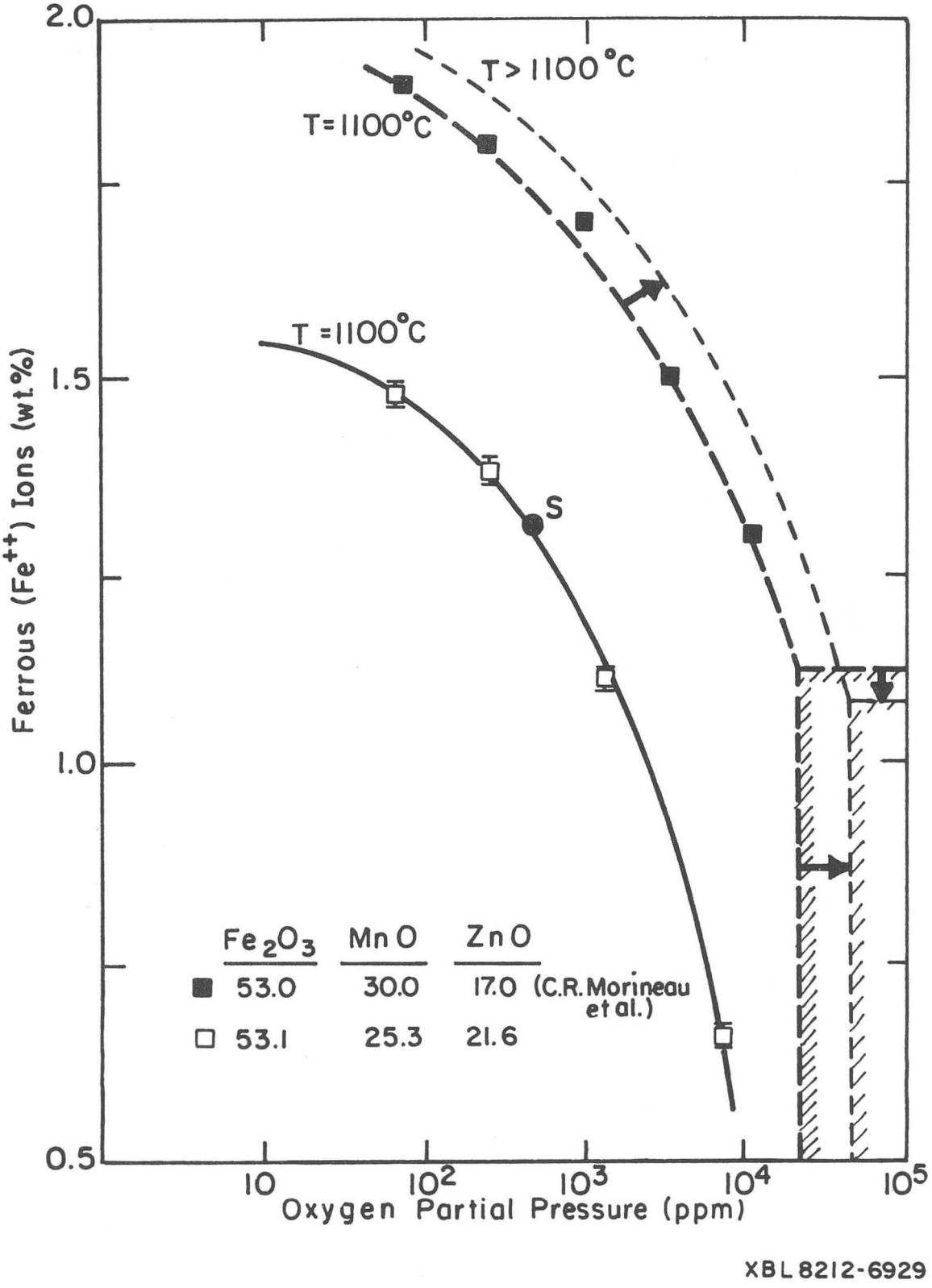
2.0
1.5
1.0
0.5
Ferrous (Fe^{++}) Ions (wt%)
T > 1100°C
T = 1100°C
T = 1100°C
S
Fe_2O_3 MnO ZnO
53.0 30.0 17.0 (C.R. Morineau et al.)
53.1 25.3 21.6
10
10^2
10^3
10^4
10^5
Oxygen Partial Pressure (ppm)
XBL 8212-6929

Fig.IV.1

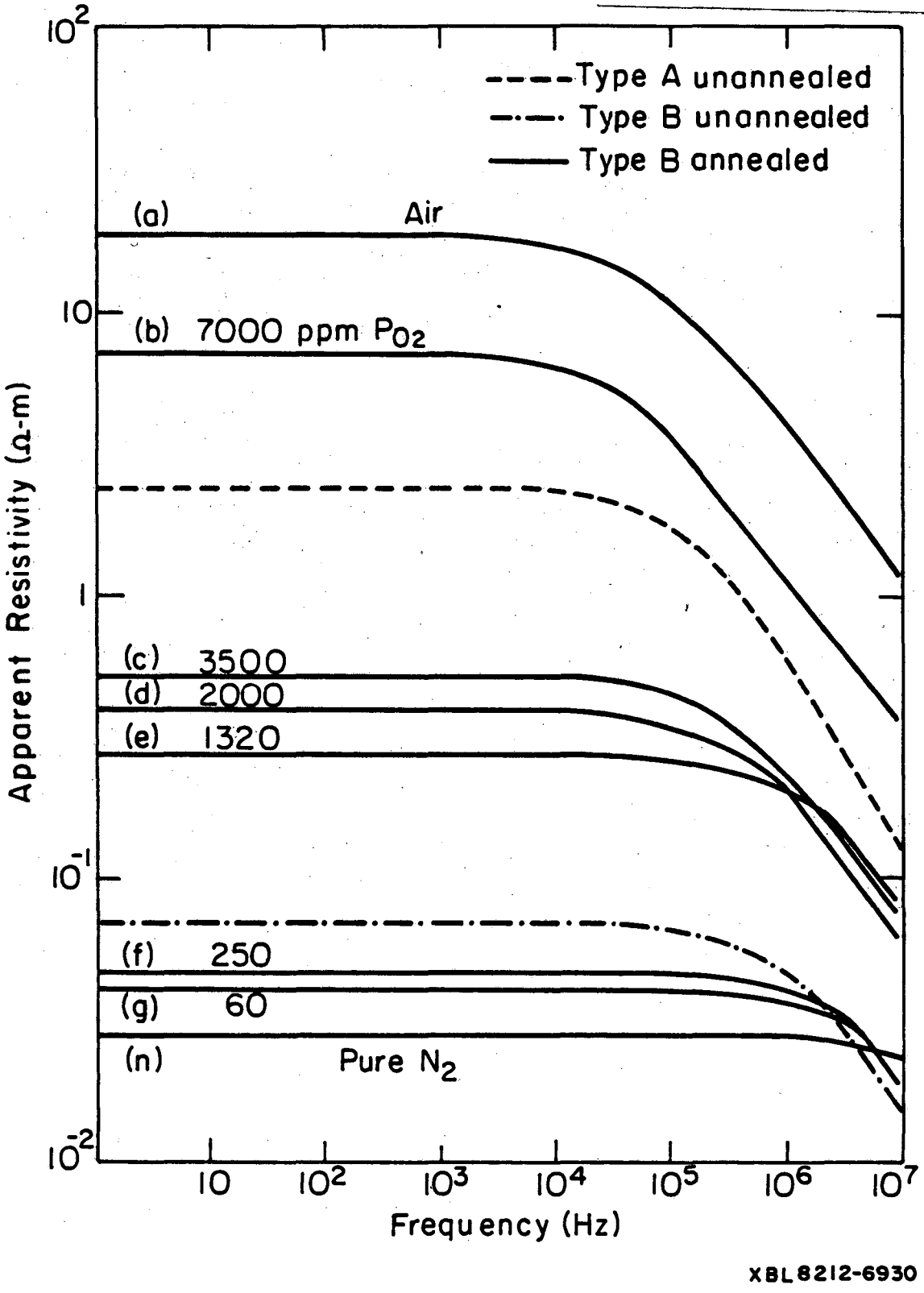
Type A unannealed
Type B unannealed
Type B annealed
(a) Air
(b) 7000 ppm P_{O2}
(c) 3500
(d) 2000
(e) 1320
(f) 250
(g) 60
(n) Pure N_2
Apparent Resistivity (Ω-m)
Frequency (Hz)
10^2
10
1
10^{-1}
10^{-2}
10
10^2
10^3
10^4
10^5
10^6
10^7
XBL8212-6930

Fig.IV.2

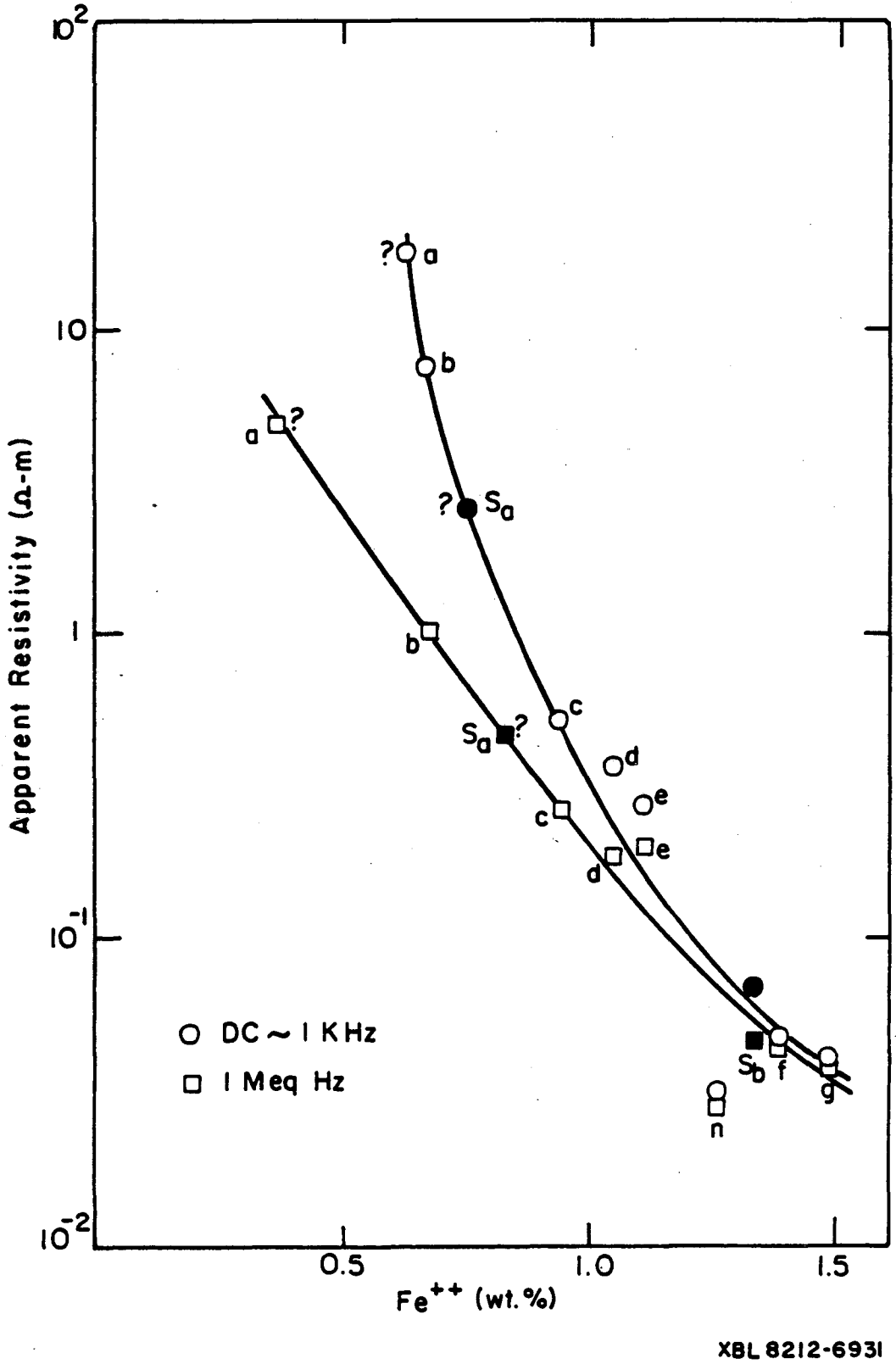
Apparent Resistivity (Ω-m)
10²
10
1
10⁻¹
10⁻²
0.5
1.0
1.5
Fe⁺⁺ (wt.%)
O DC ~ 1 KHz
□ 1 Meq Hz
?a
b
?Sa
c
d
e
f
g
n
a?
b
Sa?
c
d
e
Sb
XBL 8212-6931

Fig.IV.3

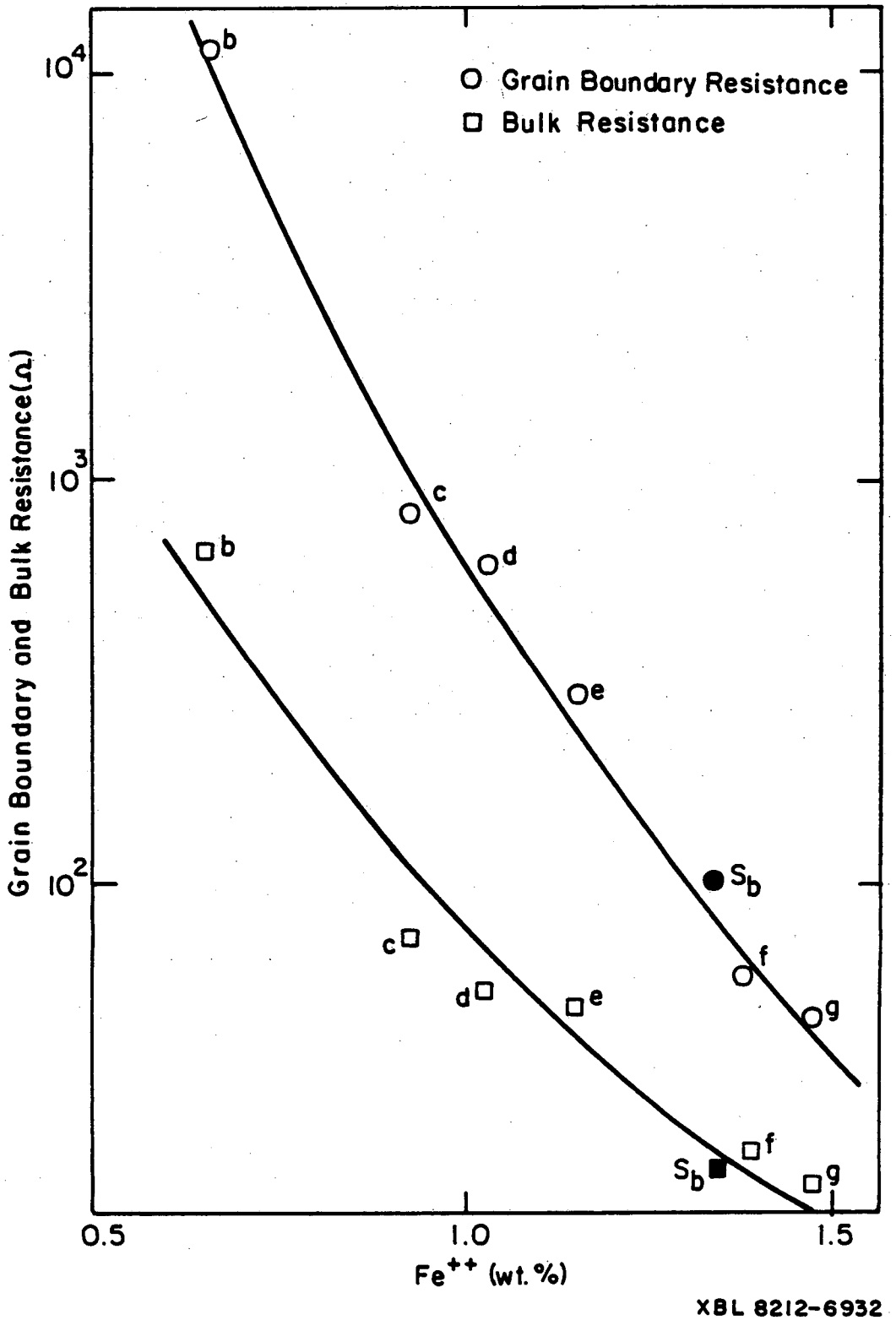
Grain Boundary Resistance
Bulk Resistance
Grain Boundary and Bulk Resistance(Ω)
10^4
10^3
10^2
b
c
d
e
S_b
f
g
0.5
1.0
1.5
Fe^{++} (wt.%)
XBL 8212-6932

Fig.IV.4

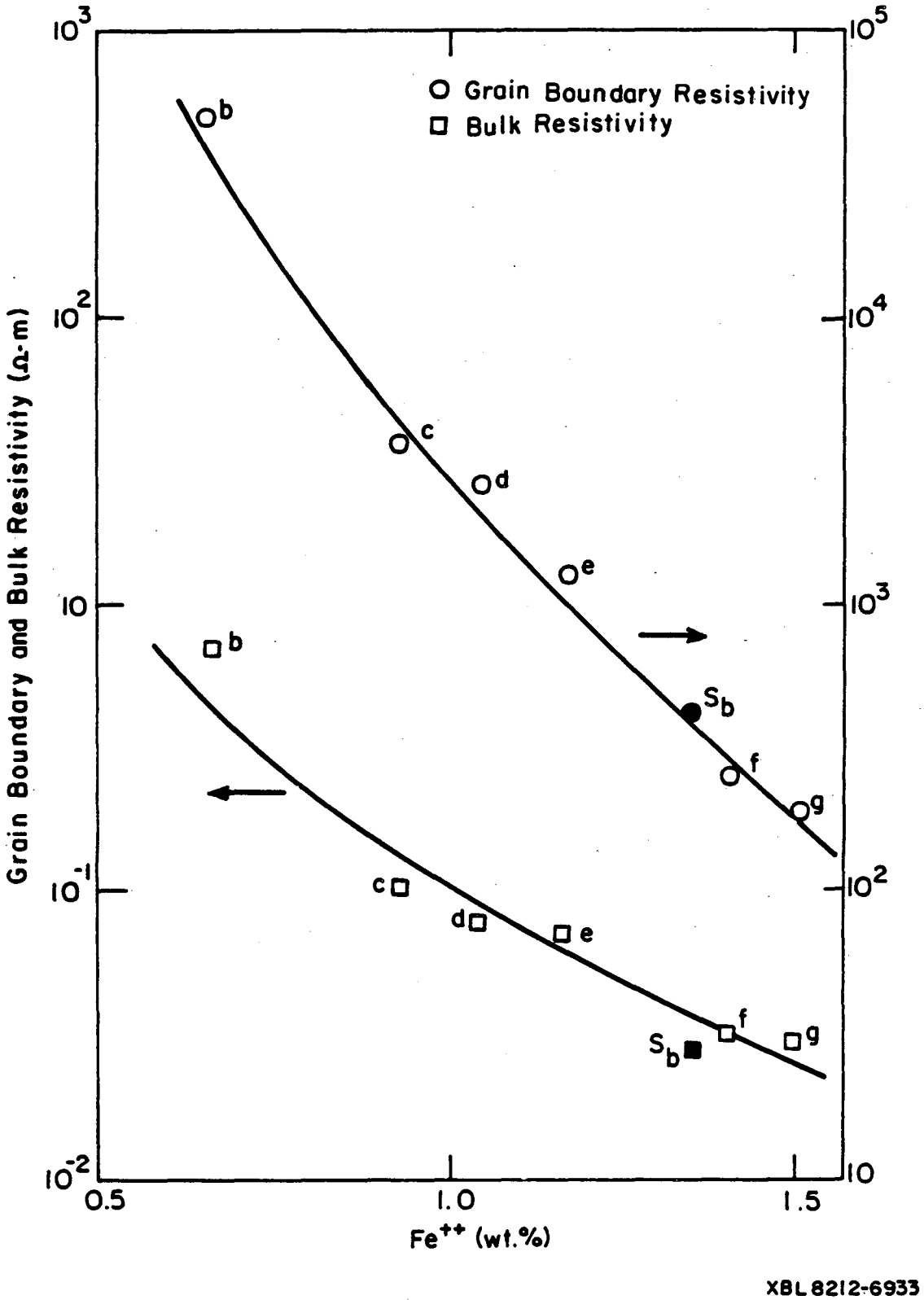
Grain Boundary Resistivity
Bulk Resistivity
Grain Boundary and Bulk Resistivity (Ω·m)
Fe++ (wt.%)
10^3
10^2
10
10^-1
10^-2
10^5
10^4
10^3
10^2
10
0.5
1.0
1.5
b
c
d
e
f
g
Sb
XBL 8212-6933

Fig.IV.5

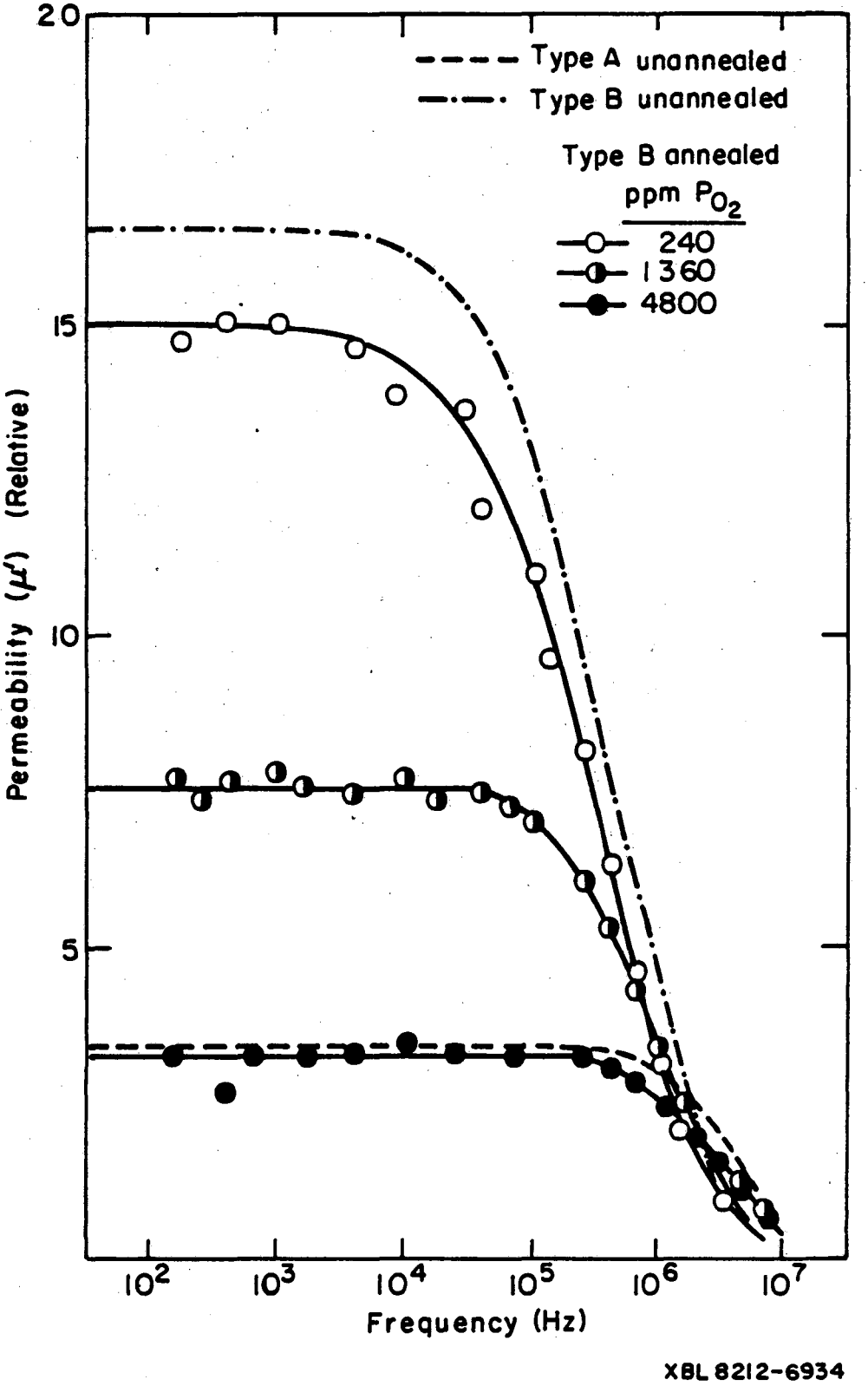
20
15
10
5
Permeability (μ') (Relative)
Type A unannealed
Type B unannealed
Type B annealed
ppm P_{O_2}
240
1360
4800
10^2
10^3
10^4
10^5
10^6
10^7
Frequency (Hz)
XBL 8212-6934

Fig.IV.6a

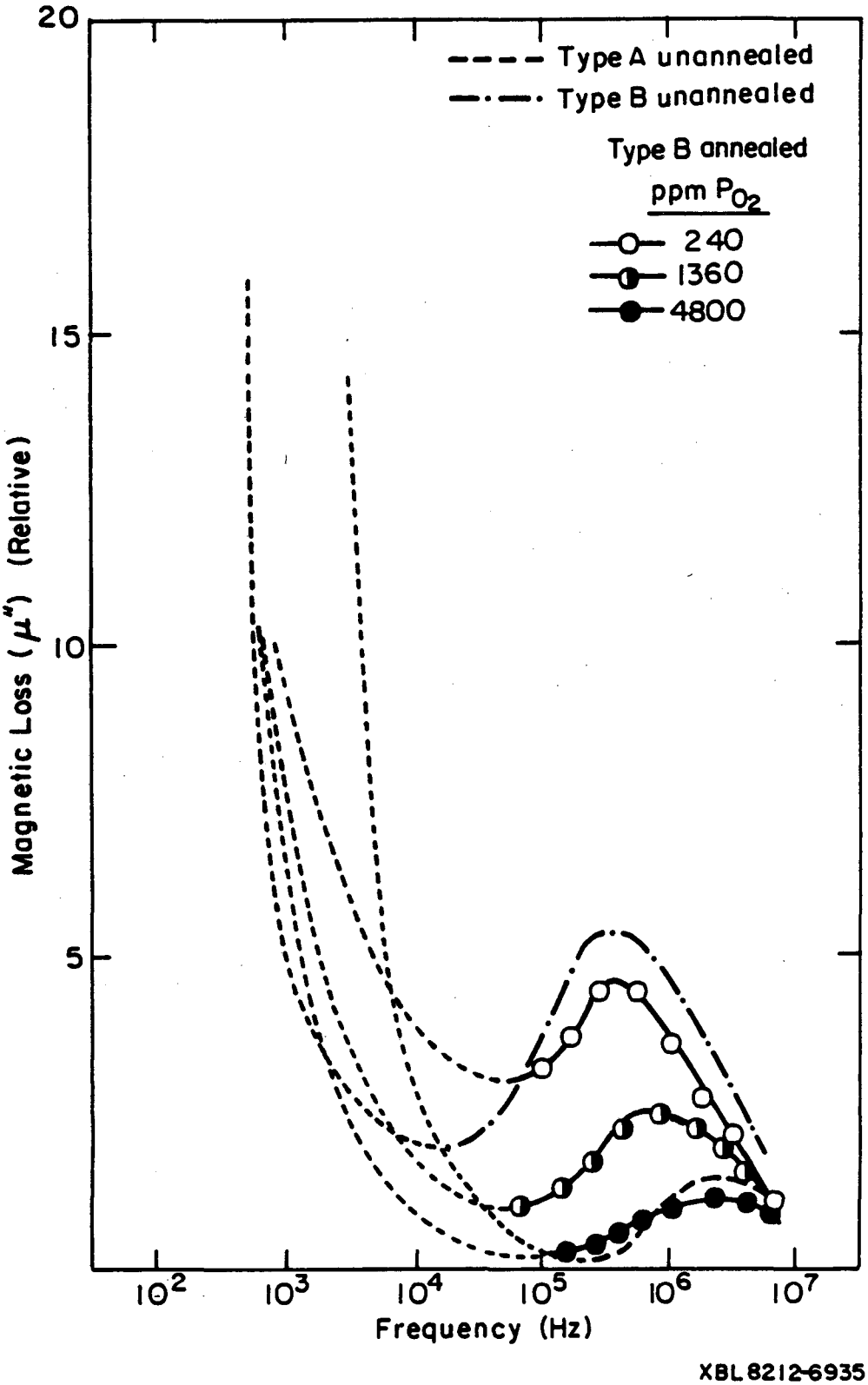
Type A unannealed
Type B unannealed
Type B annealed
ppm P_{O_2}
240
1360
4800
Magnetic Loss (μ") (Relative)
Frequency (Hz)
20
15
10
5
10^2
10^3
10^4
10^5
10^6
10^7
XBL8212-6935

Fig.IV.6b

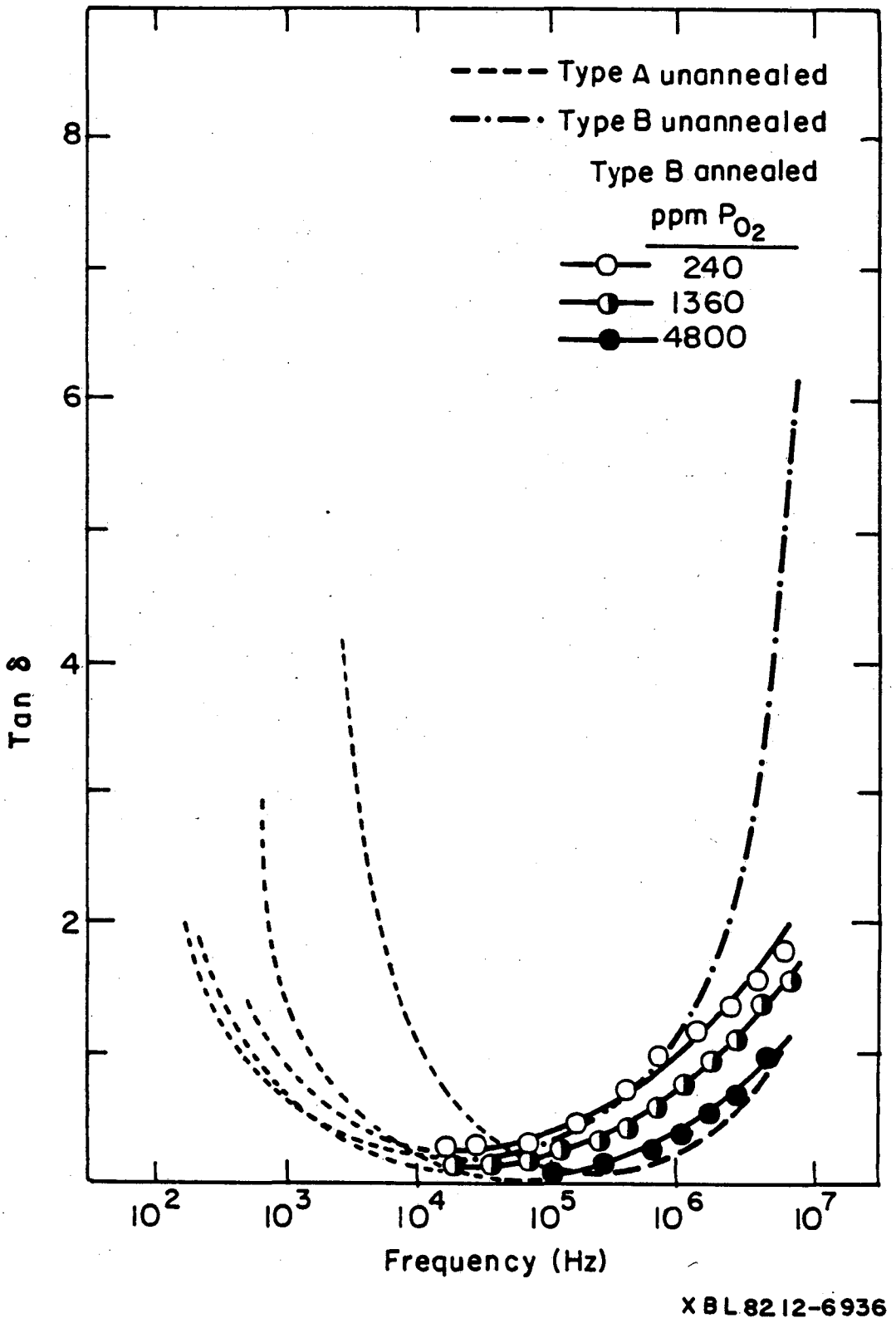
Type A unannealed
Type B unannealed
Type B annealed
ppm P_{O_2}
240
1360
4800
Tan δ
8
6
4
2
10^2
10^3
10^4
10^5
10^6
10^7
Frequency (Hz)
XBL8212-6936

Fig.IV.6c

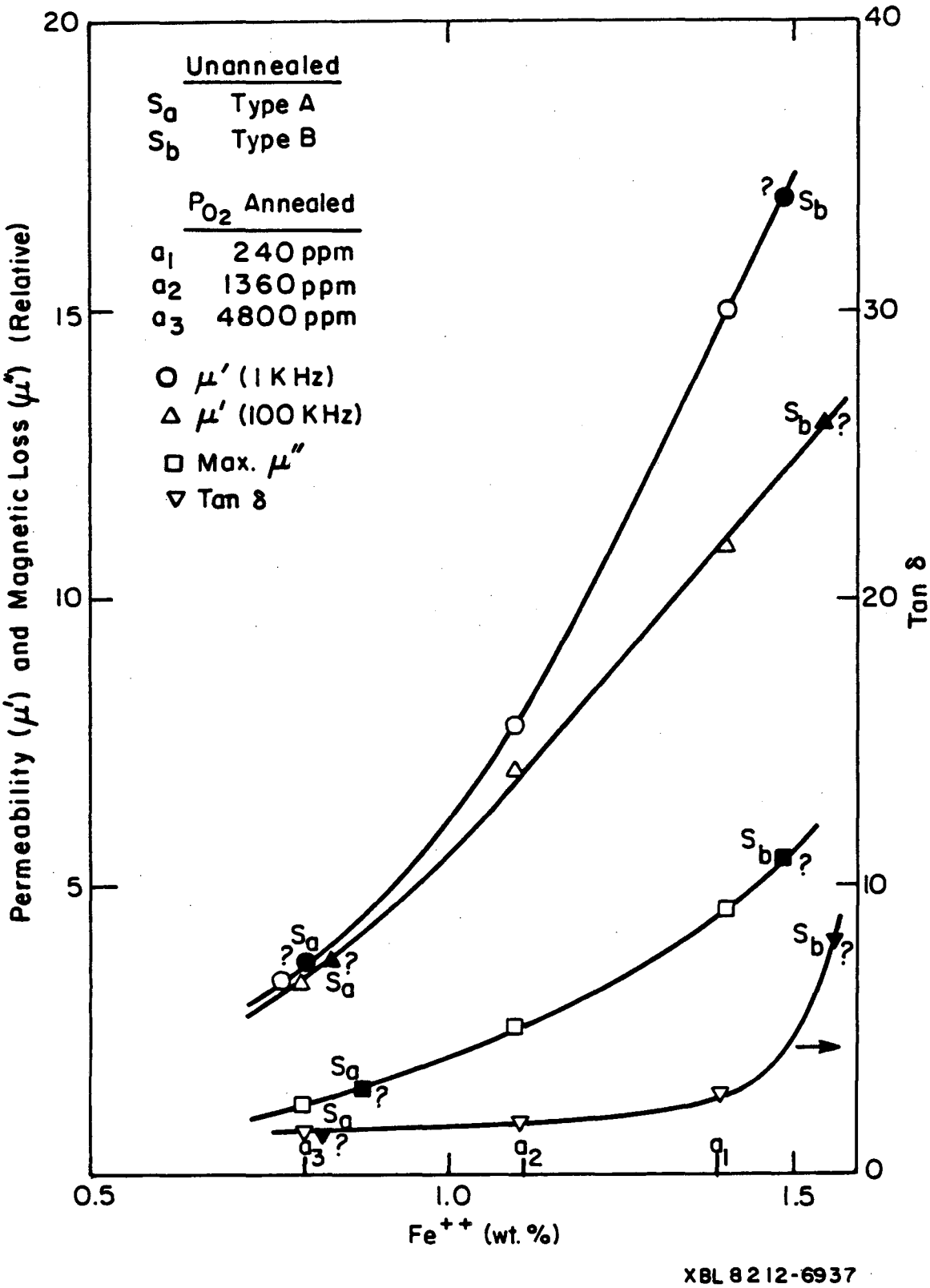
Unannealed
S_a Type A
S_b Type B
P_{O_2} Annealed
a_1 240 ppm
a_2 1360 ppm
a_3 4800 ppm
O μ' (1 KHz)
Δ μ' (100 KHz)
□ Max. μ''
▽ Tan δ
Permeability (μ') and Magnetic Loss (μ'') (Relative)
Tan δ
Fe^{++} (wt. %)
20
15
10
5
40
30
20
10
0
0.5
1.0
1.5
a_1
a_2
a_3
S_a
S_b
?
XBL 8212-6937

Fig.IV.7

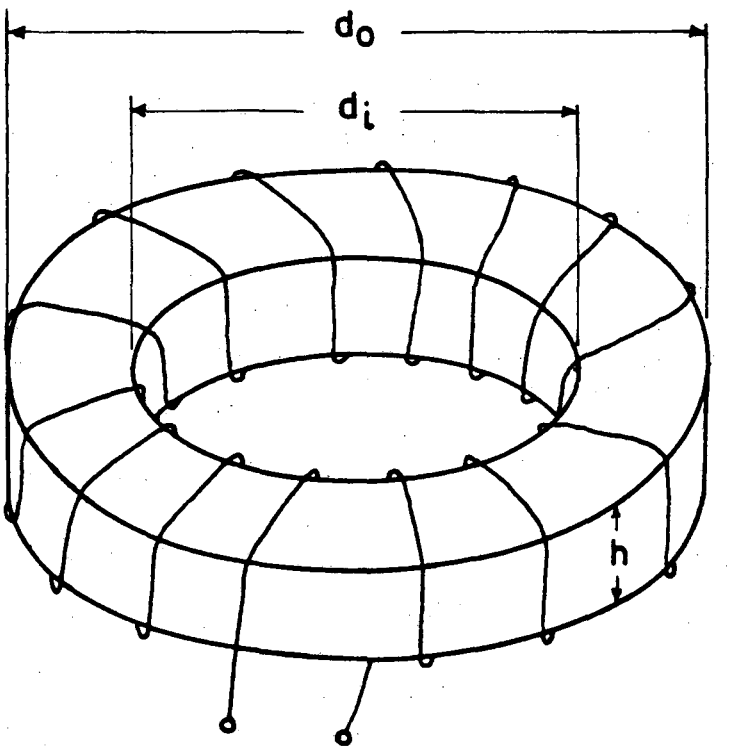

$$L_o = 0.2972\, N^2\, h \log \frac{d_o}{d_i} \quad \text{(micro-henrys)}$$

N = no. of turns of the coil

h = thickness of the toroid

d_o = outside diameter of the toroid

d_i = inside diameteter of the toroid

XBL 8211-6835

Fig.A.1

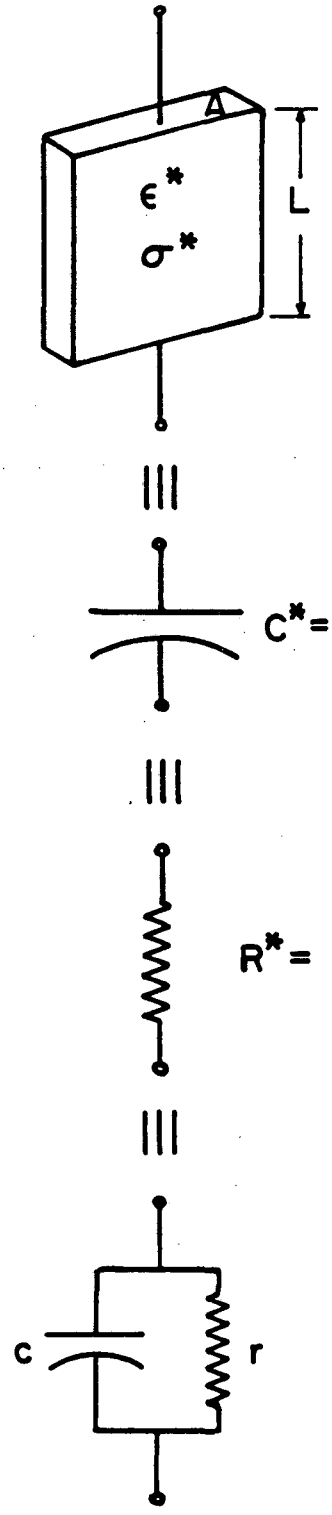

$\epsilon^* = \epsilon' - j\epsilon''$

$\sigma^* = \omega\epsilon''$

$\frac{1}{Z} = j\omega C^* = j\omega\epsilon^* \frac{A}{L}$

$\sigma^* = \sigma' + j\sigma''$

$\epsilon' = \frac{\sigma''}{\omega}$

$\frac{1}{Z} = \frac{1}{R^*} = \sigma^* \frac{A}{L}$

$r = \frac{1}{\sigma} \frac{L}{A}$

$c = \epsilon' \frac{A}{L}$

$\frac{1}{Z} = \frac{1}{r} + j\omega c$

XBL 8211-6836

Fig.A.2

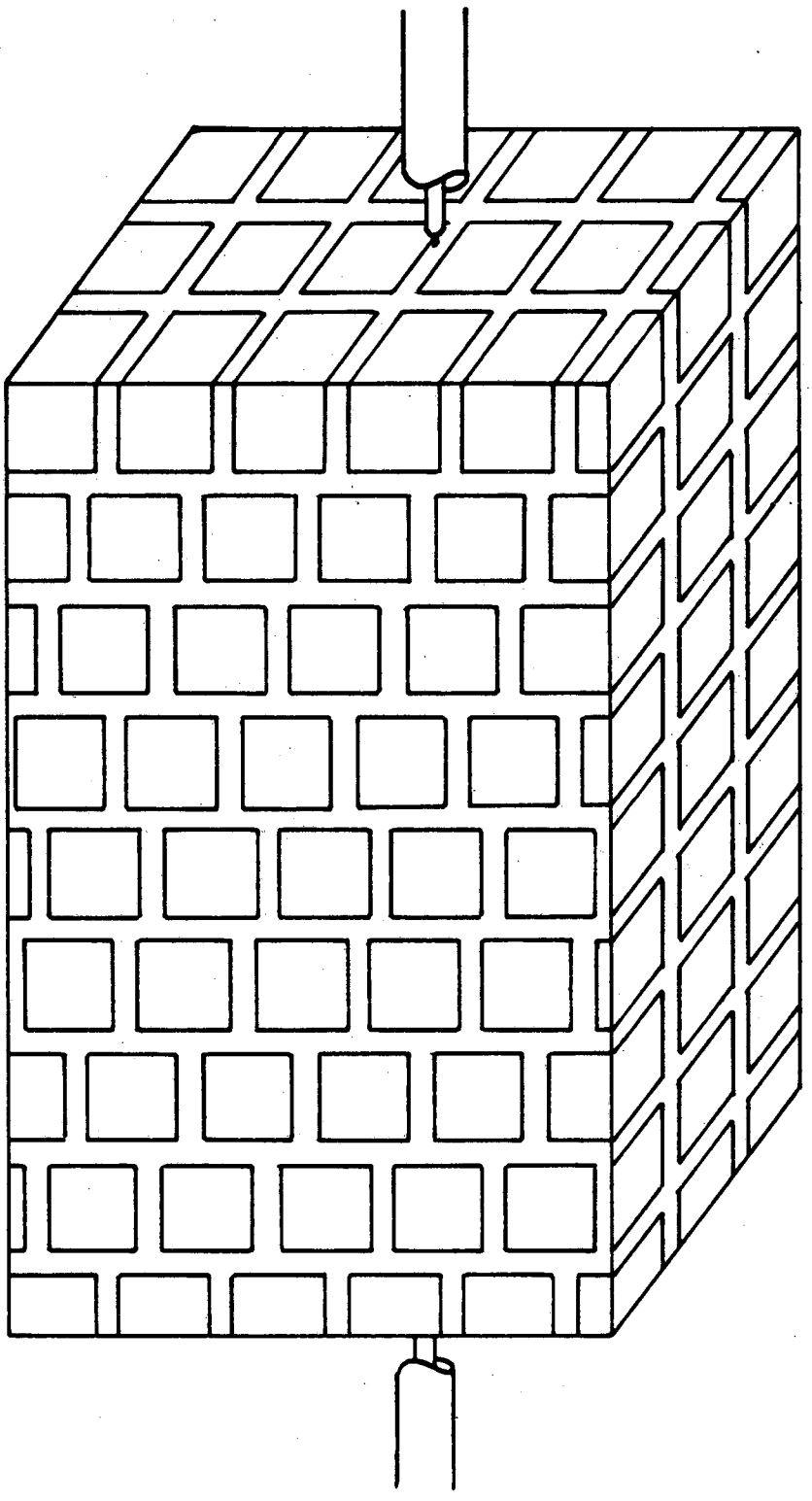

XBL8211-6837

Fig.A.3a

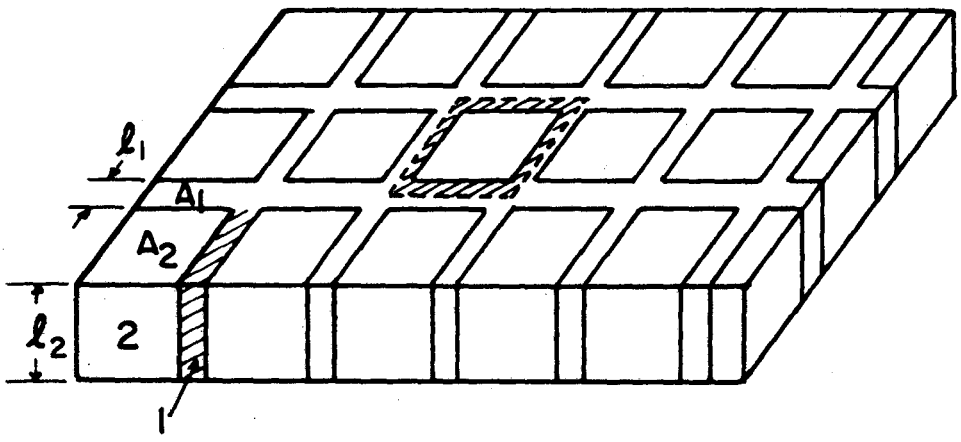

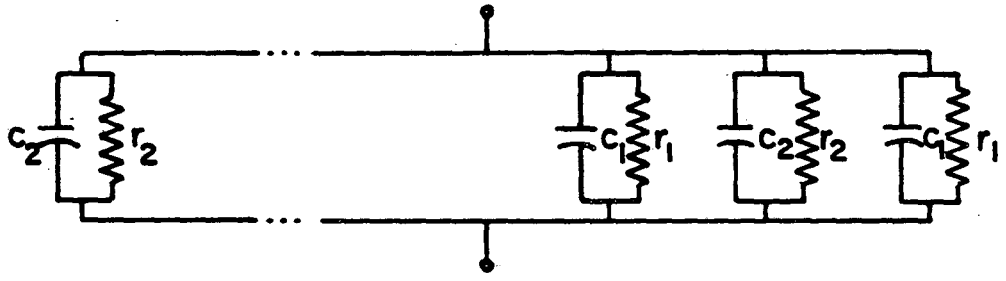

$$\begin{cases} r_i = \rho_i \dfrac{d_i}{A_i} \\ c_i = \epsilon_i \dfrac{A_i}{d_i} \end{cases}$$

$i = 1$ for grain boundary
$i = 2$ for grain
A_i = cross-sectional area
d_i = length of conducting path

XBL 8211-6838

Fig.A.3b

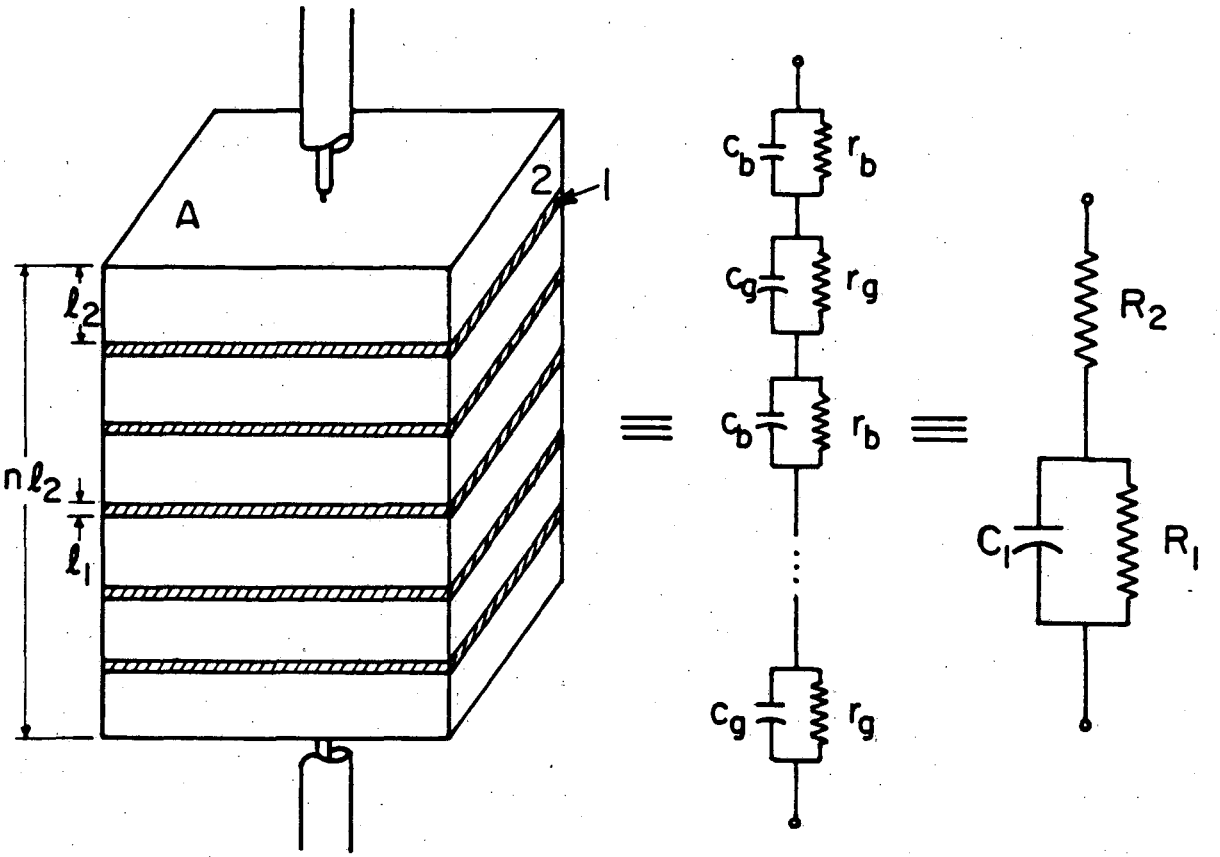

$$\begin{cases} r_b = \rho_2 \dfrac{\ell_2}{A} \\ c_b = \epsilon_2 \dfrac{A}{\ell_2} \end{cases}$$

$$\begin{cases} r_g = \rho_1 \dfrac{\ell_1}{A} \\ c_g = \epsilon_1 \dfrac{A}{\ell_1} \end{cases}$$

$$R_2 = n\, r_b$$

$$\begin{cases} R_1 = n\, r_g \\ C_1 = \dfrac{1}{n}\, c_g \end{cases}$$

n: no. of grains

XBL 8211-6839

Fig.A.3c

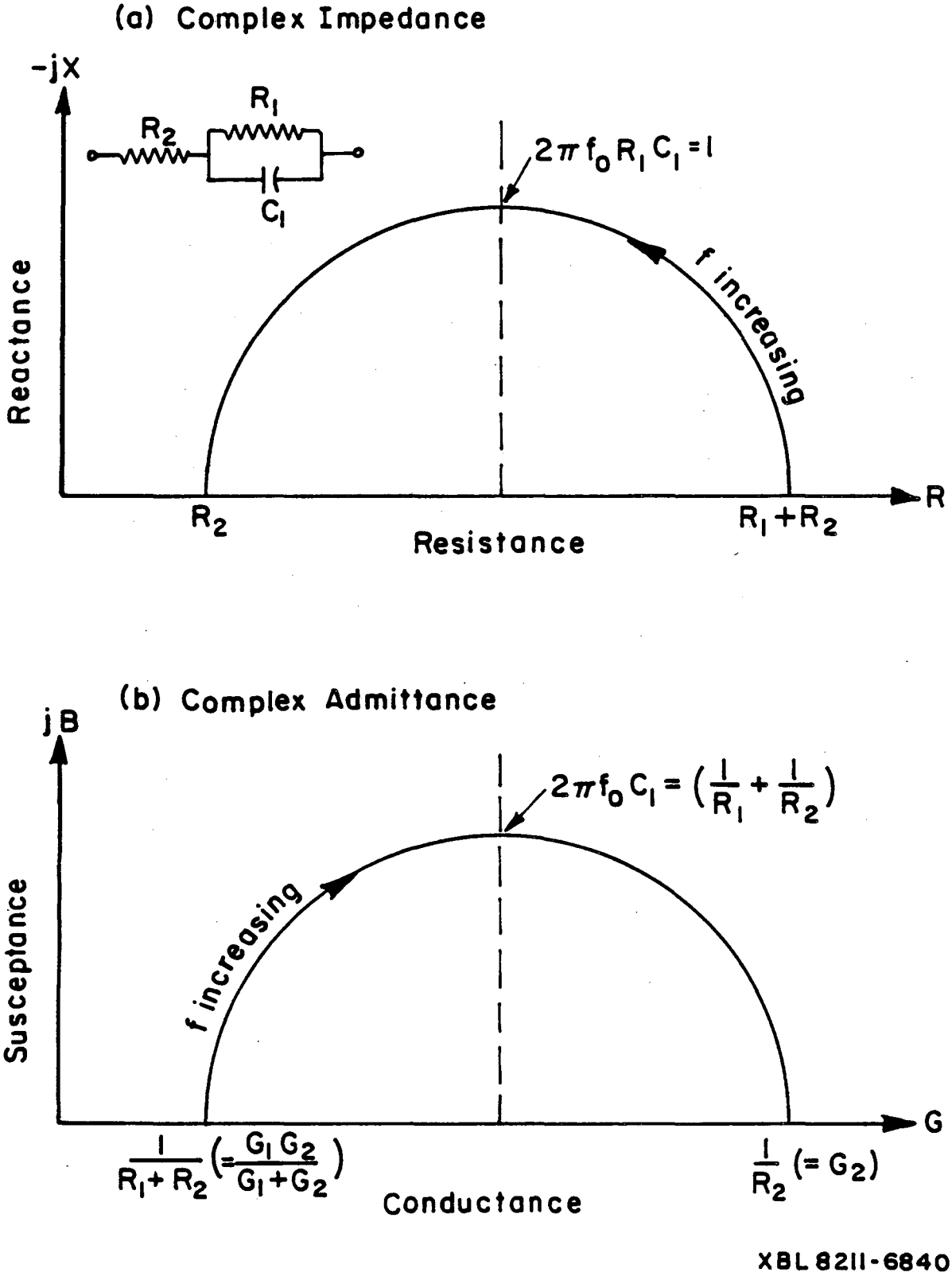
(a) Complex Impedance
-jX
R1
R2
C1
2πf0R1C1=1
f increasing
Reactance
R
R2
R1+R2
Resistance
(b) Complex Admittance
jB
2πf0C1 = (1/R1 + 1/R2)
f increasing
Susceptance
G
1/(R1+R2) (=G1G2/(G1+G2))
1/R2 (=G2)
Conductance
XBL 8211-6840

Fig.A.4

(a) Block Diagram

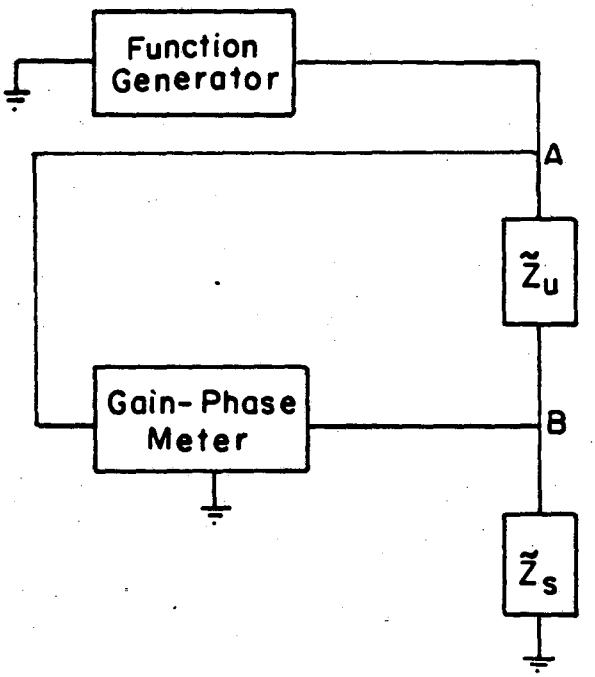

$$\tilde{Z}_u = R_x + jX_x;\ \tilde{Z}_s = R_s + jX_s$$

$$R_x = R_s(\alpha\cos\theta - 1) + X_s\alpha\sin\theta$$

$$X_x = X_s(\alpha\cos\theta - 1) - R_s\alpha\sin\theta$$

$$G_x = \frac{R_x}{R_x^2 + X_x^2}$$

$$-H_x = \frac{X_x}{R_x^2 + X_x^2}$$

$$\frac{\tilde{V}_A}{\tilde{V}_B} = \alpha e^{-j\theta}$$

(b) Specimen Jig

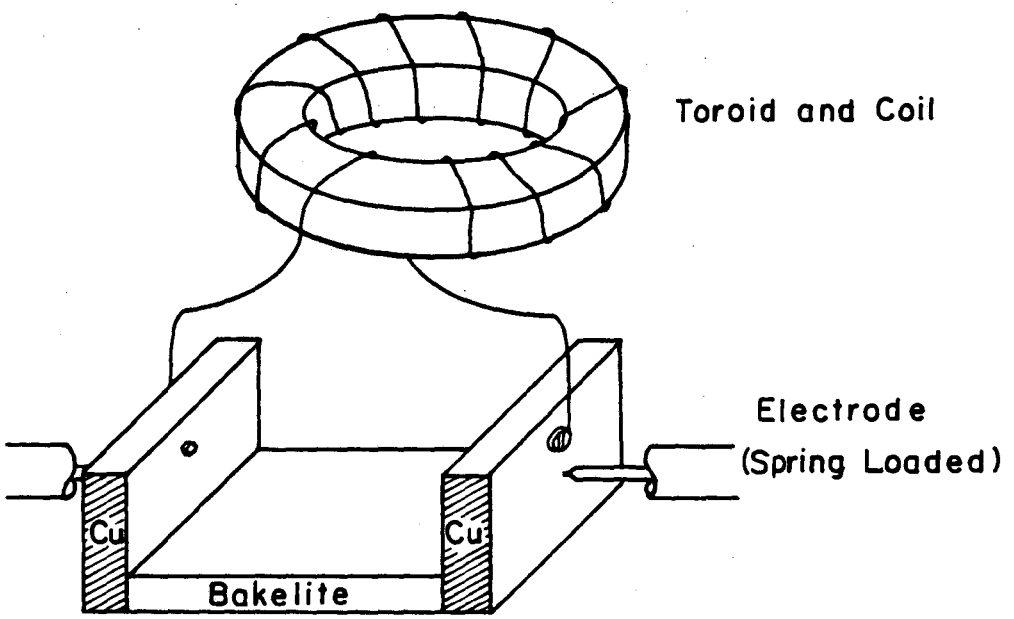

XBL821I-6841

Fig.A.5

(a) Standard Impedance

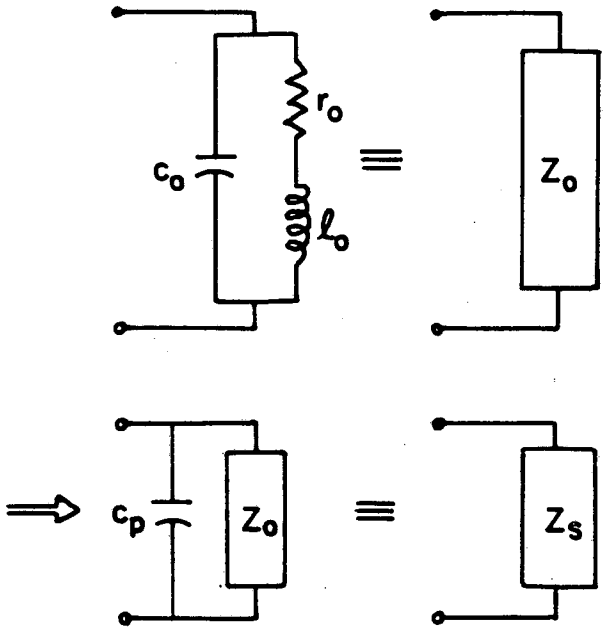

$$r_s = \frac{r_o}{(1-\omega^2 l_o c_o)^2 + \omega^2 c_o^2 r_o^2} \quad ;$$

$$x_s = \frac{\omega l_o (1-\omega^2 l_o c_o) - \omega c_o r_o^2}{(1-\omega^2 l_o c_o)^2 + \omega^2 c_o^2 r_o^2}$$

$$R_s = \frac{r_s (1-\omega c_p x_s) + \omega c_p r_s x_s}{(1-\omega c_p x_s)^2 + \omega^2 c_p^2 r_s^2} \quad ;$$

$$X_s = \frac{x_s (1-\omega c_p x_s) - \omega c_p r_s^2}{(1-\omega c_p x_s)^2 + \omega^2 c_p^2 r_s^2}$$

(b) Apparent Resistivity and Dielectric Constant

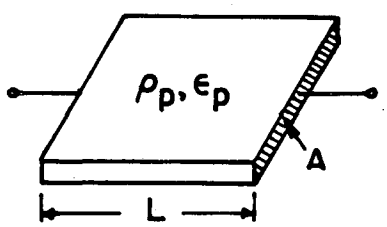

$$\begin{cases} r_p = \rho_p \frac{L}{A} \\ c_p = \epsilon_p \frac{A}{L} \end{cases}$$

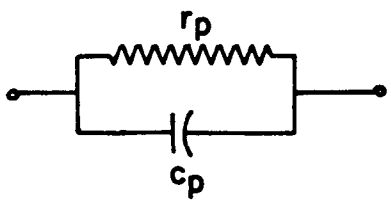

$$\begin{cases} \rho_p = \frac{A}{L} \frac{1}{G_x} \\ \epsilon_p = \frac{L}{A} \frac{B_x}{\omega} \end{cases}$$

$$Y = G_x + j B_x = \frac{1}{r_p} + j\omega c_p$$

XBL8211-6842

Fig.A.6

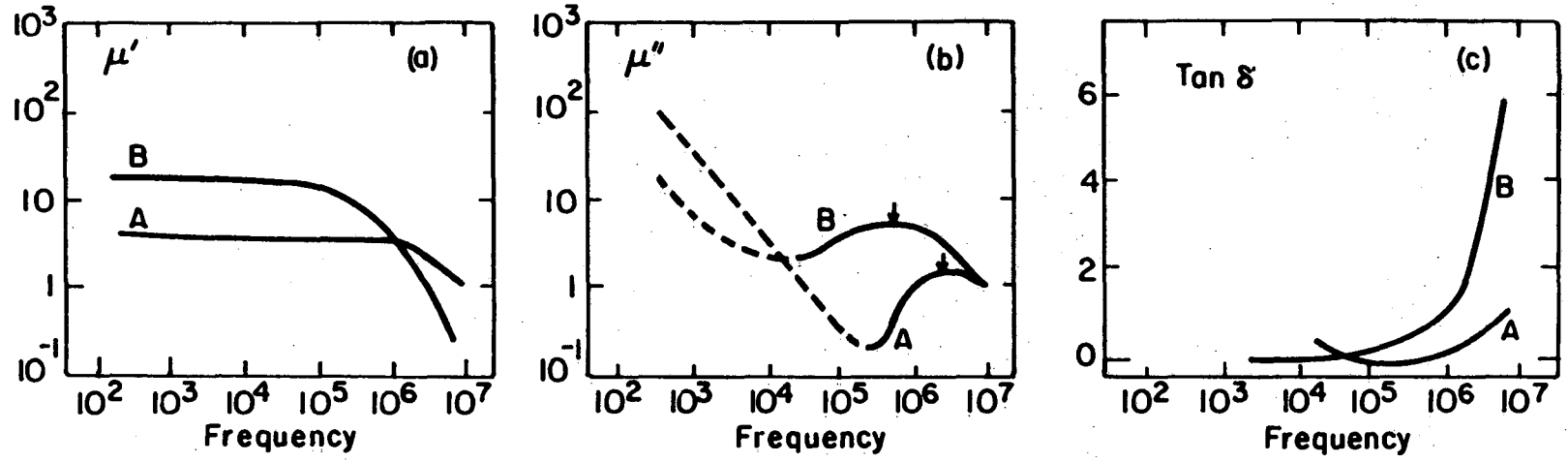

A: Low Loss MnZn-Ferrite
B: High μ_i MnZn-Ferrite

XBL8211-6843

Fig.A.7

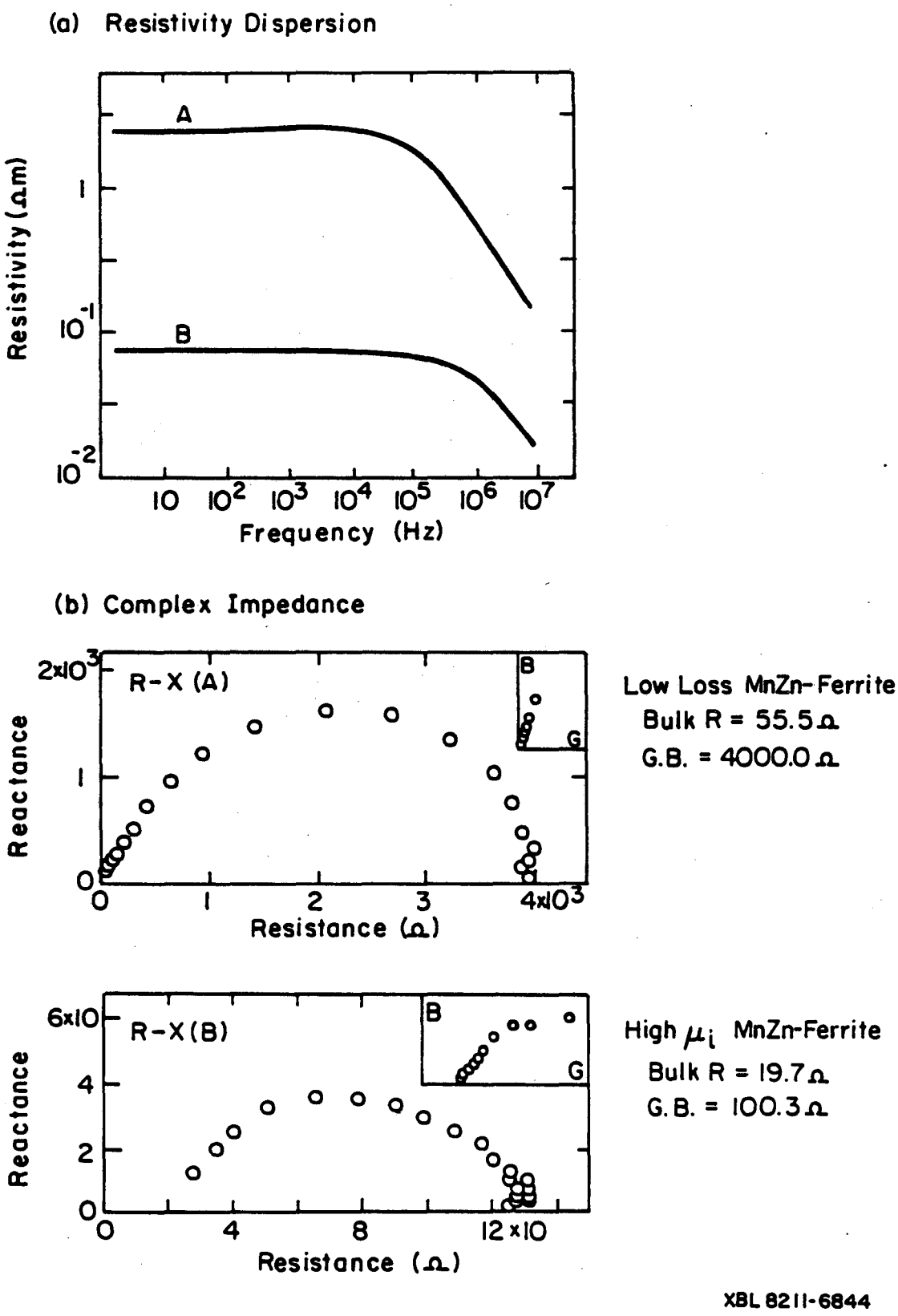
(a) Resistivity Dispersion
A
B
Resistivity (Ωm)
1
10⁻¹
10⁻²
10
10²
10³
10⁴
10⁵
10⁶
10⁷
Frequency (Hz)
(b) Complex Impedance
R-X (A)
2x10³
Reactance
0
1
2
3
4x10³
Resistance (Ω)
B
G
Low Loss MnZn-Ferrite
Bulk R = 55.5 Ω
G.B. = 4000.0 Ω
R-X (B)
6x10
4
2
0
4
8
12x10
Resistance (Ω)
High μi MnZn-Ferrite
Bulk R = 19.7 Ω
G.B. = 100.3 Ω
XBL 8211-6844

Fig.A.8

TECHNICAL INFORMATION DEPARTMENT
LAWRENCE BERKELEY LABORATORY
UNIVERSITY OF CALIFORNIA
BERKELEY, CALIFORNIA 94720